Western Graduate&PostdoctoralStudies

Western University
Scholarship@Western

Electronic Thesis and Dissertation Repository

6-18-2020 10:00 AM

Internal Pressure Modelling for Low-Rise Buildings in Tornadic Winds

Aaron L. Jaffe, *The University of Western Ontario*

Supervisor: Kopp, Gregory A., *The University of Western Ontario*

A thesis submitted in partial fulfillment of the requirements for the Master of Engineering Science degree in Civil and Environmental Engineering

© Aaron L. Jaffe 2020

Follow this and additional works at: https://ir.lib.uwo.ca/etd

Part of the Civil Engineering Commons

Recommended Citation

Jaffe, Aaron L., "Internal Pressure Modelling for Low-Rise Buildings in Tornadic Winds" (2020). *Electronic Thesis and Dissertation Repository*. 7063.
https://ir.lib.uwo.ca/etd/7063

This Dissertation/Thesis is brought to you for free and open access by Scholarship@Western. It has been accepted for inclusion in Electronic Thesis and Dissertation Repository by an authorized administrator of Scholarship@Western. For more information, please contact wlswadmin@uwo.ca.

Abstract

Internal pressures play a large role in the failure of wood-frame houses as the loss of the entire roof section becomes much more likely once the envelope of the building has been breached. Many studies have used internal pressure modelling to simulate internal pressures in structures from atmospheric boundary layer (ABL) winds, however, relatively little work has been done on this subject using tornadic winds. The objective of this study is to explore internal pressure modelling issues for tornadoes. The first part of the study uses a computational internal pressure model to simulate tornadic internal pressures of a low-rise structure; the second part uses the same model to estimate failure wind speeds of a flexible garage door, one of the critical failure modes of these structures.

The internal pressure model is able to reasonably simulate measured internal pressures in tornadic winds, although not quite as well as in ABL winds. The modelled internal pressure coefficients are mostly within 0.1 of measured internal pressure coefficients, which is similar to uncertainty bounds. When comparing ABL and tornadic building pressures, some differences are found in the mean pressures at oblique directions and the pressure distributions for normal wind directions. An analysis of the spectra of the theoretical model equation terms reveals that a lack of internal volume scaling in the tornadic tests also contributes to the differences from ABL tests.

The same theoretical model also shows that net loads on garage doors are typically reduced to 34-46% of the external pressure applied from the wind due to the internal pressure developed in the garage from the fluctuating opening size during loading. When these results are combined with experimental net pressures of garage door failures, the resulting range of expected failure wind speeds are 130-265 km/h.

Keywords: Internal Pressures, Internal Pressure Modelling, Tornadoes, Garage Doors, Low-Rise Structures

Summary for Lay Audience

Tornadoes and other severe wind events pose a significant threat to residential structures across the globe, and are a prominent issue in Canada and the United States. Although the majority of the costs of damages from these events are to houses, they are not designed for them. When it comes to severe wind, the most crucial part of a residential building in terms of structural and economic integrity is its roof. The loss of a house's roof exposes the interior to wind and rain, resulting in the destruction of contents, unsalvageable damage to the structure, and a significant threat to human life.

Wind causes pressures that push and pull on various elements of a structure. When the structure is breached by severe winds, often due to debris damage to doors and windows, or the inward collapse of a garage door, these pressures enter the building and become internal pressures that push up on the roof and out on the walls. Therefore, these openings greatly increase the chance of the loss of a house's roof in these events. The goal of this thesis is to understand these internal pressure, and how they differ in tornadoes versus "straight-line" wind.

This thesis contains two parts. The first part examines and simulates the internal pressures in a residential structure model from a tornadic wind-tunnel test. A comparison is then made between results from tornadic and straight-line wind tunnel tests. The second part of the thesis examines the failure wind speeds of garage doors in severe wind events. This is done by combining past experimental testing of the wind-resistance of garage doors, with the theoretical model that was used to simulate internal pressures in the first part of the thesis.

This study concludes that internal pressures can be simulated in tornadic winds, despite the differences from straight-line winds. The study also gives failure wind speeds of several garage door models, which mostly align with the Enhanced Fujita Scale, the primary way of assessing damaging winds in North America. The conclusions from both parts of this thesis lead to a better understanding of the behaviour of internal pressures in tornadoes and other severe wind events. Research such as this will aid in designing more wind resilient structures for the future.

Co-Authorship Statement

Chapter 2 and Chapter 4 from this thesis share text and figures from a journal paper that was co-authored by my supervisor, Dr. Gregory Kopp, former research student Alexander Riveros, and myself. The reference for this journal article, which was published by Frontiers in Built Environment, is shown below.

Jaffe, A. L., Riveros, G. A., & Kopp, G. A. (2019). Wind Speed Estimates for Garage Door Failures in Tornadoes. *Frontiers in Built Environment*, *5*, 14.

In this article, I was responsible for approximately 60% of the work, Alexander Riveros was responsible for 40% of the work and Dr. Gregory Kopp was responsible for overseeing the work. Alexander Riveros lead the experimental testing of the garage doors and the analysis of those results. I was responsible for development the internal pressure model, using this model to explore wind effects on flexible openings, and combining the model with the experimental data to determine failure wind speeds for the garage doors.

Additionally, the WindEEE Dome wind tunnel experiments described in Chapter 2 and analyzed in Chapter 3 were conducted by Dr. Chieh-Hsun Wu (then PhD student). His work is referenced throughout those sections and all analysis and modelling discussed in this thesis from those experiments were conducted myself.

Acknowledgements

This project would not have been possible without the contributions of many important individuals. Firstly, I would like to acknowledge Dr. Gregory Kopp, my supervisor, for all his gracious support and guidance these past few years. Without Dr. Kopp, I never would have gone into wind engineering here at Western, let alone written this thesis.

I would also like to acknowledge several former and current researchers whose contributions were crucial to this thesis. Dr. Chieh-Hsun Wu provided invaluable data from his WindEEE experiments, and met with me, sometimes weekly, to aid in the data gathering and analysis. Alexander Riveros performed the garage door failure experiments, and was a co-author of crucial research to the second half of this study. Dr. Jeong Hee Oh paved the way for this work with his research on the Helmholtz resonator model, which was an integral part of this thesis.

Finally, I would like to thank my family, friends, and co-workers for their continued support during this process and in the years to come.

Table of Contents

Abstract ii

Summary for Lay Audience iii

Co-Authorship Statement iv

Acknowledgements v

List of Tables ix

List of Figures x

Nomenclature xiv

1. Introduction 1

1.1 Background 1

1.2 Literature Review 3

1.2.1 Theoretical Model for Internal Pressures 3

1.2.2 Internal Pressures in Tornadoes 6

1.2.3 Internal Pressures with Variable Openings 9

1.3 Objectives 10

2. Methodology and Data 13

2.1 Wind Tunnel Testing 13

2.2 Full-Scale Garage Door Testing 17

2.2.1 Experimental Setup 17

2.2.2 Experimental Results 19

2.3 Internal Pressure Modelling 22

2.3.1 Modelling for Tornadic Experiments 22

2.3.2 Modelling for Garage Door Experiments 25

2.3.3 Comparisons to Oh et al. (2007) and Oh (2004) 27

3. Internal Pressures for a Building in a Tornado 31

3.1 Experimental and Model Results 31

3.1.1 Wind Flow Field 31

3.1.2 Ensemble Pressure Results 35

3.2 Comparison to Internal Pressures in ABL Winds 43

3.2.1 Pressure Results by Wind Direction 43

3.2.2 Distributions and Fits of Pressures 51

3.2.3 Analysis of SDE Terms and Spectra 53

3.3 Summary 65

4. Internal Pressures in Residential Garages 67

4.1 Internal Pressure Model Results 67

4.1.1 Fixed and Flexible Opening Cases 67

4.1.2 Other Flexible Opening Cases 73

4.1.3 Other Wind Directions 75

4.2 Failure Wind Speeds 78

4.2.1 Method 78

4.2.2 Results 79

4.3 Summary 82

5. Conclusions and Recommendations 83

5.1 Conclusions 83

5.2 Recommendations 84

6. References 86

Appendices 92

Appendix A – Comparison of External Pressure Taps Surrounding Opening 92

Curriculum Vitae 96

List of Tables

Table 1-1: EF-Scale DOD descriptions and wind speeds for FR12 (Environment Canada, 2014).2

Table 1-2: Summary of previous research on tornado-induced internal pressures. 7

Table 2-1: Parameters of the experimental setup in the WindEEE Dome tests (after Kopp and Wu, 2020). 16

Table 2-2: Comparison of test results for garage door experiments. 20

Table 2-3: List of variables in the SDE equation for WindEEE and garage door experiments. .. 23

Table 2-4: Comparison of pressure coefficients in Oh (2004) to the current model. 29

Table 3-1: Mean and rms internal and external pressure coefficients at various wind directions for the current study and the ABL experiments. 47

Table 3-2: Mean of the absolute values and rms of the driving, inertial, and frictional terms for internal pressure coefficients of the tornadic and ABL configurations. 57

Table 4-1: Open area and pressure means and maxima of fixed and flexible opening cases. 73

Table 4-2: Expected, lower-bound, and upper-bound failure wind speeds of garage doors. 80

List of Figures

Figure 1-1: A representation of the Bernoulli equation showing velocity, pressure, and relative height at two locations along fluid flow streamlines. 4

Figure 1-2: The Helmholtz resonator model for a building with a single dominant opening (after Holmes, 2015). 5

Figure 2-1: (a) Photo of the building model in the wind tunnel and (b) exploded view of the building showing the dimensions of the structure and its opening in centimetres along with wind directions (after Kopp and Wu, 2020). 14

Figure 2-2: Diagram showing the location of the building, the location and orientation of the Cobra probes, and the direction of vortex translation and rotation (after Kopp and Wu, 2020). . 15

Figure 2-3: (a) A conceptual image of the pressure chamber setup, and photographs of (b) its backside with (c) detailed connections to PLAs and (d) the displacement transducer support frame. 18

Figure 2-4: Conceptual image of a garage door deflection curve at its top edge. The opening area is equivalent to area under the curve..... 20

Figure 2-5: Total open area as a function of applied net pressure for (a) all three Product 2 doors tested, (b) Product 3, and (c) all samples for which displacement data were obtained. 21

Figure 2-6: Sample time history showing the external pressure at the opening, the simulated internal pressure from the SDE, and the measured internal pressure inside the building for (a) a full trial duration and (b) a section of the trial. 24

Figure 2-7: A section of sample simulated internal pressure time history from Oh et al. (2007) compared to the current model. 30

Figure 3-1: Ensemble-averaged wind direction at the opening (θo) across all trials vs. normalized vortex location (yr)..... 32

Figure 3-2: Total horizontal wind direction (V) broken down into tangential ($V\theta$), radial (Vr), and translational (Vt) vector components at various building locations relative to the translating vortex. 33

Figure 3-3: A sketch of the wind streamlines from the main vortex (thick red line) and sub-vortices (blue lines) in the WindEEE experiment showing high and low turbulence regions and two building locations relative to the location of the main vortex. 35

Figure 3-4: Ensemble-averaged wind velocity magnitude at each Cobra probe and a moving average of the results vs. normalized vortex location (after Kopp and Wu, 2020). 36

Figure 3-5: Ensemble-averaged mean, maximum, and minimum of external and internal aerodynamic pressure coefficients from all configurations. External pressure at the opening, simulated internal pressure from the SDE, and measured internal pressure inside the building plotted vs. (a) normalized vortex location (yr) and (b) wind direction at the opening (θo). 39

Figure 3-6: Ensemble-averaged mean ± rms external and internal dynamic pressure coefficients over five degree increments of wind direction for (a) the current study, (b) the ABL-Short case with building dimensions of 38.1 x 24.4, a height of 4.9 cm, and an open ratio of 3.3% with background leakage, and (c) the ABL-Tall case with the same details as ABL-Short except for an increased height of 12.2 cm. 46

Figure 3-7: Combined graph of ensemble-averaged mean and rms simulated and measured internal pressure coefficients vs. wind direction in five degree increments for the current tornadic study and for the ABL-Short and ABL-Tall cases..... 49

Figure 3-8: Probability density histograms for the measured internal pressure coefficients of the (a) 90° and (b) 135° wind direction from the current study, (c) 90° and (d) 135° wind direction from the ABL-Short case, and (e) 90° and (f) 135° wind direction from the ABL-Tall case. 52

Figure 3-9: Full time-histories of the driving, inertial and frictional terms for the (a) measured and (b) simulated internal pressures of the regular tornadic case, (c) measured and (d) simulated internal pressures of the scaled tornadic case, (e) measured and (f) simulated internal pressures of

the ABL-Short case, and (g) measured and (h) simulated internal pressures of the ABL-Tall case. 54

Figure 3-10: Time-history segments of the driving, inertial and frictional terms for the (a) measured and (b) simulated internal pressures of the regular tornadic case, (c) measured and (d) simulated internal pressures of the scaled tornadic case, (e) measured and (f) simulated internal pressures of the ABL-Short case, and (g) measured and (h) simulated internal pressures of the ABL-Tall case. 55

Figure 3-11: Spectra of the driving, inertial and frictional terms for the (a) measured and (b) simulated internal pressures of the regular tornadic case, (c) measured and (d) simulated internal pressures of the scaled tornadic case, (e) measured and (f) simulated internal pressures of the ABL-Short case, and (g) measured and (h) simulated internal pressures of the ABL-Tall case.. 60

Figure 3-12: Spectra of the external, simulated internal, and measured internal pressure coefficients of the stitched-together tornadic cases at 90° with (a) regular internal volume and (b) scaled internal volume. 63

Figure 3-13: Spectra of the external, simulated internal, and measured internal pressure coefficients at a wind direction of 90° for the (a) ABL-Short case and (b) ABL-Tall case. 64

Figure 4-1: Time-history of external, simulated internal, and net pressure over a small section of the time series of a garage door sample with a fixed opening area of (a) 0.1% and (b) 1.0%. 68

Figure 4-2: Time-histories of (a) external, simulated internal, and net pressure for the SDE using a flexible garage door, and the net pressure for the MDE for a fixed garage door opening of 1% of door area, and (b) the open area as a function of time for the flexible garage door. 71

Figure 4-3: Simplified version of total opening area as a function of applied net pressure for the three flexible opening models. 74

Figure 4-4: (a) Mean external and internal pressure coefficients, (b) maximum external and internal pressure coefficients, and (b) ratio of maximum net pressure coefficient to maximum external pressure coefficient as a function of wind direction. 77

Figure A-1: Pressure tap layout on wall CD of the WindEEE building model highlighting the four taps surrounding the opening that are used for the internal pressure model. All dimensions are shown in centimetres. ……. 92

Figure A-2: Averages between all trials of the difference between the experimental and simulated internal pressure coefficients using each of the four external pressure taps surrounding the opening. The coefficients are plotted vs. (a) normalized vortex location (y/r) and (b) wind direction at the opening (θ_o). ……... 93

Figure A-3: Ensemble-averaged mean, maximum, and minimum of external and internal dynamic pressure coefficients from all configurations using only the upper two of the four external pressure taps surrounding the opening. External pressure at the opening, simulated internal pressure from the SDE, and measured internal pressure inside the building plotted vs. (a) normalized vortex location (y/r) and (b) wind direction at the opening (θ_o). ……..…….. 95

Nomenclature

A	Area of opening
C_L	Loss coefficient through the opening
Cp	Pressure coefficient
Cp_e	External pressure coefficient
Cp_i	Internal pressure coefficient
$Cpi\ (exp)$	Measured (experimental) pressure coefficient
$Cpi\ (SDE)$	Simulated internal pressure coefficient
$\dot{C}p_i$	First time derivative of the internal pressure coefficient
$\ddot{C}p_i$	Second time derivative of the internal pressure coefficient
$\overline{Cp}_{\mathrm{y}}$	Ensemble-mean pressure coefficient at vortex location y
$\overline{Cp}_{\theta}$	Ensemble-mean pressure coefficient at wind direction θ
F	Ratio of maximum net pressure to maximum external pressure
f	Frequency
f_H	Helmholtz (natural) frequency
GCp_e	Peak external pressure coefficient
g	Force of gravity
h	Tornado simulator inflow depth
j	Time step
l_e	Length of air slug
l_o	Building model wall thickness
m	Number of openings
n_t	Number of WindEEE trials

n_y	Number of data points in set S_y
n_θ	Number of data points in set S_θ
P_0	Static pressure
p	Pressure
p_a	Aerodynamic pressure
p_e	External pressure
p_i	Internal pressure
$\dot{p}_i$	First time derivative of the internal pressure
$\ddot{p}_i$	Second time derivative of the internal pressure
p_{net}	Net pressure
$p_{net,fail}$	Garage door net failure pressure
p_s	Tornado static pressure
Q	Flow rate per unit axial length
r	Vortex radius (of maximum winds)
r_0	Updraft radius
S	Swirl ratio
S_y	Set of tornado locations for ensemble at y
S_θ	Set of wind directions for ensemble at θ
$S(f)$	Spectra
s	Length
t	Time
U	Fluid velocity
U_H	Wind velocity at roof height
V	Horizontal wind velocity

$V_{3s,fail}$	Garage door failure wind speed
V_{ma}	Moving average wind velocity
V_0	Internal volume
V_r	Radial wind velocity
V_t	Translational wind velocity
V_θ	Tangential wind velocity
x	Position of the air slug
$\dot{x}$	First time derivative of the position of the air slug
$\ddot{x}$	Second time derivative of the position of the air slug
x/r	Normalized vortex location along the x-axis
Y	Specific vortex location along y-axis
y	Vortex location along y-axis
y/r	Normalized vortex location along the y-axis
z	Height
Γ_{max}	Maximum circulation in the flow
γ	Ratio of the specific heat of air
Θ	Specific wind direction
θ	Wind direction
θ_o	Wind direction at the opening
ρ	Density of air
σ^2	Variance

1. Introduction

1.1 Background

Severe wind events such as tornadoes pose a significant threat to lives and infrastructure in Canada and the United States. Canada averaged 62 reported tornadoes per year from 1980 to 2009 and modelling techniques estimate that this number is well over 200 when unreported tornadoes are included (Sills et al., 2012). Residential houses make up a large portion of the costs in damage as they are so often affected by these events, yet not designed for them (Cheng, 2004).

The most common way of classifying tornadoes and assessing their damage in North America, is with the Enhanced Fujita (EF) Scale, which was developed by Texas Tech University (McDonald and Mehta, 2006), who modified the original Fujita Scale (Fujita, 1971). Because tornado wind speeds are difficult to measure directly, the speeds are estimated with the EF-Scale by evaluating damage done to man-made and natural structures, known as damage indicators (DIs). The damage to typically-constructed one- or two- family residences (labelled as FR12) is used as one of these DIs in the scale. For each DI, different degrees of damage (DODs) are provided, where each DOD is numbered in ascending order from the lightest damage to the most severe. Table 1-1 provides the DODs for FR12. Examining Table 1-1, uplift of roof deck and loss of significant roof covering material are grouped together with the inward collapse of single/double garage doors at DOD4, occurring at estimated wind speeds ranging from 130-185 km/h. Broken glass in doors and windows are estimated to occur for DOD3 at almost the same wind speed range. Complete failure of the roof structure is, hence, usually preceded by a significant opening in the structure such as a broken window or a collapsed garage door, due to increasing the internal pressures (Morrison et al., 2014).

One of the reasons internal pressures are of such interest in wind engineering is that low-rise buildings and residential structures can have loads on their roofs significantly increased when internal pressures are created because of large openings in the structure caused by debris damage or pressures in severe winds. A common way this occurs is when shingles and sheathing enter the debris field and penetrate doors and windows (Minor, 1994). These significant openings can more than double the risk of roof failure, according to work done by Kezele (1989). This is a

critical point as failure of the roof structure, or even just failure of smaller sections of roof structure or sheathing, can be financially devastating as it allows rain and wind to enter the building (Sparks et al., 1994).

Table 1-1: EF-Scale DOD descriptions and wind speeds for FR12 (Environment Canada, 2014).

DOD	Damage Description	Expected Value (km/h)	Lower Bound Value (km/h)	Upper Bound Value (km/h)
1	Threshold of visible damage	105	85	130
2	Loss of roof covering material (up to 20%), gutters and/or awning; loss of vinyl or metal siding	125	100	155
3	Broken glass in doors and windows	155	125	185
4	Uplift of roof deck and loss of significant roof covering material (more than 20%); collapse of chimney; garage doors collapse inward; failure of porch or carport	155	130	185
5	Entire house shifts off foundation	195	165	225
6	Large sections of roof structure removed (more than 50%); most walls remain standing	195	165	230
7	Exterior walls collapsed	210	180	245
8	Most walls collapsed, except small interior rooms	245	205	285
9	All walls collapsed	275	230	320
10	Destruction of engineered and/or well-constructed residence; slab swept clean	320	265	355

Garage doors may generate especially large internal pressures when they fail and increase the potential for further damage because of their large size relative to the internal volumes they

typically enclose. As a result, roofs of residential structures have a high probability of failure in storms that are strong enough to cause failure of component and cladding elements on the walls such as windows and garage doors. When assessing tornado damage of residential construction in Vaughan, ON, in 2009, Morrison et al. (2014) noted that roof failures were highly correlated to failures of these elements.

To help understand the internal pressures in residential structures that follow cladding failures and typically precede roof failures, internal pressure modelling can be used. This allows for better understanding of the wind-induced internal pressures in a structure using external pressures around the openings, without having to measure the internal pressures directly. A limitation of internal pressure modelling is that the vast majority of models deal with atmospheric boundary layer (ABL) or straight-line winds, as opposed to tornadic winds. The terms ABL and straight-line winds are often used interchangeably. Due to the still developing knowledge of the intricate differences between ABL and tornadic wind, work has only recently begun on simulating internal pressures in structures from tornado-induced external pressures. More research still needs to be done to determine the feasibility of simulating internal pressures in non-ABL winds flows, which will improve the overall understanding of how internal pressures behave in tornadoes.

Another issue arises when testing and modelling garage door failures. The difficulty here is that air leakage around the relatively flexible garage doors generates internal pressure changes during strong winds, even when the doors have not failed. Consequently, net loading on doors not only depends on the external pressure applied by the damaging winds, but includes the complexity of changes to the internal pressures. As a result of this, as well as the fact that not all garage door types may perform the same way or resist similar wind pressures, there may be significant variability in the performance and impacts of garage door failures.

1.2 Literature Review

1.2.1 Theoretical Model for Internal Pressures

Numerous studies have examined the effects of internal pressures on low-rise structures. These studies date back at least to Irminger and Nokkentved (1930), who measured internal pressures

on small building models in Denmark. Liu (1975) was one of the first studies to use flow rate equations to compare measured and simulated internal pressures. Holmes (1980) was the first to introduce the Helmholtz resonator model, used in this study. The following derivation follows the work of Oh et al. (2007) and several others who built on Holmes' foundation of the internal pressure model.

To understand internal pressures, a starting point is the Bernoulli equation for unsteady fluid flow along a streamline (Oh et al., 2007). Depicted in Figure 1-1, the equation is:

$$\rho \int_1^2 \frac{\delta U}{\delta t} ds + \int_1^2 dp + 0.5\rho(U_2^2 - U_1^2) + \rho g(z_2 - z_1) = 0 \qquad \textbf{(1)}$$

where the first term represents the unsteady term, the second term represents the change in pressure of the flow, the third term represents the change in velocity, and the fourth term represents the change in height. This equation assumes incompressible, inviscid, isothermal flow. Refer to the Nomenclature for descriptions of each variable.

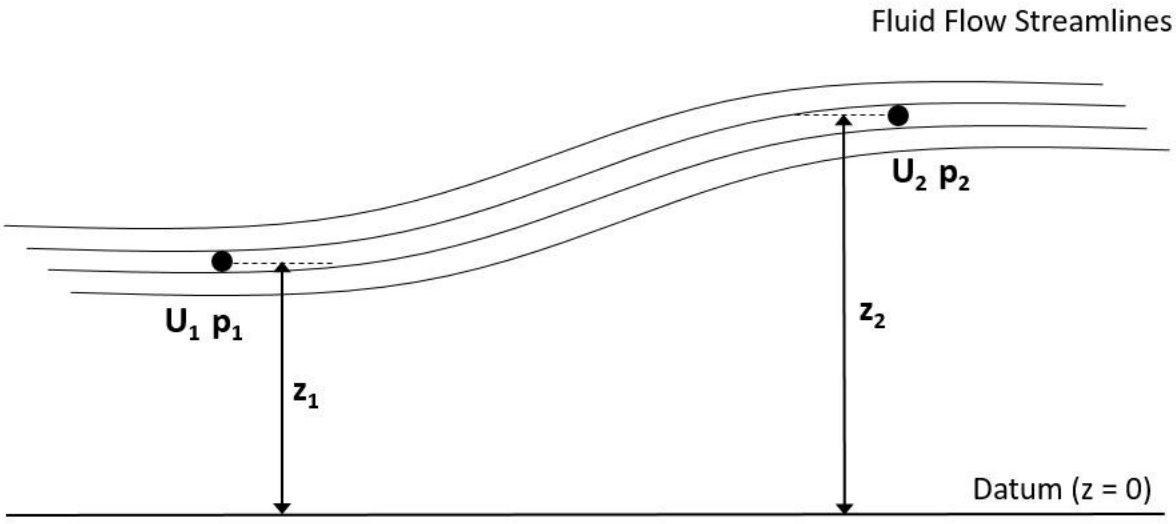

Figure 1-1: A representation of the Bernoulli equation showing velocity, pressure, and relative height at two locations along fluid flow streamlines.

Spatially-uniform internal pressures arise when an opening (or several) in a sufficiently large volume allow fluid flow (in this case, wind) to enter that volume. Using the Helmholtz resonator

concept, changes in the fluid flow, i.e., the external pressure, along with resonance instability, cause a defined "slug of air" to move in and out of the opening, as shown in Figure 1-2 (Holmes, 2015). If assumptions are made that there is no net flow and that the internal pressure inside the volume is approximately uniform, this leads to the following equation for the movement of the air slug (Oh et al., 2007):

$$\rho l_e \ddot{x} + C_L \rho \frac{\dot{x}|\dot{x}|}{2} = p_e - p_i \tag{2}$$

This equation is related to the equation of a single degree of freedom spring-mass-damping system, where the slug of air is the mass (Holmes, 1980). In the equation: x is the position of the slug of air, l_e is the length of the slug of air, and C_L is an added constant for the loss coefficient through the opening. This equation can be expressed in terms of pressure coefficients, instead of air slug position, as the single discharge equation (SDE) (Oh et al., 2007):

$$\frac{\rho l_e V_0}{\gamma A P_0} \ddot{C}p_i + \left(\frac{\rho V_0 U_H}{2\gamma A P_0}\right)^2 C_L \dot{C}p_i |\dot{C}p_i| + Cp_i = Cp_e \tag{3}$$

which will be further discussed in Chapter 2 of this study.

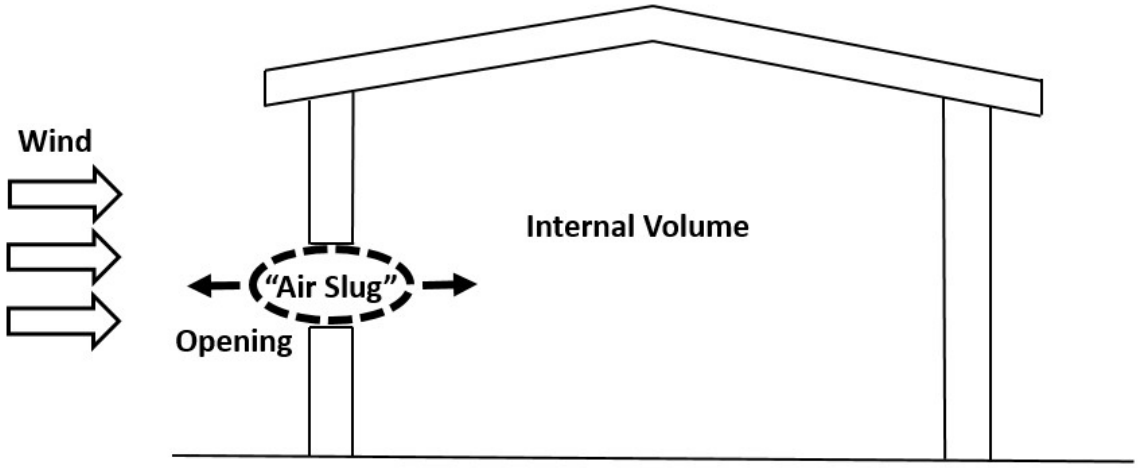

Figure 1-2: The Helmholtz resonator model for a building with a single dominant opening (after Holmes, 2015).

After being introduced by Holmes (1980), The Helmholtz resonator model was used to aid in simulating internal pressures from external pressures in many studies throughout the years. These studies include Vickery (1986), Pearce and Sykes (1999), Ginger (2000), and many others. The internal pressure model was further refined by Oh et al. (2007), who used the SDE to simulate internal pressures in the National Institute of Standards and Technology (NIST) aerodynamic database and compared them to measured internal pressures from the database. Oh et al. (2007) found that, for the case of ABL flows, simulated internal pressures using computational models had high accuracy for buildings with a large, centrally-located, dominant opening. They concluded that the model has sufficient accuracy such that it could replace direct measurements in wind tunnel experiments as long as the external pressures at the location of the opening are known.

1.2.2 Internal Pressures in Tornadoes

One thing that almost all of the past internal pressure model studies share in common, is that the pressure data being analyzed is from ABL winds, as opposed to tornadic winds, which have been studied to a lesser extent. Tornadic winds add increased complexities to the wind field due to factors such as the vertical wind component, static pressure drop in the core, and the non-uniform nature of mean wind velocities and directions as the vortex passes over or past a building. Even in recent research, many studies have used boundary layer wind tunnel results to evaluate wind loads in tornadoes, and some current design guidelines use multiplication factors applied to ABL wind loads to account for the differences in the wind effects (e.g., ASCE/SEI 7-16 (2017)). However, some studies have shown that current building codes designed using ABL winds are not sufficient for tornadic winds (e.g., Haan et al., 2010), although this is still a source of debate.

Most of the experimental research on tornado-induced internal pressures in structures has been done in the past decade due to the relatively recent development of tornado simulators. A list of these studies can be found in Table 1-2. One of the earliest simulators to produce relevant data was the ISU Tornado Simulator at Iowa State University, where the testing by Sarkar and Kikitsu (2009), Kikitsu et al. (2011), and Thampi et al. (2011) were conducted. All three of these studies examined internal pressures in low-rise buildings from a translating vortex, to some extent;

however, Kikitsu et al. (2011) did not produce a paper and Thampi et al. (2011) mainly focused on finite element analysis with only a section of the work on experimental testing. No internal pressure modelling was included in these studies, such as the model present in Oh et al. (2007). However, Auburn University is currently conducting research in this area using data from Kikitsu et al. (2011) and Thampi et al. (2011).

Table 1-2: Summary of previous research on tornado-induced internal pressures.

Author	**Year**	**Building Scale**	**p_i Model**	**Vortex Translation**	**Building Location**	**Core Radius**
Sarkar and Kikitsu	2009	1/250	No	0.15 m/s	Centreline	530 mm
Kikitsu et al.	2011	1/250	No	0.15 m/s	Centreline	530 mm
Thampi et al.	2011	1/75	No	0.3 m/s	$1.42r$	530 mm
Rajasekharan et al.	2013	1/1000	No	No	0 - $2.7r$	36 mm
Sabareesh et al.	2013	1/1000	No	No	Centreline	36 mm
Letchford et al.	2015	1/1000	Yes	No	0 - $4.7r$	190 mm
Wang et al.	2017	1/300	No	No	0 - $1.55r$	50 mm
Sabareesh et al.	2019	1/1000	No	0.02-0.24 m/s	Centreline	36 mm
Roueche et al.	2020	1/100	Yes	0.61 m/s	Centreline	14, 41 mm

* p_i = internal pressure; r = vortex core radius

Using the tornado simulator at Tokyo Polytechnic University, Rajasekharan et al. (2013) examined the characteristics of internal pressures on a low-rise building and Sabareesh et al. (2013) studied the effects of ground roughness on internal pressures in a cubic building. Similarly, Wang et al. (2017) analyzed tornado-induced internal pressures in a cubic building with additional opening size and orientation configurations in a tornado simulator at Tongji

University. Once again, these studies only measured internal pressures and did not attempt to use them to validate an internal pressure model. Therefore, one cannot discern if there are effects which may or may not negate the use of the existing internal pressure models.

Letchford et al. (2015) examined internal pressure dynamics using the larger, more advanced tornado simulator at Texas Tech University and included a numerical model for the internal pressures. However, validating the numerical model was not the primary goal of this paper, and although the simulated and measured spectra were compared, the internal pressures time histories and other statistics were not. Additionally, all of the referenced studies, with the exception of the Iowa State University studies, only examined pressures induced by a stationary vortex, as few tornado simulators are capable of producing a translating vortex. This is important to note as many subsequent studies (e.g., Feng and Chen (2018) and Haan (2017)) have revealed differences in the pressure distributions on buildings between a stationary and translating tornado. This means there is still a need for studies that pertain to simulating internal pressure in tornadic winds from a translating vortex.

During the work of this thesis, several newer studies with increasing relevancy to this topic have been produced. Another paper was published from work at the Tokyo Polytechnic University tornado simulator, this time with a translating vortex, in Sabareesh et al. (2019). This study examined the effects of various tornado translation speeds and opening configurations on the external and internal pressures acting on the roof and walls of a low-rise structure. Even more recently, Roueche et al. (2020) examined differences in past tornadic and straight-line wind tunnel studies with the help of internal pressure modelling. The tornadic experimental data for that study was published in Haan et al. (2010). However, it should be noted that internal pressures were not measured in either of those two studies.

Many key findings were made regarding internal pressures in the mentioned studies, which are listed in Table 1-2. Overall, peak internal pressures from tornadoes were shown to be significantly higher than peak pressures for straight-line winds; however, much of this can be explained by the static pressure of the vortex (Haan, 2017). These differences were most notable in the vortex core (Letchford et al., 2015), where both opening size and orientation played a large role in the internal pressures (Want et al., 2017). Furthermore, Sabareesh et al. (2019) showed

that the translation speed of a tornado is positively correlated with the size of internal pressure fluctuations for buildings with dominant openings. Roueche et al. (2020) found that, overall, simulated internal pressures from tornadoes behaved similarly to those from straight-line winds, when excluding the static pressure drop from the vortex, although it was acknowledged that more work needed to be done in that area. These studies showed the key differences in internal pressures in tornado simulators compared to ABL winds, but also that there might be ways to mitigate these differences in analysis, such as removal of the static pressure of the tornado.

1.2.3 Internal Pressures with Variable Openings

A missing feature in all of the previously mentioned studies, and internal pressure modelling in general, is the inclusion of a variable or fluctuating opening size. This applies to the situation of garage doors and their failures in severe winds. This is a crucial aspect of internal pressure research, as garage doors are commonly one of the key elements of a wood-frame structure's envelope to fail, leading to the increased internal pressures and likelihood of roof uplift (Dao et al., 2014). What complicates this analysis is that garage doors are flexible, to varying degrees, and therefore will not have a constant opening size as they bend under severe wind before failure. This makes accurate analysis of their failure wind speeds complex.

Although several papers have made observations regarding garage door failures from data gathered during tornado damage surveys (e.g., Pan et al. (2002) and Morrison et al. (2014)), there have been few published studies on different garage door failure mechanisms and capacities. Pressure testing of garage doors for wind-resistance rating is typically conducted using standardized procedures such as ASTM E1233 (ASTM, 2006) and ASTM E330/E330M (ASTM, 2014) in order to evaluate their structural performance in the form of applied load-deflection (or pressure-deflection) curves.

Following a similar approach, Shen et al. (2017) developed a full-scale simulator employing a diesel-powered fan capable of generating a maximum pressure of 22 kPa. A set of large sectional doors were tested in that study by applying a recreated pressure time history based on boundary layer wind tunnel measurements and calculated using the wind pressure coefficient (Cp) data from a building model archived in the NIST aerodynamic database (Ho et al., 2005). Shen et al. (2017) provided detailed descriptions of the observed failure mechanisms for these industrial

doors and their midspan deflections due to the applied negative (outward-acting) pressures (as opposed to positive pressures). However, the primary focus of the study lies in the fidelity of the simulator to apply and follow a pressure time history converted from a predetermined wind velocity time history and adopting the maximum Cp_e recorded from the aforementioned wind tunnel model. Therefore, as with all other experimental evaluations of the structural performance of garage doors, details of their behaviour are presented in terms of load-displacement curves, and the effects of the induced internal pressurization on Cp, caused by the inflow of air around the deflected areas, were not examined.

In an ideal case with the garage door being rigid and sealed, the net pressure would be virtually the same as the external pressure and internal pressure modelling would not be necessary. However, the difficulty lies in the fact that garage doors are flexible, which could lead to larger internal pressures pushing back against the door, as the door begins to bend inwards under a positive wind load. To further complicate the analysis, the opening size of the door - frame interface is constantly changing. As the load increases, the opening increases as well. The larger opening then allows for higher internal pressures to develop, which subsequently helps to close the opening, creating a complex pattern of loading. Because the specific failure mechanisms and related maximum wind pressures are not well defined due to the vast variety of garage door types available in the market (e.g., wood, 1 to 3-layer steel, fiberglass, etc.), their wind-resistance and behaviour may vary widely from one type to another. This will have an impact on the resulting range of wind speeds and, therefore, the EF-Scale.

1.3 Objectives

This study has two main sections, each revolving around a crucial component of internal pressure modelling for low-rise structures in tornadoes. The first section focusses on understanding if the unique details of tornadic wind fields alter the dynamics of internal pressures. The second section focusses on estimating failure wind speeds of garage doors using the internal pressure model studied in the first section. The primary goal of this study is to understand and simulate internal pressures in tornadoes.

The first part of this thesis involves a computational study of simulated and measured internal pressures using an existing data set of tornadic winds on a model building. The specific data set

being studied was gathered by, then PhD candidate, Chieh-Hsun Wu, at the University of Western Ontario's (UWO) Wind Engineering, Energy and Environment (WindEEE) Dome facility in 2016. The WindEEE Dome is one of the first wind tunnel facilities, worldwide, capable of producing tornado and downburst like winds at reasonable wind tunnel scales. In this study, wind tunnel tests of a simulated tornado that translated past a 1:50 scale pressure model low-rise building were examined. The model structure is similar to the one used for the UWO contribution to the NIST aerodynamic database, discussed in Ho et al. (2005). The data gathered from the WindEEE Dome tests include external and internal pressures on the building model, as well as wind speeds and directions measured by four Cobra probes located around the building.

The specific objective of the first part of the current study is to use the theoretical model to simulate the internal pressures in the building from the given tornadic external pressures at a dominant opening, and compare these to the actual internal pressures that were measured in testing. This will determine the feasibility of simulating internal pressures in non-ABL winds. The hypothesis is that, if the tornadic wind field alters the internal pressure dynamics, (i) the theoretical model would be less able to calculate the actual internal pressures, and (ii) the pressure coefficients would be significantly different than those for ABLs.

The second part of this study is driven by a lack of literature on internal pressures for variable openings, and limitations of garage door data, particularly that these studies only determine the net pressure being applied to the door while the fluctuating open area of the door - frame interface remains unknown. This is crucial because the external pressure acting on the door is needed to make an estimation for the failure wind speed, and this cannot be obtained without knowledge of the internal pressure. As mentioned earlier, the flexible garage door and resulting variable opening size create a complex pattern of loading that make proper analysis of the garage door wind resistance difficult to assess.

The specific objectives of the second part of this study are to determine the wind speeds required to generate garage door failures due to the applied pressures (neglecting the effects of debris impact) and to compare the results to DOD4 of FR12 in the EF-Scale. To achieve this goal, the capacities and failure mechanisms of six garage doors of various types are obtained from experimental full-scale PLA testing performed by former research student, Alexander Riveros.

The maximum wind speeds sustained by each door are evaluated using net pressure coefficients estimated from the open areas generated by the deflection of the loaded doors, in order to account for the effects of varying internal pressurization. Both parts of this study contribute to understanding and simulating internal pressures in tornadoes.

2. Methodology and Data

Most of the methodology in this study is either directly from or related to past studies that are an essential part to this thesis. The tornadic wind tunnel testing (Section 2.1) was performed by Kopp and Wu (2020), the full-scale garage door tests (Section 2.2) were performed by Alexander Riveros, as reported in Jaffe et al. (2019), and the internal pressure model approach (Section 2.3) is similar to that used by Oh et al. (2007). Each of these items is discussed in detail in this chapter.

2.1 Wind Tunnel Testing

The testing for this portion of the study was performed at UWO's WindEEE Dome by Kopp and Wu (2020). This hexagonally shaped facility is able to simulate a multitude of unique wind fields, such as tornadoes, with the use of its specialized fans located on all six sides of, and above, the test chamber. The chamber is 25 m in diameter, making it significantly larger than the tornado simulators discussed in the literature review. The structure tested was a 1:50 scale pressure model of the Texas Tech University 'WERFL' Building (Levitan and Mehta 1992a, 1992b; Smith 2010). The low-rise structure model had dimensions of 18.3 cm by 27.5 cm, an eave height of 7.8 cm, and a roof slope of ¼:12 (Kopp and Wu, 2020). The building also had a dominant opening, measuring 4.5 cm high by 2.5 cm wide, located near the centre of one of the long walls. This opening represents a significant opening on a low-rise structure, such as a broken door or window. The surface terrain of the WindEEE Dome was set as nominally smooth for the experiments. A photo and diagram of the building can be seen in Figure 2-1.

The building model contained 204 external pressure taps, uniformly-distributed on the walls and roof, as well as two internal pressure taps, located at either end of the building. The reference pressure was measured in the bellmouth chamber above the building, as this pressure does not change during the translation of the vortex. The building was placed off-centre in the test chamber, while the vortex was translated down the centre of the chamber, resulting in the building being located approximately at the radius of maximum winds (Figure 2-2).

(a)

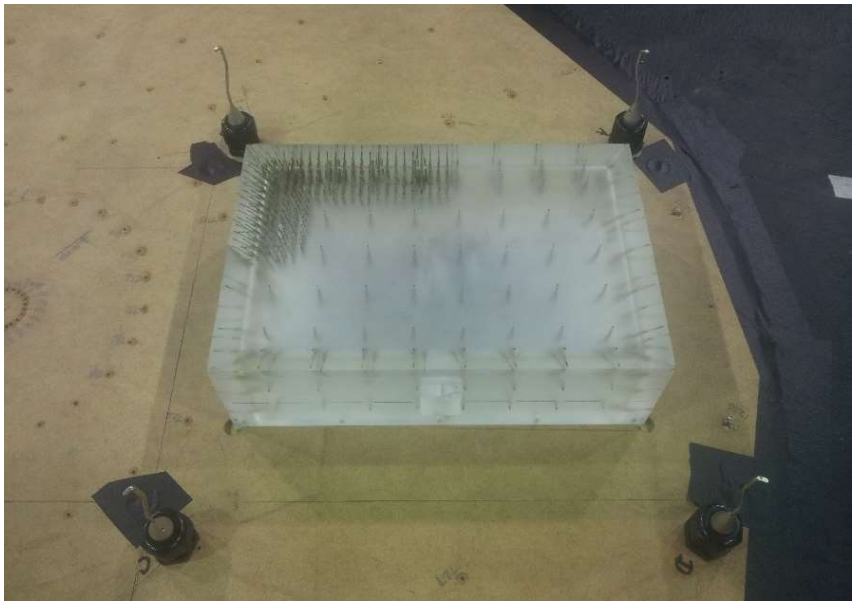

(b)

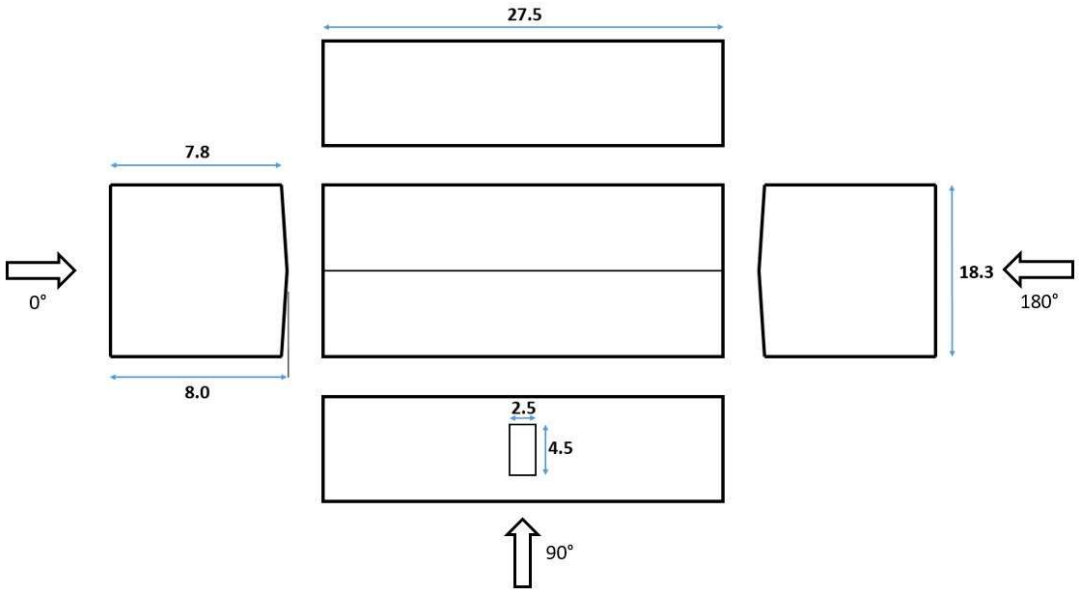

Figure 2-1: (a) Photo of the building model in the wind tunnel and (b) exploded view of the building showing the dimensions of the structure and its opening in centimetres along with wind directions (after Kopp and Wu, 2020).

The vortex had a core diameter of 0.8 m, a translation speed of 0.057 m/s, and a swirl ratio of 0.76. The swirl ratio is defined in Refan and Hangan (2018) as: $S = r_0\Gamma_{max}/(2Qh)$, where r_0 is the updraft radius, Γ_{max} is the maximum circulation in the flow, Q is the flow rate per unit axial length, and h is the inflow depth. At this swirl ratio, the tornado-like vortex was made up of

several sub-vortices swirling around the common centre. The vortex to building ratio was small enough that the experiment was not a recreation of straight-line-like winds, and the ratio of the translation speed to vortex rotational speed was low, relative to typical full-scale ratios. The vortex was translated approximately 4000 mm, with y measuring the relative location of the vortex to the centre of the building. Therefore, y = -2000 mm represented the start of the vortex translation, y = 2000 mm represented the end of the translation, and y = 0 represented the vortex directly over the building's y-axis location. The location of the vortex was taken as the location of the centre of the translating bellmouth, as this was the easiest way to accurately approximate the centre of the vortex. The vortex location was also normalized by its radius of maximum winds, r (Kopp and Wu, 2020).

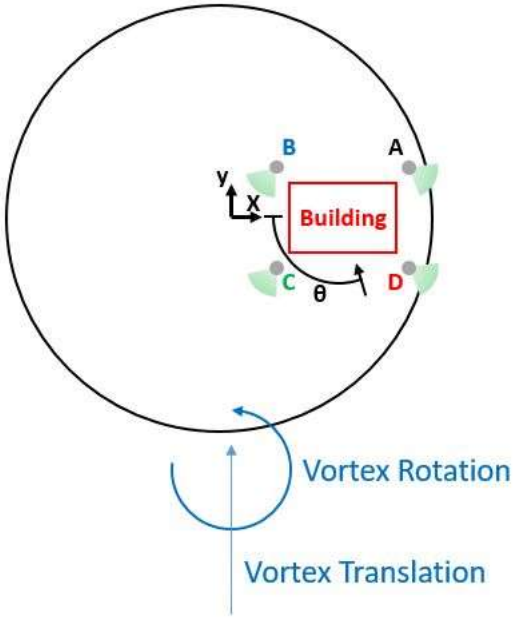

Figure 2-2: Diagram showing the location of the building, the location and orientation of the Cobra probes, and the direction of vortex translation and rotation (after Kopp and Wu, 2020).

The building was surrounded by four Cobra probes, shown in Figure 2-2 as grey dots, placed 72 mm from each corner (51 mm in each of the x and y directions) of the building at a height of 98 mm to measure wind speeds in various directions when the probes were windward. The probes were labelled A through D, starting in the upper-right and moving counter-clockwise. These

labels are also used to describe corners and walls of the building. For example, corner B would be the upper-right corner of the building, near probe B, and wall CD would be the wall with the opening that runs between corners C and D. The wind direction, θ, is defined as 0° when the wind is blowing in the positive x-direction, 90° when the wind is blowing in the positive y-direction, and 180° when the wind is blowing in the negative x-direction. Each probe has an 80° acceptance range (i.e., ± 40°) with probes A and D roughly meant to capture winds as the vortex approached the building, and probes B and C to capture winds after the vortex passed by the building. For example, Figure 2-2 shows a setup with probes A and D set to 150°, meaning they could measure winds between 110° and 190°. This is represented by the green cones extending from the Cobra probes in the sketch.

Table 2-1: Parameters of the experimental setup in the WindEEE Dome tests (after Kopp and Wu, 2020).

Building Model and Vortex Details					
Building Dimensions	275 x 183 x 78 mm				
Vortex Radius (of maximum winds)	400 mm				
Vortex Swirl Radio	0.76				
Vortex Translation Speed	57 mm/s				
Vortex Translation Length	4000 mm				
Cobra Probe Configurations					
Configuration	Cobra Probe Orientation				Trials
	Probe A	Probe B	Probe C	Probe D	
I	150°	50°	50°	150°	29
II	130°	50°	50°	130°	29
III	110°	50°	50°	110°	30

The WindEEE Dome testing was divided into three configurations, which had the Cobra probes facing different directions. The purpose of these configurations was to capture various wind velocities caused by the vortex, seeing as the probes could only measure accurately over a narrow acceptance band. Since this study is primarily concerned with the pressures on the building, and not the wind velocities measured by the probes, there is rarely a need to differentiate between the configurations. Each configuration had 30 nominal trials with a total of 88 trials that each produced 120 seconds of external and internal pressure time histories at a rate of 500 samples/sec. These were the cases also examined in detail by Kopp and Wu (2020), who only discussed the external pressure data. Table 2-1 summarizes general parameters of the testing and specific information for the three configurations. The reader is referred to Kopp and Wu (2020) for further details.

2.2 Full-Scale Garage Door Testing

2.2.1 Experimental Setup

The pressure test set-up developed to determine the capacities and deflections of the multiple garage doors is an extension of the method developed by Kopp and Gavanski (2011) and Miller et al. (2017). To determine the maximum net positive pressure that each of the garage doors can sustain and obtain displacement and pressure measurements, the experimental set-up (Figure 2-3) included the following three main components:

- A pressurization system consisting of six pressure load actuators (PLAs), as developed by Kopp et al. (2010) and Miller et al. (2017);
- An “air-box” or pressure chamber;
- A control/data acquisition system (DAQ) with linear variable differential transformers (LVDTs) and pressure transducers (PTs).

In these garage door tests, a system consisting of six PLAs was used to provide ramping positive pressures on each garage door by means of hoses connected to a large steel-framed wooden air-box upon which each of the garage doors was installed. To regulate and monitor the uniform ramping positive pressures inside the air-box, each PLA had a pressure transducer connected to the air-box. Additionally, 25 LVDTs, making contact with the specimen’s exposed surface, and

one pressure transducer coupled to the air-box, recorded the displacements and applied air pressures, respectively.

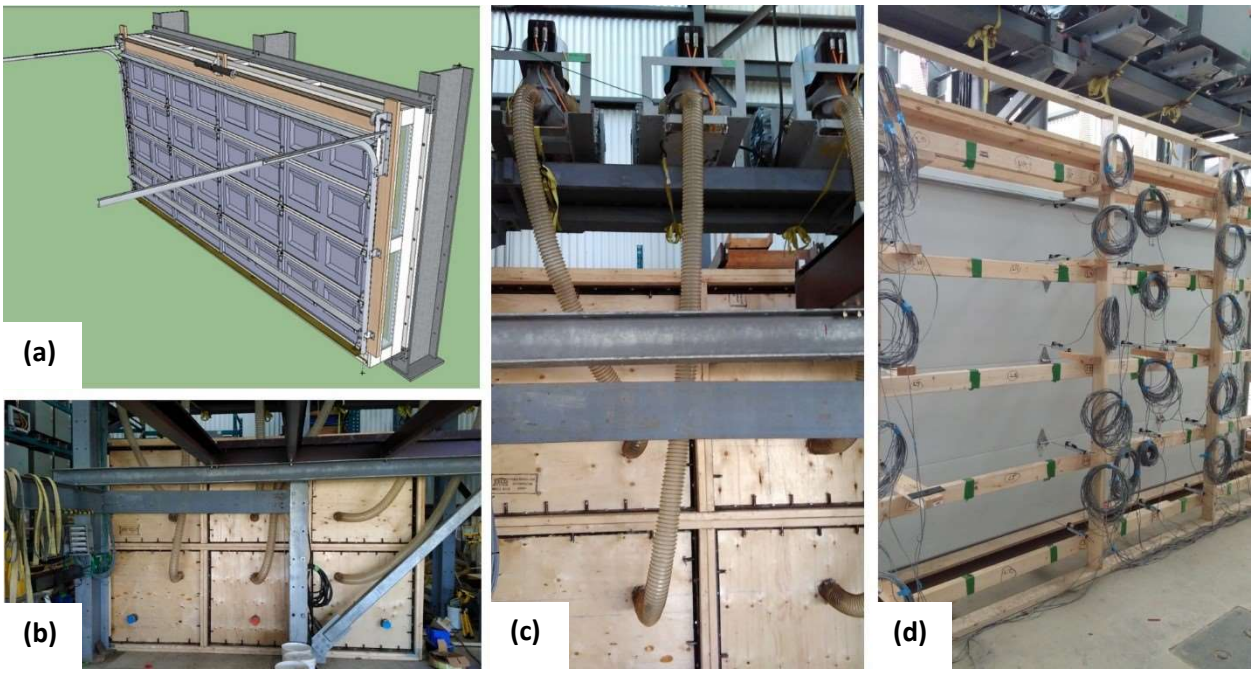

Figure 2-3: (a) A conceptual image of the pressure chamber setup, and photographs of (b) its backside with (c) detailed connections to PLAs and (d) the displacement transducer support frame.

In order to evaluate the behaviour of different garage door types in response to applied external pressures, a total of six garage doors were tested ranging across four different products. All of the doors were for residential use, 2.13 m by 3.66 m (7 ft by 12 ft) in size, with the common short raised-panel architectural design and tongue-and-groove connections between panels, and included standard mounting hardware, including 14-gauge steel hinges, 5.1 cm tracks made of 17-gauge galvanized steel, 13-gauge galvanized steel jamb brackets, and heavy-duty rollers. The four products of garage doors were of varying structural capacity, with Product 1 and Product 2 doors being 1-layer type construction and Product 3 and Product 4 doors consisting of stronger, 3-layer type construction.

During testing, a programmed static ramping load sequence with a maximum attainable positive pressure of 2 kPa was applied to the external surface of each door at a rate of 0.4 kPa/min by the

PLA system until failure occurred. The maximum pressure was selected only to ensure the applied load was high enough to cause failure while the loading rate ensured a steady transfer of the generated pressure to the door within the capabilities of the PLA system, while simultaneously ensuring close fidelity between the programmed ramping and the recorded pressures. Each test was controlled and monitored on a computer, with the pressure and displacement data being simultaneously recorded by the DAQ. The tests were manually terminated soon after failures were observed. More information about the experimental setup can be found in Jaffe et al. (2019).

2.2.2 Experimental Results

From the experimental results, Table 2-2 shows the failure mechanism, maximum net applied pressure, and maximum opening area of each garage door design. Note that the opening area was only tracked for Products 2 and 3, and that three Product 2 samples were tested. Based on these results, there is an evident difference in the structural behaviour and failure mechanisms for the single-layer and triple-layer products. Products 1 and 2 exhibited significant bending and plastic deformation that affected the doors' normal operation. In contrast, the respective fiberglass and steel shells of Products 3 and 4 seemed to provide increased resistance to permanent bending. However, the increased capacities increased the loading applied to the rollers, tracks, brackets, and fasteners. This generated pull-out failures and/or permanent deformation of such hardware. Consequently, single-layer garage doors seem to be more prone to local failures (i.e., permanent panel bending) than the stronger three-layer products, which produced pullout failures and roller disengagement due to their higher elastic range. Comparable modes of failure were reported by Shen et al. (2017) for the stronger and more elastic commercial sectional doors, for which local buckling of the U-bars and disengagement of door panels from tracks were the primary failures observed. Additional details of each garage door type failure can be found in Jaffe et al. (2019).

Using the applied net pressure and induced deflection data obtained for both garage door types, open area curves were developed by numerically integrating the deflection curves recorded at the side and top edges of each door. Figure 2-4 presents a conceptual description of a door's deflection curve at its top edge, depicting the open area as the integration of the curve. Note that

the openings at the bottom surface were neglected because these were covered by the floor making contact with the weather-stripping seal.

Table 2-2: Comparison of test results for garage door experiments.

Garage Door Design	Build (1-layer, 3-layer)	Failure Mechanism	Maximum Net Applied Pressure (kPa)	Maximum Opening Area (m^2)
Product 1	1-layer	Plastic deformation of door panels	0.42	Not Recorded
Product 2	1-layer	Plastic deformation of door panels	0.56 (average)	0.13 (average)
Product 3	3-layer	Plastic deformation of hardware and track pull-out	1.75	0.38
Product 4	3-layer	Plastic deformation of door panels, plastic deformation of hardware, and track pull-out	0.90	Not Recorded

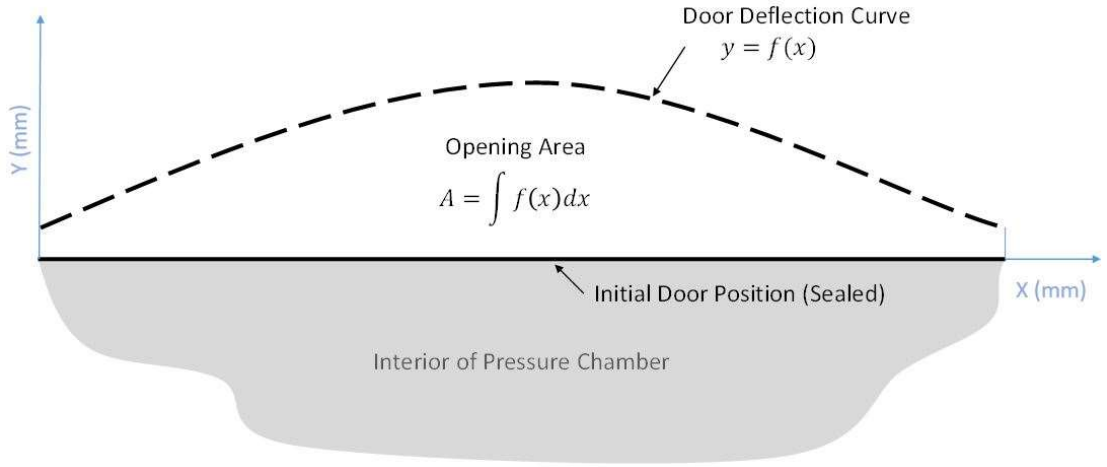

Figure 2-4: Conceptual image of a garage door deflection curve at its top edge. The opening area is equivalent to area under the curve.

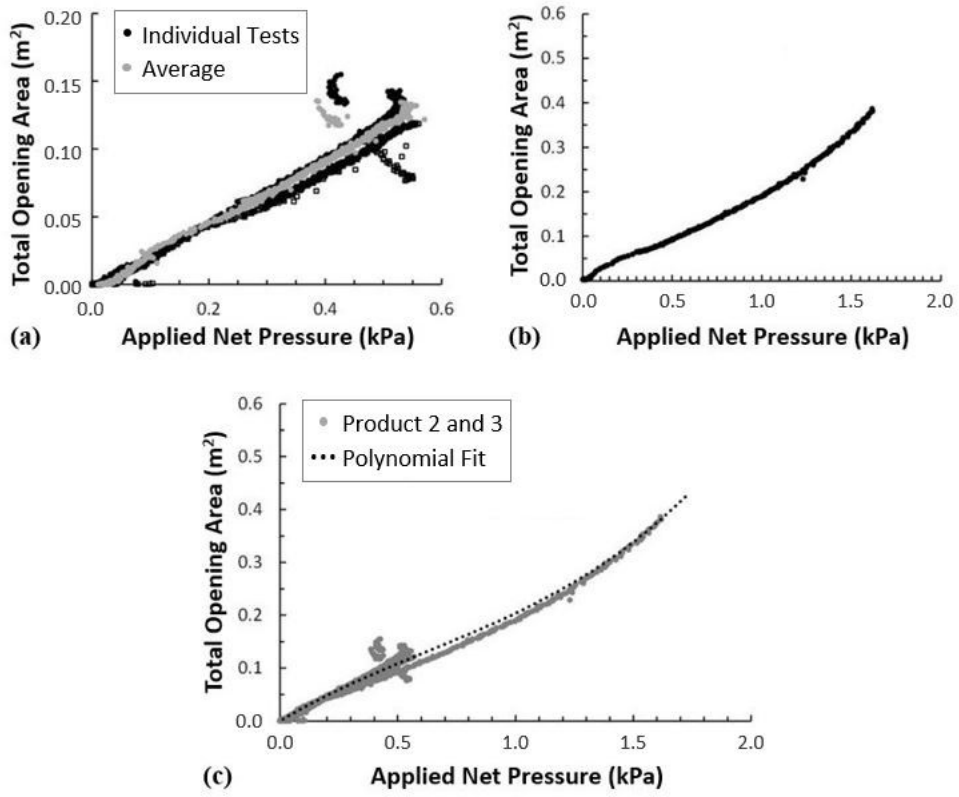

Figure 2-5: Total open area as a function of applied net pressure for (a) all three Product 2 doors tested, (b) Product 3, and (c) all samples for which displacement data were obtained.

Figure 2-5(a) shows the area of the opening versus applied net pressure for the three Product 2 tests, as well as an average between them; Figure 2-5(b) shows the same relationship for the Product 3 test, while Figure 2-5(c) shows the relationship for both door types on the same graph. A polynomial curve of best fit for the open area versus net pressure relationship is also provided in Figure 2-5(c). Despite the different properties of the two door types, the relationship between open area and applied net pressure follows a similar trend, seen in Figure 2-5(c). Thus, a larger maximum open area (0.38 m^2) was obtained for the stronger doors, which also exhibited the highest pressure capacity. Conversely, the weaker doors resulted in smaller open areas and failure because of the low pressure capacity. The similarity of the curves shows that the doors have similar stiffness despite their difference in strength and elastic range, and allows the

assumption of all the door samples having approximately the same open area versus net pressure relationship, for which a linear relationship will be used in Chapter 4.

2.3 Internal Pressure Modelling

2.3.1 Modelling for Tornadic Experiments

As mentioned, one of the goals of this study is to computationally simulate the internal pressures of a model building in a tornadic wind field, and compare these to the actual measured internal pressures. The key to the former is internal pressure modelling, which allows internal pressures to be calculated at each time interval throughout the experiment based on the instantaneous external pressures surrounding the openings. In this study, the theoretical model, used by Oh et al. (2007) to simulate internal pressures in ABL winds, is applied. The numerical model is validated by replicating the Oh et al. (2007) study, as shown later in this chapter.

The governing equation for this model is the SDE, which is based on the unsteady Bernoulli equation with the addition of a loss coefficient to account for friction and other losses. This yields the following equation, when put into discretized form:

$$\frac{\rho l_e V_0}{\gamma A P_0}\ddot{p}_i^j + \frac{C_L \rho {V_0}^2}{2\gamma^2 A^2 {P_0}^2}\dot{p}_i^j\left|\dot{p}_i^j\right| + p_i^j = p_e^j \qquad \textbf{(4)}$$

where p_i^j is the jth time step of the internal pressure, p_e^j is the jth time step of the external pressure, $\dot{p}_i^j$ is the first time derivative of the internal pressure, and $\ddot{p}_i^j$ is the second time derivative of the internal pressure. After performing numerical differentiation with a backward differencing approximation, and substituting in the known parameters, the only unknown variable becomes the internal pressure, p_i. The other parameters in the equation are constants, with values that can be found in Table 2-3. Note that several values could have been assumed for the effective length of the air slug, l_e, and loss coefficient, C_L. The values used here are taken from Oh et al. (2007) for consistency.

Table 2-3: List of variables in the SDE equation for WindEEE and garage door experiments.

Variable	Numerical Value for WindEEE (model-scale)	Numerical Value for Garage Door	Variable Name
ρ	1.23 kg/m^3	1.23 kg/m^3	Density of air
$\boldsymbol{l_e = l_0 + 0.89\sqrt{(A)}}$	0.0429 m	Fluctuating	Effective length of air slug
$\boldsymbol{l_0}$	0.0130 m	0.0508 m	Wall thickness of building
$\boldsymbol{V_0}$	0.00254 m^3	70 m^3	Internal volume of building
$\boldsymbol{P_0}$	10^5 Pa	10^5 Pa	Static pressure
A	0.00112 m^2	Fluctuating	Area of opening
$\boldsymbol{\gamma}$	1.4	1.4	Ratio of specific heat of air
$\boldsymbol{C_L}$	2.5	2.5	Loss coefficient

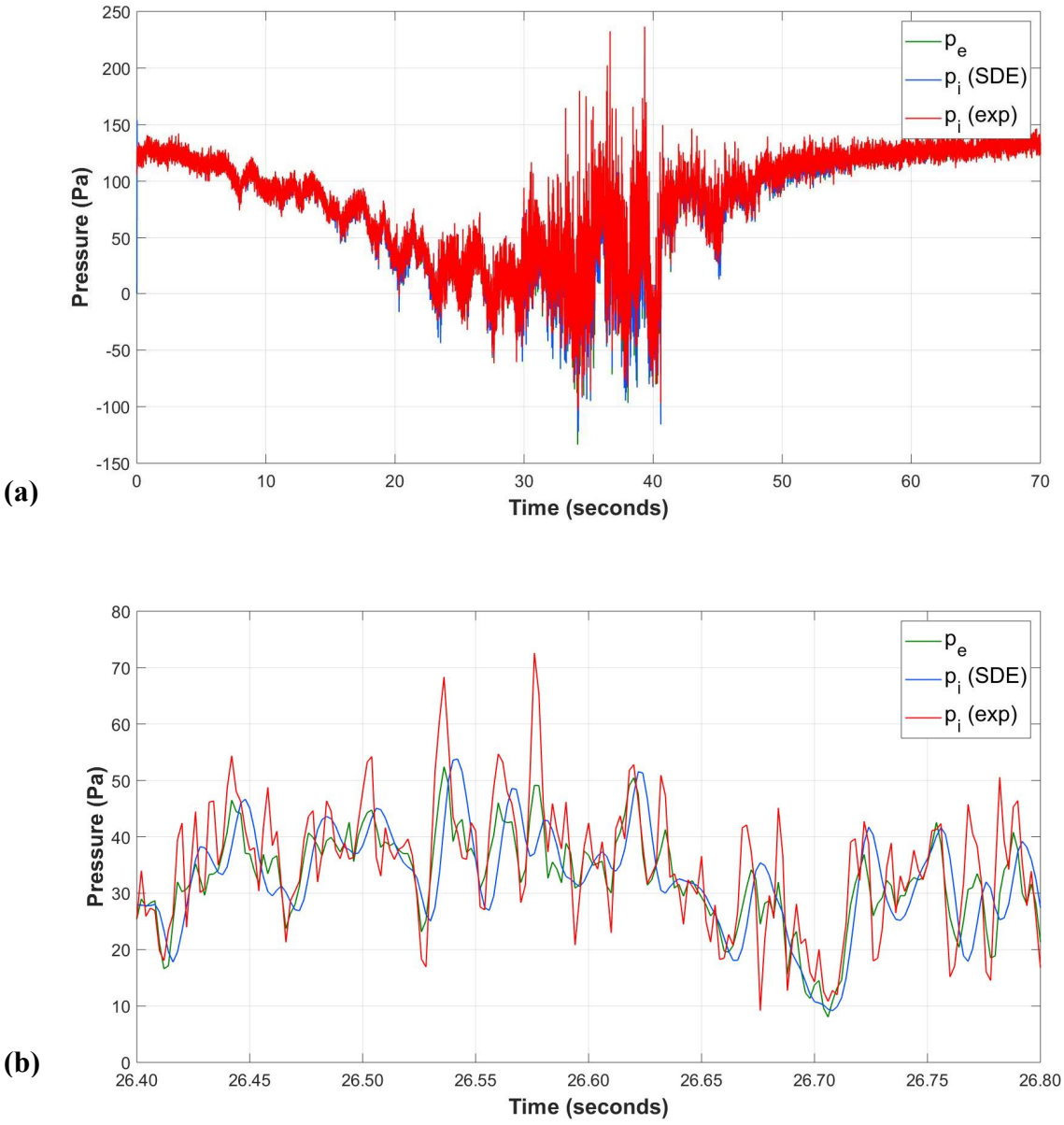

Figure 2-6: Sample time history showing the external pressure at the opening, the simulated internal pressure from the SDE, and the measured internal pressure inside the building for (a) a full trial duration and (b) a section of the trial.

As shown by Eq. (4), the simulated internal pressure at each time step is computed by inputting the current external pressure at the opening, along with the previous time steps of the internal pressure. This external pressure is taken as an area average of the four external pressures taps immediately surrounding the dominant opening. Due to their uniform spacing around the opening, the inputted external pressure value ends up being a simple equally-weighted average of

these four taps. The two internal pressure taps, located at either end of the building, have similar pressure values with time, and the measured internal pressure value used for comparison is simply an average of these two taps. Sample time histories showing the external pressure, simulated internal pressure, and measured internal pressure are shown in Figure 2-6. Measured external pressures are shown in green, simulated internal pressures are shown in blue, and measured internal pressures are shown in red. The results will be examined in detail in Chapter 3.

2.3.2 Modelling for Garage Door Experiments

As mentioned in the introduction, pressure testing alone is not enough to accurately estimate the failure wind speeds of garage doors. Due to the flexibility of the garage door, it is the net pressure that is obtained at failure, not the external pressure. However, it is the external pressure that is more directly correlated with the wind speed. Thus, the internal pressure for a given external pressure (and building geometry) is needed. Of course, the passage of a tornado is unsteady, and the flow is turbulent, so both the external and internal pressures are fluctuating. The approach here is to examine the ratios of net pressure to external pressure during the moments of peak loading (i.e., peak gusts), incorporating the effects of garage door flexibility, and then using these ratios as part of the estimation of the failure wind speeds, which are examined in Chapter 4.

Once again, the theoretical internal pressure model is used. Although this model has been validated for ABL winds, this thesis shows that it can reasonably be applied to tornadic winds as well. Therefore, the common assumption is made that, if the tornado is large relative to the structure of study (a garage in this case), this method should be sufficiently accurate within the other variabilities and uncertainties of the problem, particularly since the only purpose is to relate the net wall pressure to the wind speed.

For this section of the study, there are two governing equations, or sets of equations, for the internal pressure model. The first is the SDE, already discussed, and the second is the multiple discharge equations (MDE), also based on the unsteady Bernoulli equation. For the SDE, although the equation is the same as Eq. (4), the open area, A, is an additional unknown to the internal pressure for the flexible garage door cases. The effective length of the air slug, l_e, is also

changing, but it is assumed to be directly related to the area. Table 2-3 summarizes the various parameters for the garage door model, as several of them are different from the WindEEE model.

When dealing with multiple openings, the MDE method is used. In this case, there are a series of equations:

$$\begin{aligned} \rho l_{e1}\ddot{x}_1^j + \frac{1}{2}C_{L1}\rho\dot{x}_1^j\left|\dot{x}_1^j\right| &= p_{e1}^j - p_i^j \\ \rho l_{e2}\ddot{x}_2^j + \frac{1}{2}C_{L2}\rho\dot{x}_2^j\left|\dot{x}_2^j\right| &= p_{e2}^j - p_i^j \\ &\dots \\ \rho l_{em}\ddot{x}_m^j + \frac{1}{2}C_{Lm}\rho\dot{x}_m^j\left|\dot{x}_m^j\right| &= p_{em}^j - p_i^j \end{aligned} \quad \textbf{(5)}$$

where m is the number of openings, $\dot{x}_m^j$ is the j^{th} step of the time derivative of the position of the air slug at opening m, and $\ddot{x}_m^j$ is the second time derivative of the position of the air slug at opening m. After substituting the derivatives in for x, this system becomes m equations with $m + 1$ unknowns (x_1, $x_2 \dots x_m$, and p_i). To eliminate the internal pressure as an unknown, the continuity equation is incorporated:

$$p_i^j = \frac{P_0}{V_0}\sum_{k=1}^{m} A_k x_k^j \quad \textbf{(6)}$$

where x_k^j is the j^{th} step of the position of the air slug at opening k (Holmes, 1980) and A_k is the area of opening k. P_0 and V_0 are constant parameters already shown in Eq. (4).

Here, we use the SDE method to determine the effects of the variable open area on internal pressures. Then, we apply those results with the MDE method for realistic scenarios but with an effective open area for the garage door that captures the proper internal pressure effects during peaks gusts. This simplifies the solution of these non-linear differential equations significantly, while yielding an answer of acceptable accuracy.

The solution of the SDE and MDE require iterative processes. For the MDE, the method of Oh et al. (2007) is used. For the SDE with the variable open area of the garage door, the Oh et al. (2007) method must be modified. Following each iteration, where the internal pressure is solved using the external pressure and previous internal pressure values, the net pressure is calculated and used to determine an updated open area using a fit to the net pressure - open area curve, shown in Figure 2-5(c). The updated open area is then used in the calculation to determine the next value of the internal pressure. It should be noted that the open area for the garage door when it is closed under a no-load condition is not zero because of leakage between the door and the frame. A leakage value of 0.1% of the garage door area is used (ASHRAE, 2005).

Finally, realistic external pressure time series for the location of the door are required as input for the SDE and MDE methods. Data from the NIST aerodynamic database of Ho et al. (2005) is used for this purpose. This database was gathered from ABL wind tunnel tests on low-rise building models with various dimensions and sizes of openings. In particular, pressure taps were examined from the middle of a windward wall on a building with full-scale dimensions of 38.1 m x 24.4 m with an eaves height of 12.2m and a roof slope of 1:12. While this is somewhat larger than the dimensions of a typical house, windward wall pressures near the centre of the wall (i.e., near the stagnation point) are not likely to be too sensitive to the precise wall dimensions, keeping in mind that the objective is to obtain the ratio of the peak net pressure to peak external pressure for typical residential garage door sizes and volumes. Although external pressures from the WindEEE experiments could have been used, the NIST data is more established, and the small size of a garage door relative to a tornado makes using ABL winds a reasonable simplification.

2.3.3 Comparisons to Oh et al. (2007) and Oh (2004)

The internal pressure model used throughout this study is implemented using a MATLAB code that is based upon the work done by Oh et al. (2007). Therefore, the accuracy of the code is validated by examining and replicating results using the current model to those in Oh (2004), Ho et al. (2005), and Oh et al. (2007). All of these past studies examined pressure coefficients on the same 38.1 m by 24.4 m building model, using data from the NIST aerodynamic database.

Three different series of pressure coefficients were examined in Oh's previous work: the measured external pressure, Cp_e, the simulated internal pressure Cp_i (SDE), and the measured internal pressure Cp_i (exp). The measured external pressure was a weighted average of pressure taps located near the significant opening in the building model, the simulated internal pressure was found by solving the SDE using the internal pressure model, and the measured internal pressure was taken from the two internal pressure taps located in the building. The first set of results examined pertain to these three types of pressure coefficients with several building configurations at a wind angle normal to the opening (270°), and oblique to the opening (330°). The configurations examined are a 12.2 m eave height with a large rectangular opening, a 12.2 m eave height with a large circular opening, a 4.9 m eave height with a small circular opening, and a 12.2 m eave height with solely background leakage. For each configuration and type of pressure coefficient, the mean, maximum, minimum, and rms (standard deviation) of the coefficients are found.

Table 2-4 compares these results for the large rectangular opening between Oh (2004) and the current model. This configuration is chosen due to being the most similar to the setup of the current study. The results compare reasonably well, with the current model mostly yielding results within 10% error of Oh (2004). A consistent underestimation of mean pressure coefficients is present, especially in the 270° wind direction. It should be made clear that the current model is not expected to exactly replicate the results of past studies as there are several unknown factors. The main sources of error are the unknown combination and weights of pressure taps that were used to gather the measured pressure coefficients, and the unknown statistical method that was used to find the extreme values (max and min) in the time histories.

Another model validation performed is the comparison of sample sections of pressure time history available in several of the past studies. Printed versions of the sample time histories are scanned and plotted using PlotDigitizer, and these same sections of time history are replicated using the current model with the same NIST data. Figure 2-7 shows a sample simulated internal pressure time-history from the large rectangular opening case in Oh et al. (2007), shown in blue, and a replica using the current model on the same plot, shown in orange. Despite several sources of error, mentioned above, the results line up well, with only subtle inconsistencies. These comparisons, along with many others, provide confidence in the numerical method.

Table 2-4: Comparison of pressure coefficients in Oh (2004) to the current model.

		270 Degrees		330 Degrees	
		Oh (2004)	**Current Model**	**Oh (2004)**	**Current Model**
Cp_e	**Mean**	0.63	0.58	0.17	0.18
	rms	0.27	0.27	0.12	0.13
	Max	1.89	1.81	0.90	0.85
	Min	0.06	-0.07	-0.16	-0.18
$Cp_i\ (SDE)$	**Mean**	0.63	0.58	0.17	0.18
	rms	0.31	0.29	0.15	0.15
	Max	2.20	1.95	1.16	0.97
	Min	-0.11	-0.14	-0.28	-0.26
$Cp_i\ (exp)$	**Mean**	0.68	0.61	0.21	0.19
	rms	0.33	0.31	0.13	0.13
	Max	2.18	2.06	0.98	0.87
	Min	-0.02	-0.13	-0.15	-0.20

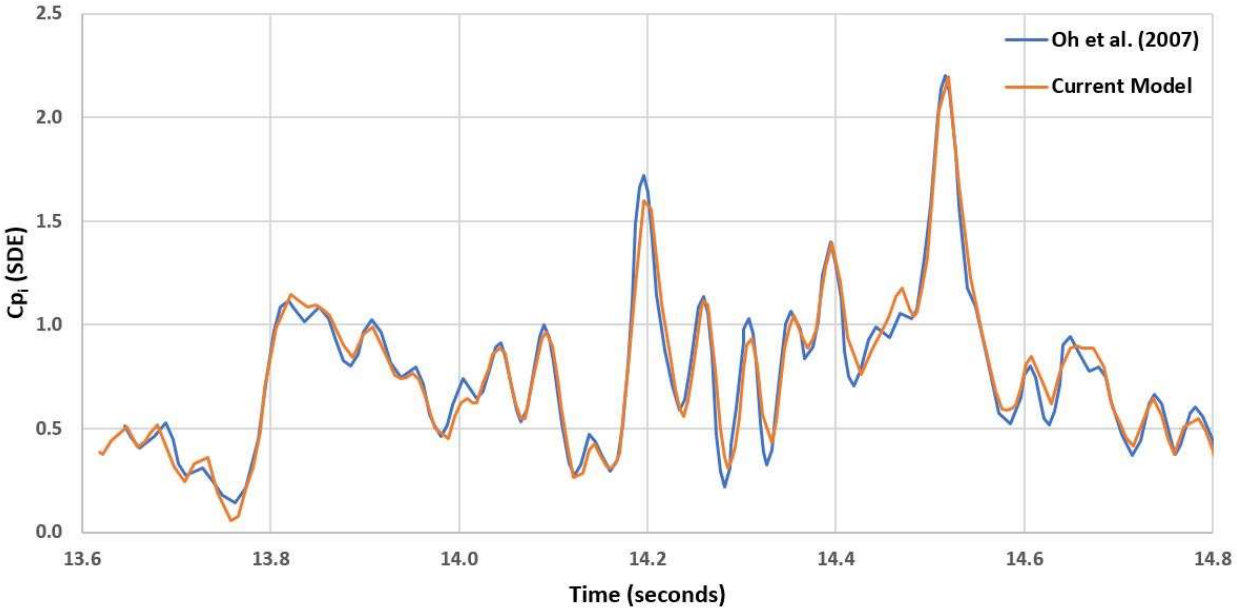

Figure 2-7: A section of sample simulated internal pressure time history from Oh et al. (2007) compared to the current model.

3. Internal Pressures for a Building in a Tornado

3.1 Experimental and Model Results

3.1.1 Wind Flow Field

To better examine the experimental pressure data from the WindEEE Dome shown in Figure 2-6 of Section 2.3.1, several adjustments are made to the raw pressure-time histories to allow for more convenient and meaningful analysis of the data. Due to the focus of this study being effects of the tornado vortex on the building, it is more informative to plot the pressures versus the normalized location of the vortex (y/r), and the wind direction at the opening (θ_o), instead of plotting the pressures versus time. Although the vortex translation is 4000 mm, or -5 ≤ y/r ≤ 5, the tracking of the bellmouth location was started manually each trial sometime shortly after the beginning of translation. Because the actual start and end locations of the vortex vary between trials, and the changes in pressures are small when the vortex is far away from the model, this study examines the effects of the vortex on the building over the range -4 ≤ y/r ≤ 4. Further steps of processing the pressures include removing the static pressure, transforming the remaining dynamic pressure to pressure coefficients, and taking the ensemble averages of the coefficients with respect to vortex location and wind direction. Before these steps can be explained, an understanding of the flow patterns and directions is needed.

Based on the definition of θ in Chapter 2, the wind direction is approximately 90° ≤ θ ≤ 180° as the vortex approaches the building, θ ≈ 90° as the vortex translates past the building, and 0° ≤ θ ≤ 90° after the vortex translates past the building. The θ_o values are approximated using the wind directions at probes C and D, seeing as the opening is located closest to those two probes, halfway between them. First, moving averages using 100 data points of wind direction are taken from probes C and D, individually, for each trial. The reason for this averaging is to only capture meaningful data from the probes by removing the small anomalous groups of data from when the probes are not facing windward. The wind direction is taken from probe D for y/r ≤ -2, from probe C for 2 ≤ y/r, and as an average between the two probes for -2 ≤ y/r ≤ 2, based on the general orientation of each probe in the test setup. Additionally, the moving average is reduced to 10 points when the vortex is within one radius of the building's y-axis location (-1 ≤ y/r ≤ 1).

This reduction is to counter the turbulent nature of the wind directions when the vortex is near the building. This turbulence results in large fluctuations in the wind direction that easily fall out of the 80 degree range of the probes and, therefore, do not produce 100 consecutive measurements of wind direction for the moving average. After this process is performed for all 88 trials, the average wind direction is ensemble averaged over lengths of y = 80 mm, or y/r = 0.2, the results of which are shown in Figure 3-1. This length of translation is chosen to be short enough to accurately show the changes in the wind direction, but long enough to ensure a smooth relationship.

Figure 3-1 shows the wind direction at the opening, θ_o, beginning around 190°, decreasing to 90° just before the vortex translates past the building, and decreasing to about 40° as the vortex moves away from the building. There is asymmetry about y/r = 0, with the wind direction decreasing more rapidly with respect to the vortex location when the vortex is approaching the building, compared to after the vortex translates past the building. It is worth noting that although the vortex edge is directly over the centre of the building at y/r = 0, the wind direction is measured at the location of probes C and D, not the centre of the building, located at y/r = -0.36.

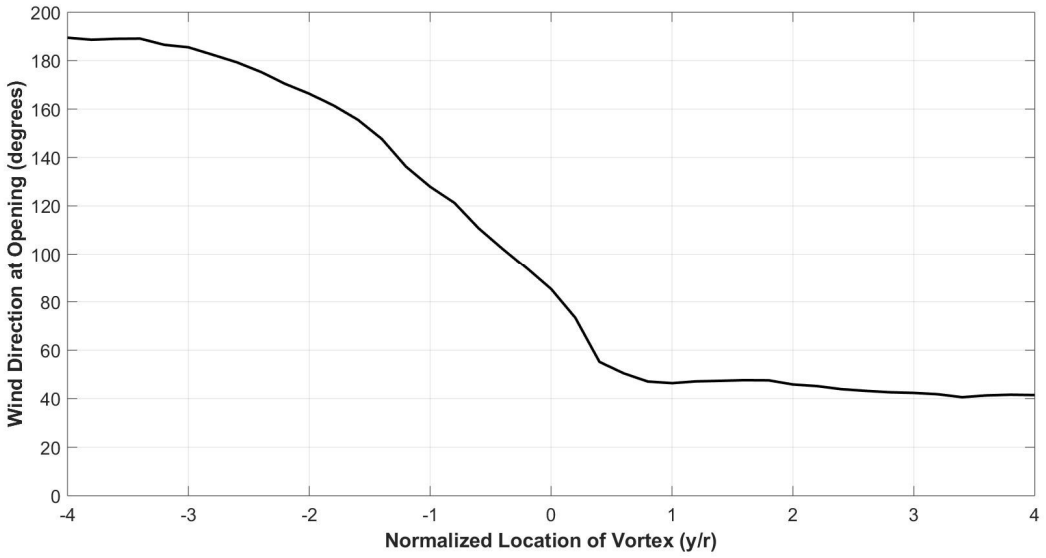

Figure 3-1: Ensemble-averaged wind direction at the opening (θ_o) across all trials vs. normalized vortex location (y/r).

To aid in understanding the wind directions from Figure 3-1, Figure 3-2 illustrates the various components of the wind direction at three vortex locations. To better visualize the wind field and wind vectors near the building, the three building locations are shown relative to the vortex location, even though the vortex is translating and the building location is stationary. Each building location shows the overall horizontal wind velocity (ignoring the vertical component), V, as well as its vector components which are the tangential wind velocity, V_θ, the radial wind velocity, V_r, and the translational wind velocity, V_t. These wind component vectors are drawn roughly to scale with each other, with the exception of V_t which is approximately 100 times smaller than the other components and, therefore, can be reasonably excluded in analysis.

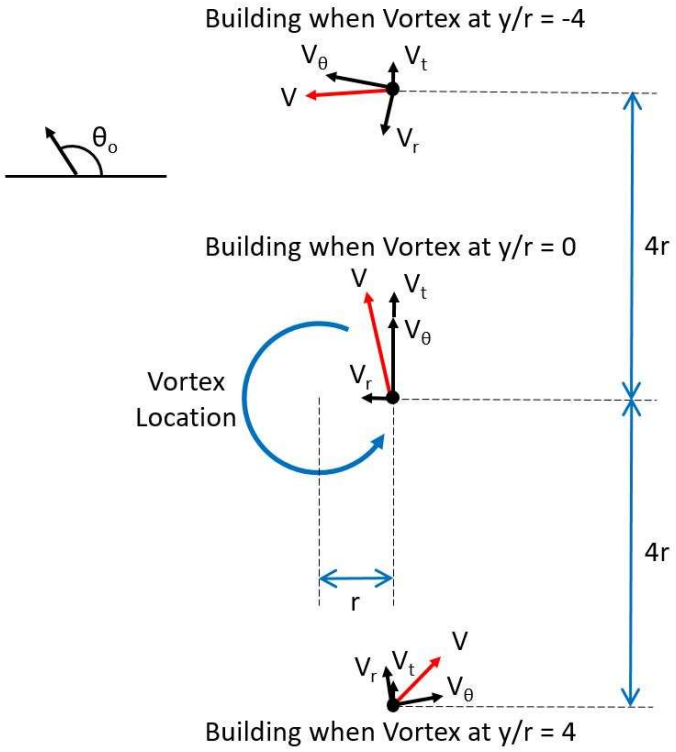

Figure 3-2: Total horizontal wind direction (V) broken down into tangential (V_θ), radial (V_r), and translational (V_t) vector components at various building locations relative to the translating vortex.

Although the wind direction as a function of y/r governed solely by a constant tangential component would start just below 180° and decrease to a value just above 0°, the radial component of the wind that points towards the centre of the vortex also plays a large role in the wind direction at the opening. Additionally, the tangential wind speed of the vortex is stronger

closer to the vortex centre. This means that as the vortex approaches the building, the tangential wind speed is increasing and the wind direction changes faster, however, after the vortex has passed, the tangential wind speed is decreasing and the wind direction changes slower. This explains the asymmetric nature about $y/r = 0$ in Figure 3-1, where the wind direction changes more from $-4 \leq y/r \leq 0$, than it does from $0 \leq y/r \leq 4$. Also, keep in mind that Figure 3-2 shows the wind direction at $y/r = 0$ to be just above 90°, however, probes C and D are located at $y/r = -0.36$, as mentioned earlier. Therefore, it makes sense that the wind direction in Figure 3-1 is just above 90° at $y/r = -0.36$.

Another contributing reason to why the wind direction in Figure 3-1 drops off quickly but then flattens out after passing $y/r = 0.5$ is the transition between the wind direction being captured by probes C and D to being captured by only probe C. In an ideal experiment, all wind speed and direction measurements would be taken at one location, preferably at the opening. However, probe C is located 377 mm from probe D, and 188 mm, or $0.47r$, away from the opening in the negative x-direction (refer back to Figure 2-2). After the vortex translates past the building, the tangential wind speed at probe C is closer to 0° than it is at probe D. The difference between the wind direction at probes C and D is less notable when the vortex moves further away, but contributes to the somewhat surprising immediate flattening of the wind direction around $y/r = 0.5$.

One important feature of the wind flow not depicted in Figure 3-2 is that the tornado produced by the WindEEE experiment is comprised of several sub-vortices swirling within the main vortex, shown in Figure 3-3. These sub-vortices cause highly turbulent flow with large changes in wind speed and direction within and around the radius of the main vortex. Because these events are small in scale relative to the building, they can alter measurements at individual Cobra probes and external pressure taps surrounding the opening. Additionally, the vortex core adds a more significant vertical component to the wind, further increasing the turbulence in this region. Contrarily, the areas father away from the vortex have less streamline curvature and turbulence, resulting in a more uniform environment. Since the vortex is translating along the y-axis and the building is located offset to the right at $x/r = 1$ and $y/r = 0$, the most turbulent flow occurs when the vortex is near $y/r = 0$.

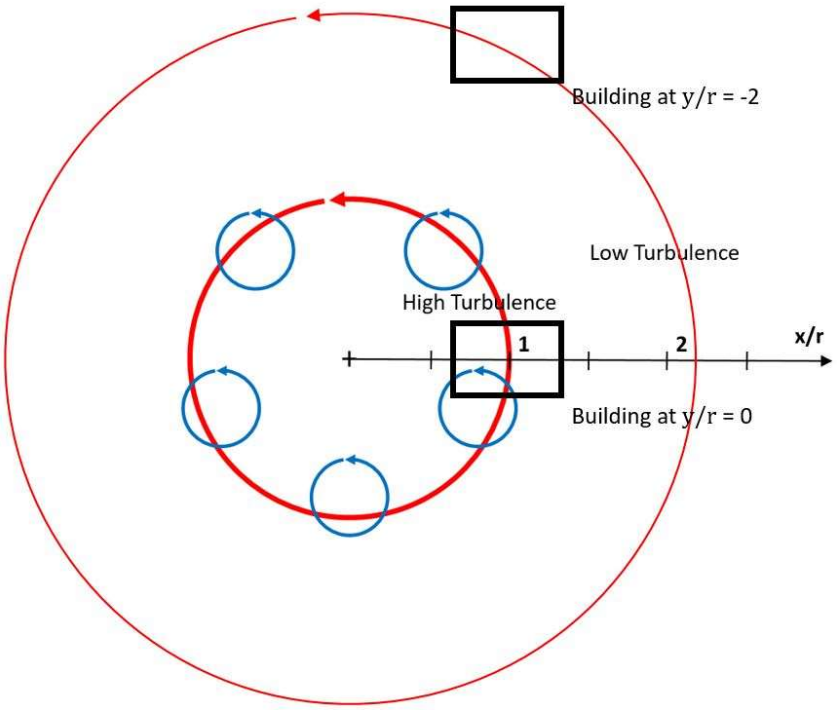

Figure 3-3: A sketch of the wind streamlines from the main vortex (thick red line) and sub-vortices (blue lines) in the WindEEE experiment showing high and low turbulence regions and two building locations relative to the location of the main vortex.

3.1.2 Ensemble Pressure Results

As mentioned at the beginning of the chapter, several adjustments are made to the pressure data plotted in Figure 2-6. In addition to plotting the pressures with vortex location and wind direction instead of time, these adjustments include: removing the static pressure, transforming the pressures to pressure coefficients, and taking the ensemble averages of the coefficients.

In ABLs and regular wind tunnel tests, the static pressure is approximately spatially uniform; however, in a tornadic wind field, the static pressure varies spatially with parameters such as the core radius and swirl ratio (e.g., Baker and Sterling, 2019). Therefore, the static pressure from the WindEEE results is removed from the overall pressure, leaving only the aerodynamic pressure. This is simply represented as: $p_a = p - p_s$, where p is the overall pressure, p_s is the static pressure, and p_a is the aerodynamic pressure. The static pressure is calculated using a function of the pressure tap locations relative to the location of the vortex core on the ground, developed in Kopp and Wu (2020).

The reason for this removal of the static pressure is to focus on the aerodynamic effects of the tornado on the building. In the case of this study, only the static pressures surrounding the single dominant opening need to be removed. In a case with multiple openings, this process would be more complicated as the spatial static pressures for multiple openings would need to be computed. The removal of the static pressure changes extreme pressures surrounding the opening and inside the building as the vortex radius passes over the structure from negative to positive values, as the negative drop from the static pressure of the tornado is larger in magnitude than the positive aerodynamic pressures on the building. All pressures discussed in this chapter are aerodynamic pressures, unless otherwise stated.

The pressures from the experiment are then turned to coefficients using the average wind velocity magnitude from the four Cobra probes as a function of vortex location. Figure 3-4 depicts the ensemble-averaged wind velocity of each probe as well as a moving average of the velocities between all the probes versus the vortex location. The velocities from probe A are shown in black, probe B in blue, probe C in green, probe D in red, and the moving average in purple. The figure confirms that, approximately speaking, probes A and D measured wind speeds as the vortex approached the model and probes B and C measured wind speeds after the vortex translated past the model. These ensemble-averaged velocities were obtained in Kopp and Wu (2020), but the process is described here since it is important to this study.

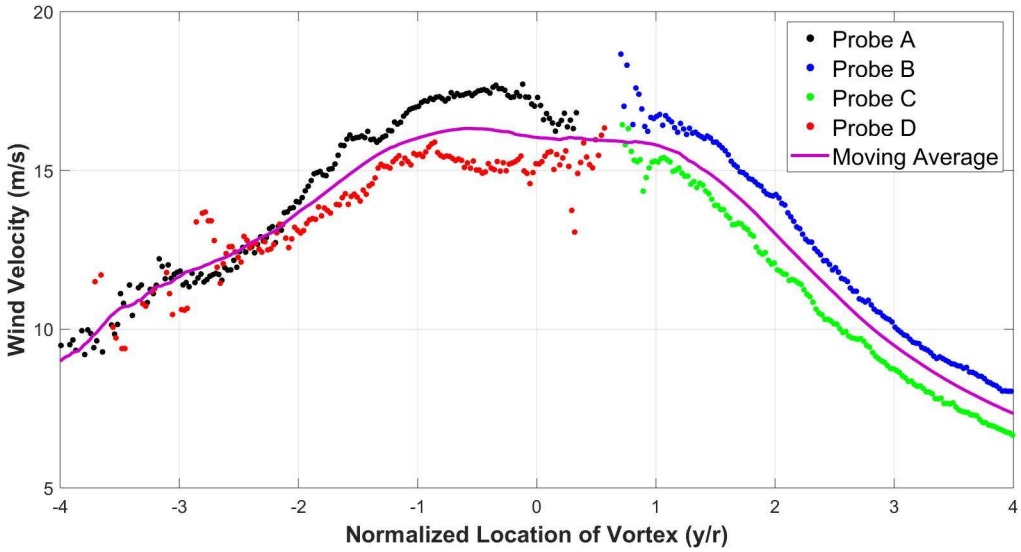

Figure 3-4: Ensemble-averaged wind velocity magnitude at each Cobra probe and a moving average of the results vs. normalized vortex location (after Kopp and Wu, 2020).

The velocities of each probe are taken using the conditional average of the velocity time-histories based on the location of the vortex. The bin size (i.e., segment length) is chosen as 5 mm of vortex translation, as a reasonable compromise between having a sufficient number of data points along the tornado translation and having sufficient data in each segment. Each probe velocity data point in Figure 3-4 represents the average probe velocity in the given segment of vortex location across all 88 trials. Any trial that did not produce 5 mm of data (or about 0.1 seconds based on the vortex translation speed) due to missing measurements is excluded. These missing measurements are the result of Cobra probe limitations, being that they could not record data for wind velocity magnitudes less than 2 m/s or wind directions more than 40° from their windward facing direction (including winds with a strong vertical component). Lastly, a moving average using the 100 nearest velocity data points from any probe at every vortex location is taken. This ensures one smooth relationship between velocity and vortex location. Keep in mind that many reasonable assumptions could have been made to obtain this velocity relationship, and the purpose is simply to change the pressures into pressure coefficients. The pressure coefficients are then simply calculated as follows:

$$Cp(Y) = \frac{p_a(Y)}{\frac{1}{2}\rho V_{ma}^2(Y)} \tag{7}$$

where $Cp(Y)$ is the pressure coefficient, $p_a(Y)$ is the aerodynamic pressure, and $V_{ma}(Y)$ is the moving average wind velocity magnitude, all at vortex location Y.

Finally, the individual pressure coefficients are ensemble-averaged in order to plot the mean pressure coefficients as a function of y/r, similar to what was done with the wind velocities. The conditional average of the pressure coefficients, obtained using the pressures and associated average wind velocity at the given vortex location (Eq. 7), are gathered using 10 mm of vortex translation segments. The pressure coefficients within each of these segments are averaged over all 88 trials. This ensemble-averaging process is represented by the following equation:

$$\overline{Cp}_{\mathrm{y}} = \frac{1}{n_{\mathrm{y}}} \sum_{i=1}^{n_t} \sum_{Y \in S_y} Cp(i, Y) \tag{8}$$

where $\overline{Cp}_y$ is the ensemble-mean external or internal pressure coefficient at general tornado location y, n_t is the number of experimental trials, $Cp(i, Y)$ is a specific pressure coefficient in trial i and specific tornado location Y, and S_y is the set of tornado locations contained within a 10 mm interval of y (y - 5 mm $\leq Y \leq y$ + 5 mm) for each trial, and n_y is the number of data points contained in set S_y across all trials.

From each set of pressure coefficients, S_y, a maximum and minimum pressure is also determined. Due to the differing number of data points contained within each set, as a result of the nature of the WindEEE testing, standard methods of computing the extreme pressures statistically, such as the Lieblein (1974) BLUE (Best Linear Unbiased Estimator) method, are difficult. Therefore, the maximum and minimum pressure coefficients are taken as the 95th and 5th percentiles, respectively, from each tornado location set of coefficients. The advantage of this method is that it is not influenced by the number of data points contained in each value of y, or the details of the testing (length scales, sampling rates, etc.), the goal being to simply have some idea of the extreme values from the experiment. Distributions of these values are examined later in this chapter.

Using the above methods, ensemble-averaged pressure time-histories as a function of y/r are obtained for all 88 trials with Cobra probe orientations I, II, and III. Figure 3-5(a) depicts the ensemble mean, maximum, and minimum of the external, simulated internal, and measured internal pressure coefficients across all relevant trials versus the normalized vortex location. Once again, the external pressures (green) are taken as an average of the four taps surrounding the opening, the simulated internal pressures (blue) are produced using the SDE, and the measured internal pressures (red) are an average of the two pressure taps inside the building, which have similar values, as mentioned earlier. The darker, vibrant plots in Figure 3-5 represent the mean pressures and the lighter, faded plots represent the maximum (above the mean data) and minimum (below the mean data) pressures, obtained as detailed above. Note that the external pressure coefficients are not visible in the plots due to their similarity to the simulated internal pressures.

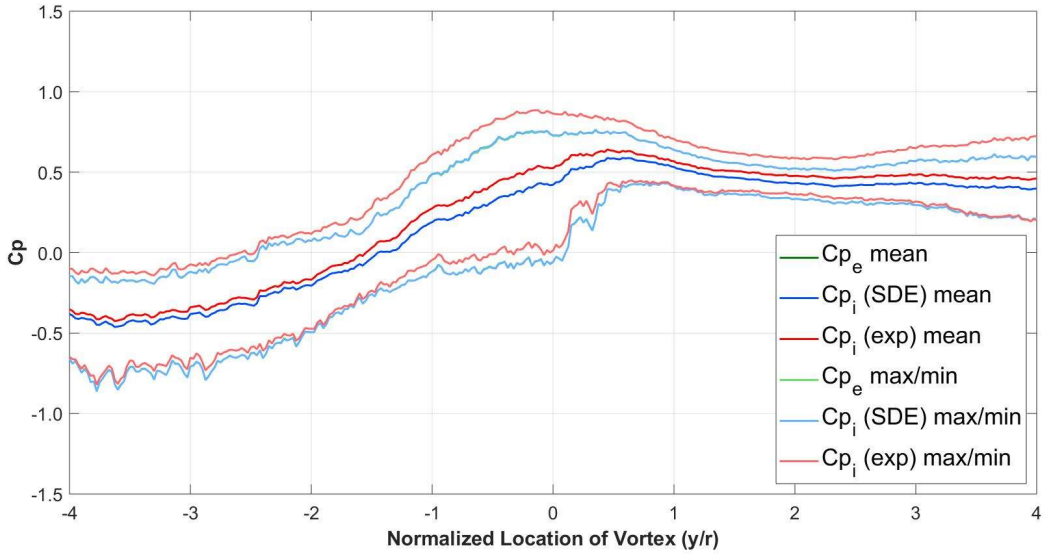

(a)

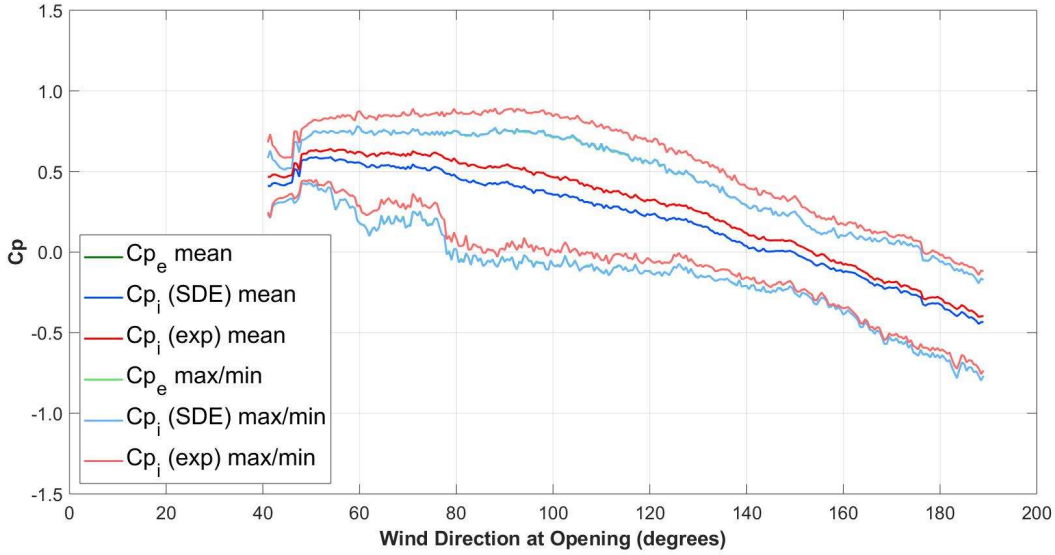

(b)

Figure 3-5: Ensemble-averaged mean, maximum, and minimum of external and internal aerodynamic pressure coefficients from all configurations. External pressure at the opening, simulated internal pressure from the SDE, and measured internal pressure inside the building plotted vs. (a) normalized vortex location (y/r) and (b) wind direction at the opening (θ_o).

From Figure 3-5(a), the pressure coefficients are negative when the vortex is far away from the building, increase to a positive peak around $y/r = 0$, and then decrease slowly until after $y/r = 2$ but remain positive as the vortex moves away from the building model again. These pressure changes are due to the changing wind direction as the vortex translates past the building, which

will be examined further in Figure 3-5(b). The peak maximum pressures in Figure 3-5(a) occur just before the vortex radius reaches the centre of the building (i.e., when it is approximately over the opening), and the peak mean and minimum pressures occur shortly after the vortex has translated past the centre of the building. There appears to be more variation in the pressures (i.e., the maximum and minimum pressures are farther from the mean) as the vortex approaches the building, compared to after it translates past the building, although this variation begins to increase again after y/r = 2. The larger pressure variations prior to the vortex reaching the building are likely due to the more rapidly changing wind direction during this section of the vortex translation, as noted earlier. The ensemble pressure averages also appear less noisy (i.e., smoother Cp lines) after the vortex translates past the building, which could also be seen in Figure 2-6.

The most important takeaway from Figure 3-5(a) is that SDE internal pressure model simulates the measured internal pressures fairly accurately throughout the entire translation of the vortex. The model only has a slight offset making it consistently smaller than the measured pressures, with slightly higher error around the peak pressure coefficients at -1.5 ≤ y/r ≤ 0.5 when the vortex radius is approaching and directly over or near wall CD of the building with the dominant opening. In general, the model is the most accurate when simulating minimum pressures and the least accurate when simulating the maximum pressures, although the maximum pressures are still well predicted.

To better understand the wind effects on the building and its internal pressures, ensemble pressure coefficients are also plotted against the wind direction at the opening in Figure 3-5(b). This process is similar to that of computing the ensemble-averages based on tornado location. Here, the bin size is selected as 0.5°, to ensure a similar number of data points to when the bins were separated by vortex location in Figure 3-5(a). The equation for the ensemble pressure coefficients, which is similar to Eq. (8), is as follows:

$$\overline{Cp}_{\theta} = \frac{1}{n_{\theta}} \sum_{i=1}^{n_t} \sum_{\Theta \in S_{\theta}} Cp(i, \Theta) \qquad \textbf{(9)}$$

where $\overline{Cp_\theta}$ is the mean external or internal pressure coefficient at general wind direction θ, $Cp(i, \Theta)$ is a specific pressure coefficient in trial i and specific wind direction Θ, S_θ is the set of wind directions contained within a 0.5° interval of θ (θ - 0.25° ≤ Φ ≤ θ + 0.25°), and n_θ is the number of data points contained in set S_θ across all trials. Using the same method as with sets Cp_y, maximum and minimum pressures are determined from sets S_θ using the 95th and 5th percentiles, respectively.

In Figure 3-5(b), the largest maximum pressure coefficients occur at wind directions between 50° and 100°, with the peak measured internal pressure at 88°, expectedly near 90°, although many other peaks in the larger range come close to this absolute peak. Interestingly, the largest mean pressures occur between 50° and 75°, with the peak measured internal pressure at 54°, and the largest (most positive) minimum pressures occurring between 48° and 54°. This is partially explained by the higher variation in pressures around and after 90°, which was also noted in Figure 3-5(a). As a result of this wind direction shift in peak pressures, the coefficients at wind directions near 45° are higher than those at 135°, even though they would be expected to be similar. Figure 3-5(b) does explain why Figure 3-5(a) has positive pressure coefficients for the duration of the vortex translation after it translates past the building, but is negative until a certain distance before it reaches the building. Evidently, the pressure coefficients never drop back into the negatives because the wind direction never adequately approaches 0°, reaching only about 40°.

There are a couple notable results that can be explained by the complexity of the experiment and the potential sources of error encountered throughout the experiment and analysis. These results are the peak minimum, mean, and to a lesser extent, maximum, pressure coefficients not being at 90° (and as a result, the pressures at wind directions below 90° being higher than the pressures at wind directions above 90°), and the difference between the simulated and measured internal pressures. Both of these findings will be discussed below.

Several factors likely contribute to peak mean pressures not occurring at a wind direction at the opening of 90°. Namely, the multiple vortices of the simulated tornado, the tornado translation, and the measurement limitations of the Cobra probes. As depicted earlier in Figure 3-3, the main vortex in the WindEEE experiment contains multiple sub-vortices that made the region in and

around the radius of maximum winds especially turbulent. Therefore, large, local fluctuations occur in the wind speeds and directions when the vortex is near $y/r = 0$, including a larger vertical component in the wind velocity. Theoretically, this is the point where $\theta_o \approx 90°$; however, these sub-vortices cause large fluctuations in the wind direction, and, therefore, the pressure coefficients.

The translation of the tornado is another reason for the peak pressure coefficients not occurring at $\theta_o = 90°$. Many past studies have examined the differences between translating and stationary tornadoes (e.g., Haan (2017)). Feng and Chen (2018) showed that a translating tornado can cause delays in the peak responses of a building, partially due to the portion of the vortex near the ground lagging behind the upper portion of the vortex where its location is measured from. This could partially explain the peak mean pressures in this study occurring shortly after $y/r = 0$. A translating vortex also has an effect on the static pressure model. The static pressure that is removed from the pressure time-histories is considered symmetrical about $y/r = 0$, but this is only an approximation that is not completely accurate for a translating tornado according to Kopp and Wu (2020). Inaccuracies in the static pressure model would be reflected in the aerodynamic pressures in Figure 3-5, which could change the location of the peak pressures.

The third factor that likely contributes to the peak pressures not being at 90° is the limited wind direction range of the Cobra probes. As discussed in the methodology, each probe only has an 80° acceptance range with probes A and D roughly meant to capture winds as the vortex approaches the building, and probes B and C to capture winds after the vortex translates past the building. Probes B and C are set to 50° in every configuration, and therefore could only measure winds between 10° and 90°. Probes A and D are set to 150°, 130°, and 110° for Cobra probe orientations I, II, and III, respectively. Therefore, 90° winds are at the limit of the range for probes B and C, and are only captured more accurately by probes A and D in one of three probe orientations. This likely creates measurement biases of θ_o away from 90°.

The second important item to discuss in this section is the small difference in the measured and simulated internal pressures in the results. One likely explanation of this difference is the multiple vortices discussed earlier. As mentioned, the turbulence is not spatially uniform in the tornado-like flow, and the turbulence is especially strong near the vortex core where the sub-

vortices and higher vertical components in the wind are present. This is different from straight-line ABL wind tunnel experiments which have spatially uniform turbulence, which the internal pressure model was originally designed for.

Another reason for the small difference in the measured and simulated internal pressures is the difference between the various external pressure taps surrounding the opening, and wind interference at the opening from the Cobra probes, probe mounts, and the building model. When comparing the external and simulated internal pressures using each of the four external taps surrounding the opening individually, some differences are found. This investigation is discussed more thoroughly in Appendix A, but overall, the top two taps appear to produce more accurate estimations of the measured internal pressure than using the bottom two taps. This may be related to wind interference from the Cobra probes or their mounts. Due to the greatly varying wind directions of any given trial in a translating tornadic wind tunnel test, avoiding interference from measurement instruments is more difficult than in an ABL wind tunnel test. The following section will go more into depth on the differences of ABL and tornadic pressures.

3.2 Comparison to Internal Pressures in ABL Winds

3.2.1 Pressure Results by Wind Direction

To provide a reference for the accuracy of the internal pressure model used in this study for the tornadic winds, this section presents a comparison to similar results obtained from the NIST aerodynamic database. The NIST database contains external and internal pressure measurements that were made on a series of low-rise building models in an ABL wind tunnel. The same internal pressure model used in this study was previously used on this data to compare simulated and measured internal pressures by Oh et al. (2007). For the purposes of this section, the experiments and data from NIST will be referred to as the "ABL cases" and the experiments and data from WindEEE will be referred to as either the current study or the "tornadic cases".

Figure 3-6(a) shows the ensemble means of external and internal pressure coefficients versus wind direction for the tornadic case, similar to Figure 3-5(b), except that the coefficients are averaged over 5° wind direction increments instead of 0.5° increments and plotted from 40° to 180°. Averaging the coefficients over these intervals makes the data more easily comparable to

the NIST database, as ABL testing is performed one wind direction at a time. Additionally, this type of comparison is reasonable because even in ABL flows, the wind direction fluctuates from the mean significantly (Wu and Kopp, 2016). Only data for wind directions captured in both the tornadic and ABL cases are examined. Figure 3-6 also includes the mean coefficients ± the respective rms values. It should be noted that the turbulence intensity in the current study is between approximately 0.1 and 0.15 depending on vortex location at the roof height of the building (Kopp and Wu, 2020). This is lower than the turbulence intensity for open exposure used in the ABL studies of 0.20 at roof height (Ho et al., 2005). The rms is shown in Figure 3-6 instead of the extreme pressures because the statistical peak pressures are not gathered the same way in this study as in the ABL experiments, making a comparison of the mean and rms statistics more meaningful. The pressure distributions in the tornadic and ABL cases are compared later in this section. In Figure 3-6, the mean values are displayed as solid lines and the rms offsets are displayed as dashed lines. Once again, the measured external pressure is similar to the simulated internal pressure, making them appear as a single line in the plots.

Table 3-1 shows similar information as Figure 3-6 but in tabular form. Presented in the table are the mean and rms external, simulated internal, and measured internal pressure coefficients at various wind directions for the current study and the two ABL cases. The chosen wind directions are spaced equally at 45°, from 45° to 180°.

The mean measured internal pressure coefficients for the tornado in Figure 3-6(a) are highest for wind directions at the opening of 55° to 75°, reaching coefficients of up to 0.63 for 55°. The coefficients drop off quickly as the wind direction decreases towards 40° (and wind directions below 40° are not captured) and drop off more slowly as the wind direction increases towards 180°, to a minimum Cp_i of -0.30. The mean + rms coefficients are highest at between 60° and 90°, which makes sense as it was shown earlier that the maximum pressures occur in this range. As noted previously, the mean SDE simulated internal pressure is consistently slightly below the experimental pressure, with closer agreement at the more oblique wind angles and the largest underestimations around 90°. The average absolute difference in simulated and measured Cpi between all wind directions is 0.07, with a relatively small range of values between 0.04 and 0.11. These differences are partly within uncertainty, which is defined as ±0.07 for experiments in identical conditions with a 95% confidence level, as stated in Quiroga Diaz (2006). This

means that there is some difference between the simulated and measured internal pressure coefficients that is not accounted for by measurement uncertainty.

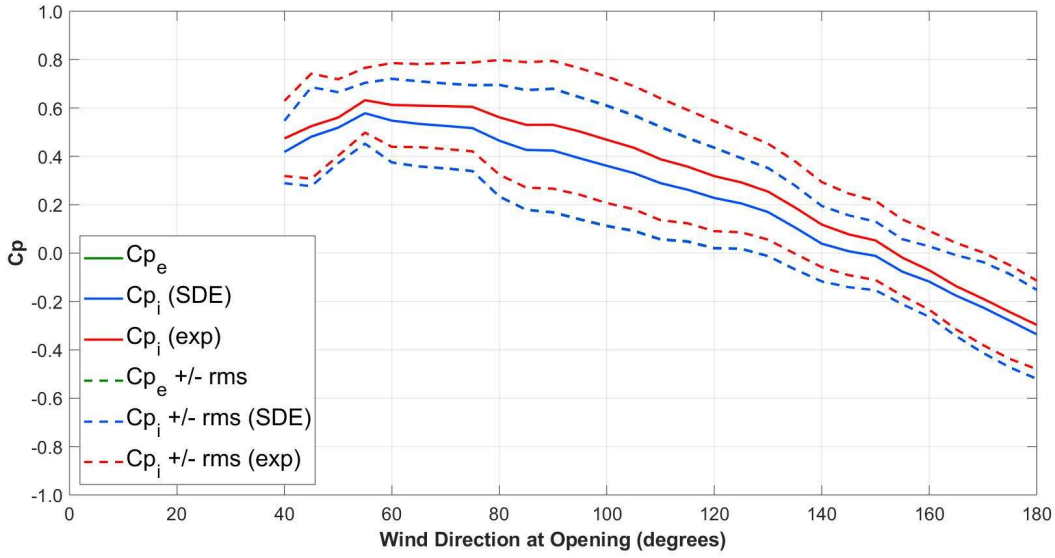

(a)

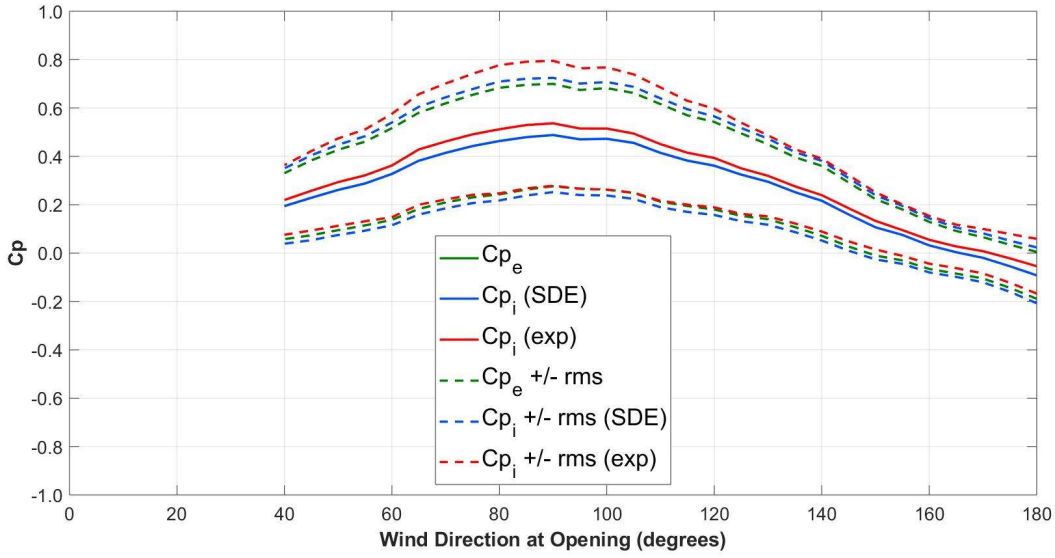

(b)

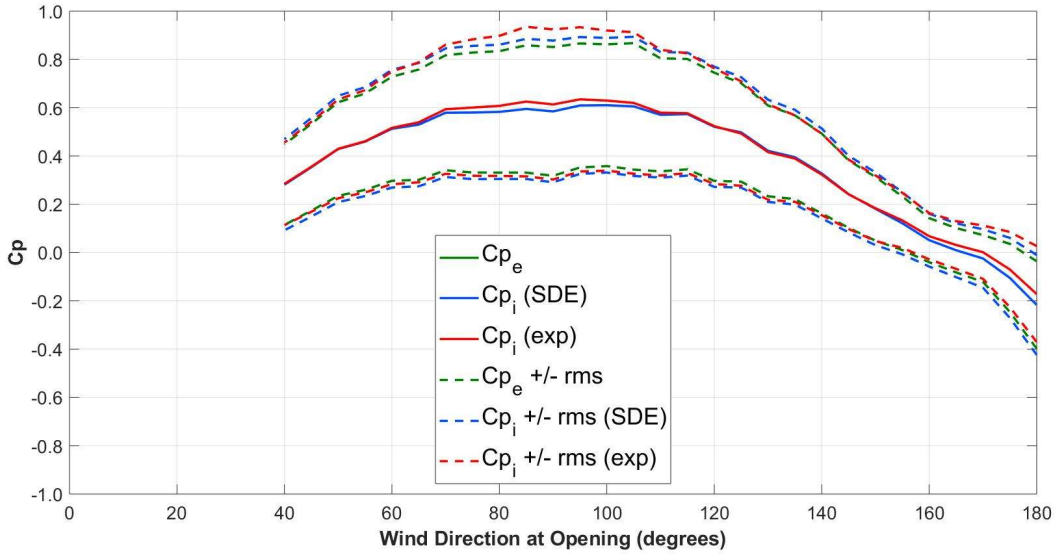

(c)

Figure 3-6: Ensemble-averaged mean ± rms external and internal dynamic pressure coefficients over five degree increments of wind direction for (a) the current study, (b) the ABL-Short case with building dimensions of 38.1 x 24.4, a height of 4.9 cm, and an open ratio of 3.3% with background leakage, and (c) the ABL-Tall case with the same details as ABL-Short except for an increased height of 12.2 cm.

Data from the ABL cases, two similar configurations to the current study from the NIST database, are also displayed in Figure 3-6. These tests were performed in the Boundary Layer Wind Tunnel Laboratory at UWO. The low-rise buildings from the NIST configurations of interest were tested at a scale of 1:100 in open terrain with model plan dimensions of 38.1 x 24.4 cm. The only difference between the two configurations is that the first configuration had an eaves height of 4.9 cm, and the second configuration had a larger eaves height of 12.2 cm. These two configurations will be referred to as ABL-Tall and ABL-Short, respectively, for simplicity in this study. Both building models had a roof slope of 1:12 with a “large opening” on the long-wall on the windward side of the building. The opening ratio for both buildings was 3.3% with additional background leakage of 0.1%. Full details of these experiments can be found in Ho et al. (2003).

Table 3-1: Mean and rms internal and external pressure coefficients at various wind directions for the current study and the ABL experiments.

Statistic		Mean				rms			
Wind Direction		45°	90°	135°	180°	45°	90°	135°	180°
Current Study (tornadic)	Cp_e	0.46	0.40	0.10	-0.34	0.20	0.24	0.19	0.19
	Cp_i (SDE)	0.46	0.40	0.10	-0.34	0.21	0.24	0.19	0.19
	Cp_i (exp)	0.51	0.50	0.18	-0.30	0.22	0.25	0.21	0.20
ABL-Short	Cp_e	0.23	0.49	0.25	-0.09	0.15	0.21	0.14	0.10
	Cp_i (SDE)	0.23	0.49	0.25	-0.09	0.18	0.24	0.17	0.12
	Cp_i (exp)	0.26	0.54	0.28	-0.05	0.16	0.26	0.15	0.11
ABL-Tall	Cp_e	0.35	0.58	0.39	-0.22	0.18	0.27	0.17	0.18
	Cp_i (SDE)	0.35	0.58	0.40	-0.22	0.20	0.29	0.20	0.21
	Cp_i (exp)	0.36	0.61	0.39	-0.17	0.19	0.31	0.18	0.20

Figure 3-6(b) and 3-6(c) show the same data as Figure 3-6(a) but for cases ABL-Short and ABL-Tall, respectively. The ABL-Short case has experimental Cp_i values ranging from as low as -0.05 at the oblique wind directions to 0.54 at the expected normal wind direction of 90°. The ABL-Tall case has a slightly larger range from -0.17 at oblique wind directions to 0.63 at a wind direction of 95°. As expected, all data is relatively symmetric about 90°. These ranges of Cp_i values are comparable to this study, being somewhat within the uncertainty, discussed below, although do not reach lows as extreme at the oblique wind angles.

The internal pressure model simulates the measured internal pressures very well in the ABL cases, with slightly more accuracy than the current study, but a similar consistent offset of the simulated pressure to the measured pressure, especially in the ABL-Short case. The absolute difference in simulated to experimental internal pressure coefficient in ABL-Short ranges from

0.02 to 0.05, with a mean across wind directions of 0.03, and in ABL-Tall ranges from 0.00 to 0.05, with a mean of 0.01. Both of these ranges are completely within the uncertainty of ±0.07 for experiments in identical conditions that was mentioned earlier. This means that the simulated internal pressures are matching the measured internal pressures, within measurement uncertainty. Once again, the Cp_i difference in the tornadic case results ranges from 0.04 to 0.11, with a mean of 0.07. Therefore, the internal pressure simulations are more accurate in the ABL testing than the tornadic testing.

To achieve a better visualization of the similarities and differences in the current study from the ABL cases, Figure 3-7 compares just the ensemble mean and rms measured and simulated internal pressure coefficients versus wind direction from the tornado and ABL results. In this figure, the experimental mean pressures are plotted in red, the SDE mean pressures are plotted in blue, the experimental rms pressures are plotted in purple, and the SDE rms pressures are plotted in yellow. Additionally, tornadic results are plotted using circular data points, ABL-Short results are plotted using square data points, and ABL-Tall results are plotted using triangular data points.

Figure 3-7 shows that the pressure coefficients from the tornadic experiment in the current study have reasonable agreement with the ABL experiments, with some differences. The biggest discrepancy between the internal pressures is the aforementioned early peaks in the current study that occur around 60°, whereas the ABL pressure peaks occur around 90°. As a result, the internal pressure coefficients at wind directions near and before 60° are all higher in the current study. From 90° onwards, the pressures from the current study are lower than in the ABL studies, having coefficients roughly 0.1 lower than configuration ABL-Short and 0.2 lower than configuration ABL-Tall. As the wind direction approaches 180°, the pressures from the ABL-Tall case begin to converge on the values of the current study, and become closer than the ABL-Short case. When determining whether the differences between the tornadic and ABL cases can be attributed to uncertainty, a value of ±0.13 is used to compare coefficients from different laboratories under nominally identical conditions with a 95% confidence level (Quiroga Diaz, 2006). Using this value, the differences between the measured internal pressure coefficients from the tornadic and ABL-Short cases are within uncertainty between wind directions of 75° and 160°, and the differences between the same coefficients from the tornadic and ABL-Tall cases

are within uncertainty between 60° and 95°, with the majority of the results at other wind directions falling outside of the uncertainty range. Therefore, the differences in the tornadic and ABL wind pressures can not be completely accounted for by uncertainty, and there is therefore some difference between them.

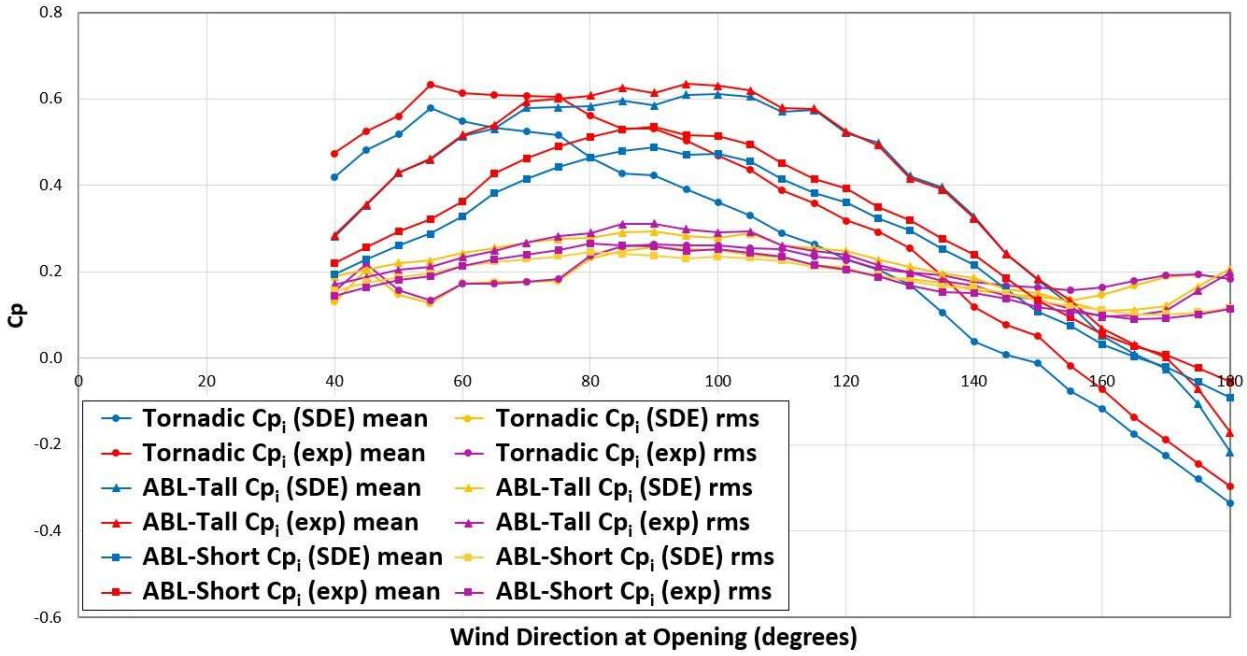

Figure 3-7: Combined graph of ensemble-averaged mean and rms simulated and measured internal pressure coefficients vs. wind direction in five degree increments for the current tornadic study and for the ABL-Short and ABL-Tall cases.

The measured rms pressure coefficients from the ABL cases have maximum values of up to 0.31 at normal wind directions of 90°. These coefficient decrease when moving away from the normal wind direction towards oblique wind directions, with the exception of an increase from 165° to 180°, especially in the ABL-Tall case. The tornadic rms coefficients matchup with the ABL cases well for some wind directions, being noticeable lower for wind directions below 80°, and deviating upwards after 135° to coefficients of up to 0.19 around 175°. For both tornadic and ABL experiments, the simulated rms coefficients match the measured rms coefficients well, never deviating by more than 0.03.

An important difference to note in the tornadic and ABL rms coefficients is that there is a rapid drop off in the tornadic rms values when the wind direction changes from 85° to 75°. This corresponds to when the vortex has just passed over the building, which shows that the turbulence is much higher near the vortex core than away from it. It should also be noted that the tornadic rms coefficients at wind directions of 40° to 50° are inflated. This inflation is due to the wind direction changing slowly in the later parts of the vortex translation (refer back to Figure 3-1), meaning that the rms is calculated from a larger set of coefficients with a changing mean value that range from vortex locations of y/r = 0.5 to y/r = 4.

The reasons for the differences in the accuracy of the internal pressure model for the tornadic experiments compared to the ABL experiments are similar to the discussions of results in section 3.1. The multiple vortices of the simulated tornado and the translation of the tornado both result in a complicated, non-uniform wind field, even more complicated than that of a stationary single-vortex tornado. As stated earlier and shown in Figure 3-3, the sub-vortices and vertical component of the wind in and around the tornado core make that region highly turbulent, whereas the turbulence is much lower farther away from the core.

Additional reasons for differences between the tornadic and ABL data are discrepancies arising from the experimental setups and the tornadic versus ABL winds. Although the setups are similar in building type, terrain, etc., there are differences in aspects such as building dimensions, opening size, and roof slope. Another difference in the setup between tornadic and ABL wind tunnel tests is the placement of the instruments. Due to the greatly varying wind direction with vortex location in translating tornadic experiments, the Cobra probes need to be placed all around the building. This placement generates more interference of the wind field at the building opening from the probes and their mounts than is present in a typical boundary layer setup. The ABL experiments also included an internal pressure chamber underneath the building model for internal volume scaling, whereas the tornadic WindEEE experiments did not. Although it was expected that the internal pressure model would be able to accurately simulate building internal pressures in tornadic winds, it is not surprising that there is some drop off in accuracy from easier-to-analyze ABL winds. Further differences between tornadic and ABL winds are discussed in the following sections.

3.2.2 Distributions and Fits of Pressures

To explore some of the similarities and differences between tornadic and ABL winds, the pressure coefficient distributions are examined. As mentioned earlier, comparing extreme values between the two studies is difficult due to the uneven spacing of the pressures as a function of wind direction in the current study, and the differences in the setups between the tornadic and ABL wind tunnel tests. Alternatively, the behaviour of the experimental internal pressures can be studied by examining the pressure distributions as probability density functions.

The measured internal pressure distributions are examined in the current study and in both ABL configurations (ABL-Short and ABL-Tall) for two wind directions: 90° and 135°. The reasoning behind these selections is to examine the distributions both at perpendicular peak pressures, and lower oblique pressures. The distributions from the tornadic experiment are taken as 1°, 5°, and 10° increments centred at the wind directions of interest. Due to the results being similar between these three increments, only the 5° increment is discussed in detail in this study. This increment makes for a convenient comparison to the ABL data, similar to the comparison in Figure 3-6. It is also worth noting again that the wind directions from the ABL experiments are only nominal, as the actual wind direction fluctuates significantly (Wu and Kopp, 2016).

A probability density histogram of measured internal pressure coefficient distributions is created for both wind directions of the five mentioned configurations, i.e., the three wind direction increments of the tornadic data and the two ABL configurations (ABL-Short and ABL-Tall). Figure 3-8 shows the probability density of the pressure distributions as blue bars for the tornadic data (top), ABL-Short data (middle), and ABL-Tall data (bottom) for the 90° (left) and 135° (right) wind directions.

A few observations can be made from the pressure distributions in Figure 3-8. All six pressure distributions have a Gaussian appearance, with all 135° configurations having a small positive skew, the 90° ABL configurations having a larger positive skew, and the 90° tornadic configuration having a noticeable negative skew. The reason for the negatively-skewed distribution of the 90° tornadic data, compared to the positively-skewed distribution of the other five cases, likely stems from the 90° tornadic case being the most affected by the large changes in wind speeds and directions due to the sub-vortices of the tornadic flow field, as the tornado

radius is located overtop of or near the building opening in that case. As the vortex moves farther away from the building, which is represented by the 135° tornadic case, the wind field becomes closer to that of ABL flows, which is clearly shown by the distributions in Figure 3-8.

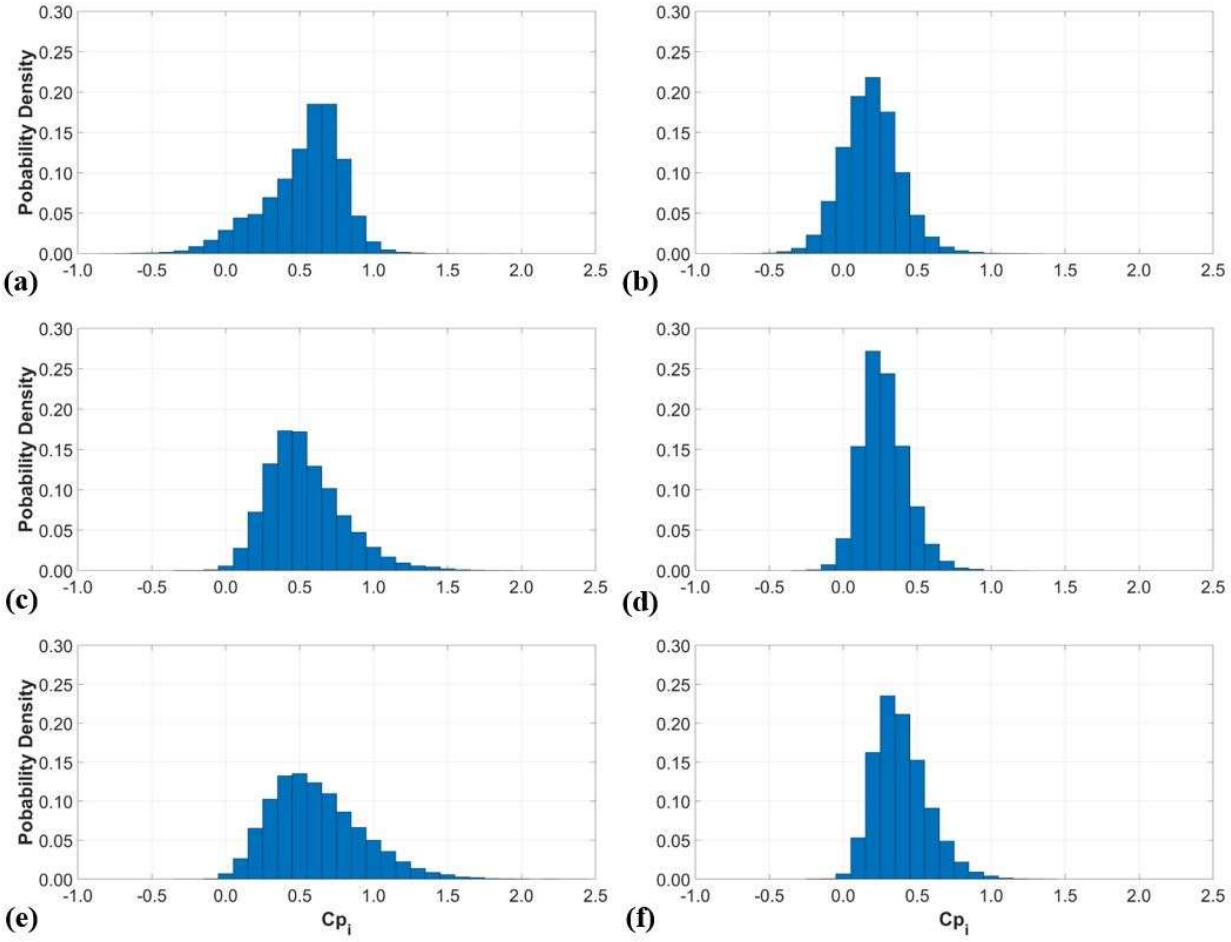

Figure 3-8: Probability density histograms for the measured internal pressure coefficients of the (a) 90° and (b) 135° wind direction from the current study, (c) 90° and (d) 135° wind direction from the ABL-Short case, and (e) 90° and (f) 135° wind direction from the ABL-Tall case.

Another takeaway from Figure 3-8 is that in the ABL cases, the relative increase in the bulk of the internal pressure coefficients when comparing the 90° wind direction to the 135° wind direction is small, whereas the relative increase in the large pressures that make up the top percentiles of the distributions is large. Contrarily, in the current tornadic study, the increase in

the bulk of the internal pressures is relatively large in the 90° versus 135° wind direction, but relatively small in the largest pressures. These differences in pressure and parent distributions is part of what makes comparing the statistical extreme values between the ABL and tornadic data difficult.

In conclusion, the probability density histograms show that there are similarities and differences between ABL and tornadic pressure distributions. The similarities are stronger at more oblique wind directions, where the tornadic wind field is more similar to an ABL wind field due to the vortex being located far away from the building. However, when the vortex is located near the building, the large local fluctuations in the wind speed and directions from the vortex and its sub-vortices alter the pressure distributions.

3.2.3 Analysis of SDE Terms and Spectra

One final analysis of the tornadic and ABL pressures shown in this thesis is a study of the SDE equation terms and their spectra. Figure 3-9 and Figure 3-10 show the time-histories of each of the equation terms from the SDE equation for the tornadic and ABL cases: the driving term (green), the inertial term (blue), and the frictional term (red). Figure 3-9 plots the full time-histories of study, while Figure 3-10 plots a segment of the time-histories for closer analysis. The terms in these time-histories correspond to Eq. 3, repeated below:

$$\underbrace{\frac{\rho l_e V_0}{\gamma A P_0}\ddot{C}p_i}_{\text{Inertial Term}} + \underbrace{\left(\frac{\rho V_0 U_H}{2\gamma A P_0}\right)^2 C_L \dot{C}p_i\left|\dot{C}p_i\right|}_{\text{Frictional Term}} + \underbrace{Cp_i}_{\text{Driving Term}} = Cp_e \qquad \textbf{(3)}$$

with the driving term being defined as ($Cp_e - Cp_i$). The inertial and frictional terms are plotted as their negative values, so that they offset the given definition of the driving term, keeping in mind that it is, namely, the relative magnitudes of the terms that matter in this analysis. The time-histories are plotted for the simulated (SDE) and measured (exp) internal pressure coefficients for the tornadic case from the current study and the same two ABL cases seen throughout this chapter (ABL-Short and ABL-Tall). Additionally, Figure 3-9 and Figure 3-10 contain a configuration of the current study with an increased simulated internal volume to mimic the

effects of internal volume scaling, which is present in the ABL experiments, but not the tornadic experiments. This is done to determine the effects of having a realistic ratio of opening size to internal volume, similar to the ABL cases. To differentiate between the two tornadic cases, they will be referred to as the "regular tornadic case" and the "scaled tornadic case" in this section.

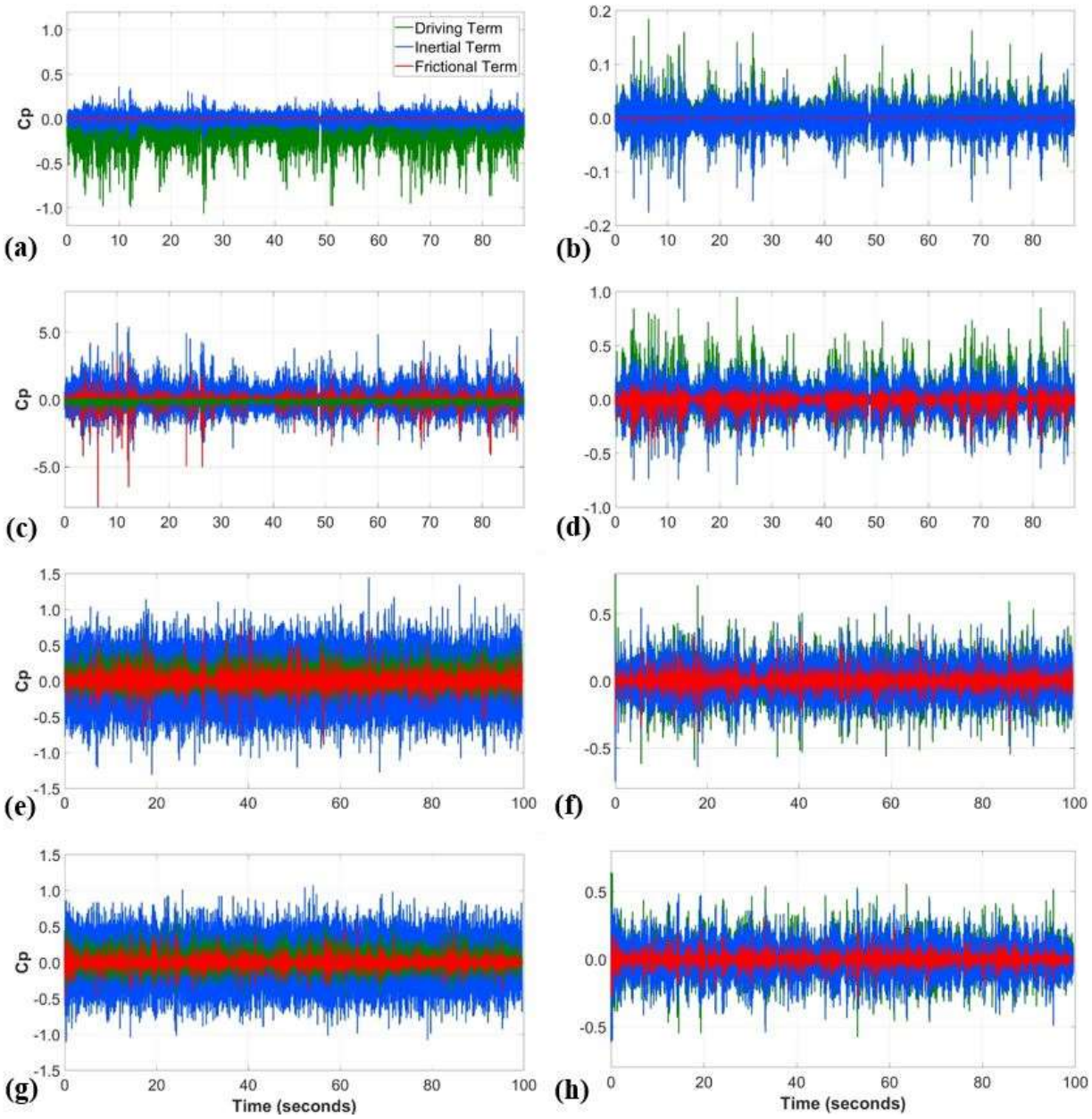

Figure 3-9: Full time-histories of the driving, inertial and frictional terms for the (a) measured and (b) simulated internal pressures of the regular tornadic case, (c) measured and (d) simulated internal pressures of the scaled tornadic case, (e) measured and (f) simulated internal pressures of the ABL-Short case, and (g) measured and (h) simulated internal pressures of the ABL-Tall case.

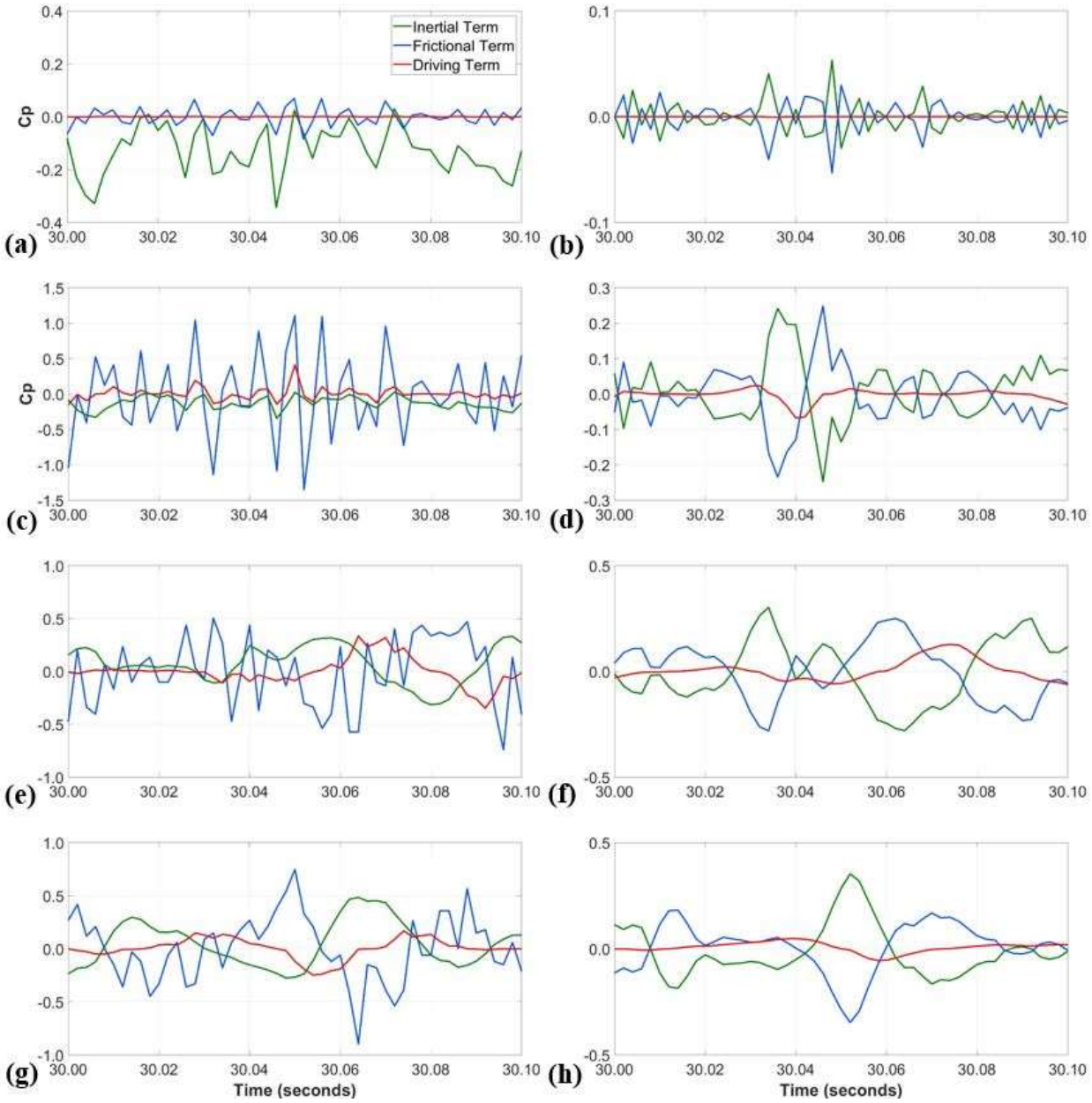

Figure 3-10: Time-history segments of the driving, inertial and frictional terms for the (a) measured and (b) simulated internal pressures of the regular tornadic case, (c) measured and (d) simulated internal pressures of the scaled tornadic case, (e) measured and (f) simulated internal pressures of the ABL-Short case, and (g) measured and (h) simulated internal pressures of the ABL-Tall case.

The time-histories for the ABL cases are taken from the NIST configurations with the wind direction normal to the windward wall (90°). To make an accurate comparison, one second of the time history is taken from each of the 88 trials of the tornadic cases when the wind direction is approximately 90°, and stitched together to make the full time-histories seen in Figure 3-9. This

resulted in similarity between both the wind direction and length of data sampling for the tornadic and ABL cases.

To aid in the comparison of the time-histories, Table 3-2 contains the mean of the absolute values and the rms of each of the equation terms for each configuration, along with the coefficients for each term in Eq. 3 (the term without the Cp component). This table also displays the statistics of the inertial and frictional terms relative to the driving term, to make the trends more observable. It should be noted that the mean of the driving term does not equate to the mean of the frictional plus inertial terms because the mean of the absolute values is used and, for the experimental results, inaccuracy of the model (Eq. 3).

Several observations can be made when examining the measured internal pressure terms, shown on the left side of Figure 3-9 and Table 3-2. The two ABL cases (Figure 3-9(e and g)) are similar to one another, with the inertial term being the largest, followed by the driving term, and then the frictional term. The scaled tornadic case (Figure 3-9(c)) has a similar magnitude of the driving term as the ABL cases, but approximately twice the magnitude in the inertial and frictional terms. The regular tornadic case (Figure 3-9(a)) is significantly different than the other three cases. Here, the inertial and frictional terms are each one or several orders of magnitude smaller than they are in the other cases. This results in the driving term being the largest of the three equation terms and the frictional term being negligible. There is also an imbalance in the terms, i.e., the inertial and frictional terms not balancing out the driving term at each time step, as they are only bound by the SDE equation in theory (whereas the simulated internal pressure equation terms are strictly bound to the SDE equation). This imbalance is most obvious for the regular tornadic case when looking at Figure 3-9(a), but can be seen in all experimental cases when looking at the segments of time-history in Figure 3-10(a, c, e, and g).

When looking at the trends in the simulated internal pressure terms, shown on the right side of Figure 3-9 and Table 3-2, many of the observations made between the measured cases still hold true. The ABL cases (Figure 3-9(f and h)) are similar once again, here with the driving and inertial terms being comparable in mean absolute magnitude, and the frictional term averaging approximately 20% the magnitude of the driving term. The scaled tornadic case (Figure 3-9(d)) is even more similar to the ABL cases than it was for the measured internal pressure terms,

having only slight decreases in the average driving and inertial terms. The regular tornadic case (Figure 3-9(b)) for simulated pressures is by far the most different of the four cases, with a large decrease in all three of the equation terms, and an especially large decrease in the frictional term relative to the driving term, once again making it negligible in the equation.

Table 3-2: Mean of the absolute values and rms of the driving, inertial, and frictional terms for internal pressure coefficients of the tornadic and ABL configurations.

			Measured (exp) Pressures				**Simulated (SDE) Pressures**			
		Equation Term Coefficient	Equation Term Values		Equation Term Relative Values		Equation Term Values		Equation Term Relative Values	
			Mean	rms	Mean	rms	Mean	rms	Mean	rms
Regular Tornadic Case	Driving	1	0.113	0.107	1.00	1.00	0.009	0.014	1.00	1.00
	Inertial	8.64×10^{-7} s^2	0.029	0.040	0.26	0.38	0.009	0.014	1.00	0.99
	Frictional	6.63×10^{-8} s^2	0.000	0.001	0.00	0.01	0.000	0.000	0.01	0.02
Scaled Tornadic Case	Driving	1	0.113	0.107	1.00	1.00	0.078	0.109	1.00	1.00
	Inertial	1.38×10^{-5} s^2	0.472	0.646	4.16	6.04	0.071	0.097	0.91	0.89
	Frictional	1.70×10^{-5} s^2	0.068	0.184	0.60	1.72	0.016	0.033	0.20	0.31
ABL-Short Case	Driving	1	0.096	0.116	1.00	1.00	0.087	0.113	1.00	1.00
	Inertial	4.54×10^{-5} s^2	0.220	0.278	2.29	2.40	0.081	0.104	0.93	0.92
	Frictional	6.36×10^{-5} s^2	0.031	0.061	0.32	0.52	0.018	0.033	0.21	0.29
ABL-Tall Case	Driving	1	0.089	0.114	1.00	1.00	0.084	0.109	1.00	1.00
	Inertial	5.15×10^{-5} s^2	0.197	0.249	2.21	2.19	0.080	0.102	0.95	0.94
	Frictional	5.44×10^{-5} s^2	0.023	0.045	0.26	0.40	0.015	0.028	0.18	0.26

There are a few notable differences when comparing the equation terms from the measured and simulated internal pressures over all four cases. Examining Figure 3-9 and Table 3-2, the driving

term changes little from the respective cases of measured to simulated pressures, with the exception of the regular tornadic case, but there is a large decrease in the inertial and frictional terms, especially for the scaled tornadic case. What stands out in Figure 3-10, is that the terms must balance each other in the simulated right-side graphs, which means the addition of the inertial and frictional terms is always equal to the negative of the driving term. For the regular tornadic case, with minimal influence of the frictional term, this results in the inertial term always being equal and opposite to the driving term (Figure 3-10(b)). Because the terms do not need to be balanced in the measured cases, there is also a lack of symmetry about $Cp = 0$ in those cases, especially in the driving term of the tornadic cases, which is mostly negative. This indicates that the measured internal pressure is typically larger than the external pressure, which is related to the Helmholtz resonance.

In both the case of measured and simulated internal pressure terms, the scaled tornadic case is significantly more similar to the ABL cases than the regular tornadic case. This is not surprising, as the opening to internal volume ratio of the scaled tornadic case is similar to the ABL cases, while the opening to volume ratio of the regular tornadic case without internal volume scaling is much larger, due to the smaller internal volume. This trend can also be noted in the equation term coefficients of Table 3-2, where the coefficients for the regular tornadic case are several orders of magnitude smaller than the coefficients for the other three cases.

Figure 3-11 shows the spectra of each of the equation terms from the SDE equation for the same configurations as Figure 3-9 and Table 3-2, comparing the measured and simulated internal pressure terms from the tornadic and ABL cases. These spectra are calculated computationally using the Welch method. The time-histories shown in Figure 3-9 are broken into equally-spaced, one-second segments without overlap for each plot. This results in 88 segments for the tornadic cases, one for each trial, and 100 segments for the ABL cases. These segment lengths compare reasonably with the integral time scales of approximately 0.4 seconds for the tornadic cases and 0.1 seconds for the ABL cases. The goal is to have the segments be short enough to reduce the noise in the spectra, but long enough to be several factors larger than the fluctuations represented by the integral time scale.

The frequency of the spectra are normalized in each configuration by dividing by their respective Helmholtz (natural) frequency, obtained from the below equation from Holmes (2015).

$$f_H = \frac{1}{2\pi}\sqrt{\frac{\gamma A P_0}{\rho l_e V_0}} \quad \textbf{(10)}$$

To obtain the spectra plotted in Figure 3-11, the spectral density estimate obtained from Welch's method ($S(f)$) is multiplied by the frequency of the given equation term (f) and then divided by the variance of the driving term (σ^2) for the given configuration.

Several trends can be noted in the spectra of the measured internal pressure terms in Figure 3-11, many of which are parallels to trends seen in Figure 3-9 and Figure 3-10. The ABL cases (Figure 3-11(e and g)) have similar spectra, with mostly monotonically increasing energy as the frequency increases to the natural frequency, at which point the spectra mostly decreases in energy with further increasing frequency, with the exception of a second large peak at a frequency 7-8 times larger than the natural frequency, seen especially in the inertial term. At the low frequencies, the driving term contains the most energy, followed by the frictional term and then the inertial term. Shortly before the natural frequency, the inertial term eclipses the other two terms in energy content and remains the dominant term for all higher frequencies. This trend coincides with the inertial term being the dominant of the three equation terms for the ABL cases in Figure 3-9.

When comparing the spectra of the measured ABL terms to the scaled tornadic case (Figure 3-11(c)), the scaled tornadic case has higher energy for the higher frequencies of all three terms. Due to a higher natural frequency, there is also a shift towards a lower frequency range of normalized values. The energy spike in the spectra is located at a frequency four times greater than the theoretical natural frequency, although this is due to the fact that the actual natural frequency of the building is based on the smaller actual internal volume and not the larger simulated internal volume. The regular tornadic case (Figure 3-11(a)) has a few significant differences from the other three cases. First, the driving term dominates the other terms at all frequencies except the highest ones, where the spectra of the inertial term converges with the driving term around the natural frequency. This natural frequency is also higher for this case,

resulting in a larger shift towards lower normalized frequencies, with few frequencies above the Helmholtz frequency. The frictional spectra is also insignificant in energy relative to one or both of the other terms for all frequencies of the regular tornadic case, which was also noted in Figure 3-9(a).

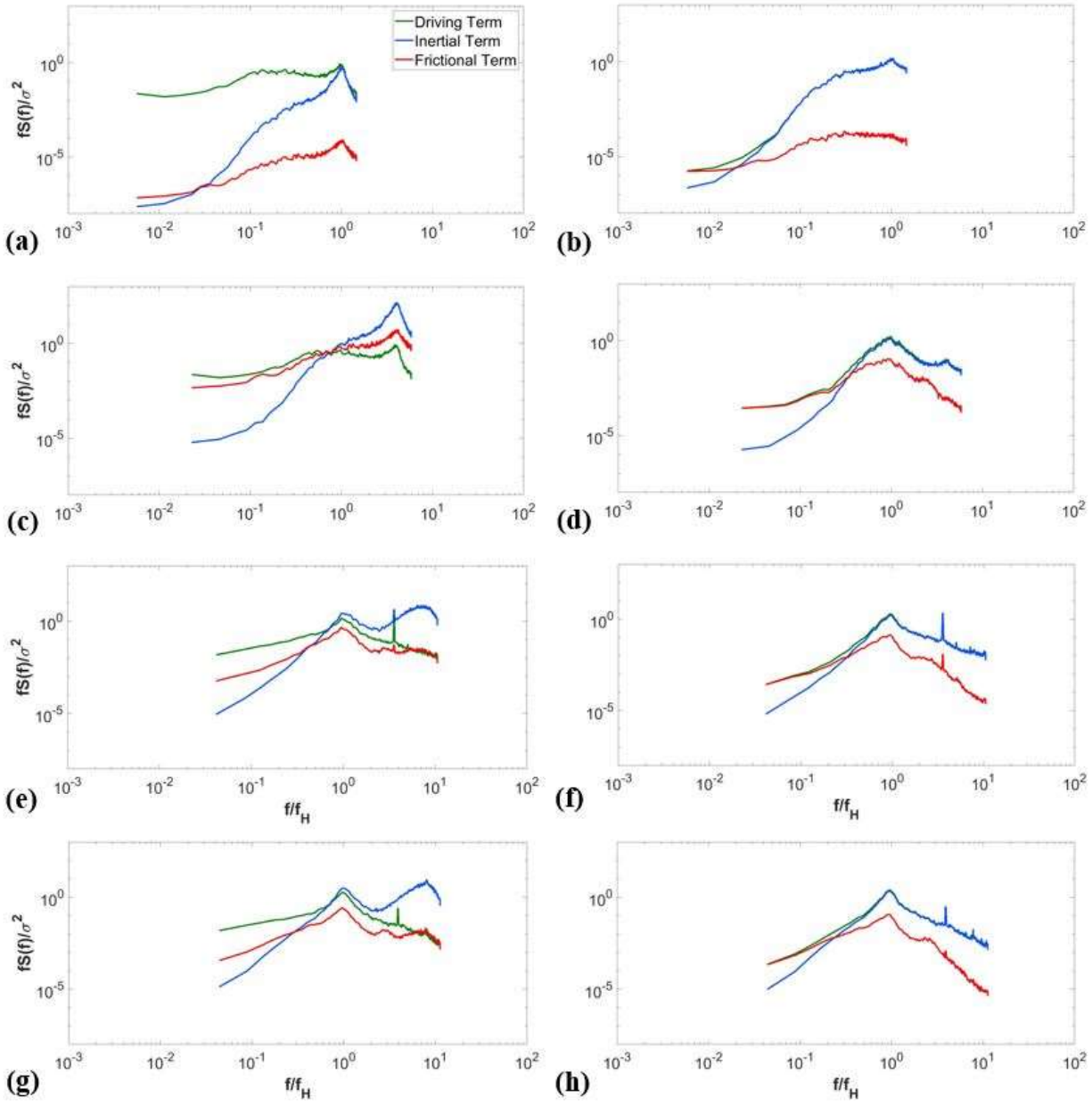

Figure 3-11: Spectra of the driving, inertial and frictional terms for the (a) measured and (b) simulated internal pressures of the regular tornadic case, (c) measured and (d) simulated internal pressures of the scaled tornadic case, (e) measured and (f) simulated internal pressures of the ABL-Short case, and (g) measured and (h) simulated internal pressures of the ABL-Tall case.

When examining the spectra of the simulated internal pressure terms, there is a lot of similarity between the four cases. Across all cases, similar to the measured pressure spectra, all terms are generally increasing in energy prior to the natural frequency and decreasing afterwards, while the driving and frictional terms dominate the lowest frequencies with the inertial term dominating the remaining frequency range. The spectra for the driving term matches the frictional term at low frequencies; then, sometime before the natural frequency is reached, transitions to matching the inertial term at high frequencies. This match makes it such that the driving term is hidden by the inertial spectra in the graphs at higher frequencies. Similar to earlier noted trends, the high energy of the driving and inertial terms at the higher frequencies aligns with the dominance of the driving and inertial terms in Figure 3-9(d, f, and h).

The two ABL cases (Figure 3-11(f and h)) for the simulated equation terms once again have similar spectra, while the scaled tornadic case (Figure 3-11(d)) has similar trends with some minor differences from the ABL cases, and the regular tornadic case (Figure 3-11(b)) has more significant differences from the other three cases. Compared to the ABL cases, the scaled tornadic case has a shift in the spectra towards lower normalized frequencies and has secondary small peaks in the equation terms at high frequencies. In the regular tornadic case, the shift in the normalized frequency range is more pronounced, with hardly any spectra appearing at frequencies higher than the natural frequency. The natural frequency peak is also less prominent for all the equation terms, and missing for the frictional term. Additionally, there is a large decrease in the energy of the driving term at low frequencies, and the frictional term across all frequencies.

Although the spectra from the measured and simulated equation terms share many trends, there are some notable differences when comparing the two. The most glaring difference is that the energy of the driving and frictional terms are less for the lower frequencies in the simulated equation terms, with the exception of the frictional term in the regular tornadic case. In both the spectra from the measured and simulated equation terms, the regular tornadic case has spectra noticeably different from the other three cases. As mentioned earlier, this is likely due to the lack of internal volume scaling present in that configuration.

To complement the spectra of the equation terms, Figure 3-12 and Figure 3-13 plot the spectra of the external and internal pressures themselves, from the tornadic and ABL cases, respectively. Following earlier plotting convention, the external pressure is plotted in green, the simulated internal pressure in blue, and the measured internal pressure in red. The spectra are plotted from the same time histories as Figure 3-11 with a wind direction of 90° for both the tornadic and ABL cases, and are broken up into the same number of segments. In these spectra, σ^2 represents the variance of the external pressure coefficient of the respective time-history.

For the regular tornadic case, depicted in Figure 3-12(a), the spectra reveal the similarity in the measured and simulated internal pressures. This similarity, discussed earlier in the chapter, is the cause of the low magnitude and spectra of the simulated driving term for the regular tornadic case, which directly leads to low inertial and frictional terms as well. The spectra of the measured internal pressure is similar to the other spectra at lower frequencies, but contains noticeably higher energy at the natural frequency due to Helmholtz resonance. This resonance is clearly not fully captured by the simulated internal pressure.

Figure 3-12(b) is different from Figure 3-12(a) only in that the simulated internal pressure is based on the scaled tornadic case with a larger internal volume. The measured external and internal pressures are taken directly from the experimental testing, so there is no change in their spectra. What this graph reveals is that scaling the internal volume results in spectra for the simulated internal pressure that look much different than the external pressure or the simulated internal pressure from the regular tornadic case. As has been shown throughout this section, the internal volume scaling significantly alters the internal pressures.

Figure 3-13(a) plots the spectra for the ABL-Short case while Figure 3-13(b) plots the spectra for the ABL-Tall case. As seen throughout this analysis of equation terms and spectra, there is once again little difference between the two cases. In both figures, there is an energy spike in the spectra at the natural frequency for both internal pressures that is not clearly reflected in the measured external pressure. In other words, the spectra of the simulated internal pressure is more similar to the measured internal pressure than the measured external pressure, which contrasts with the trends seen in the regular tornadic case. This coincides with the fact that the changes in

the magnitudes and spectra of the equation terms of the ABL cases change relatively little between the simulated and measured cases, when compared to the tornadic cases.

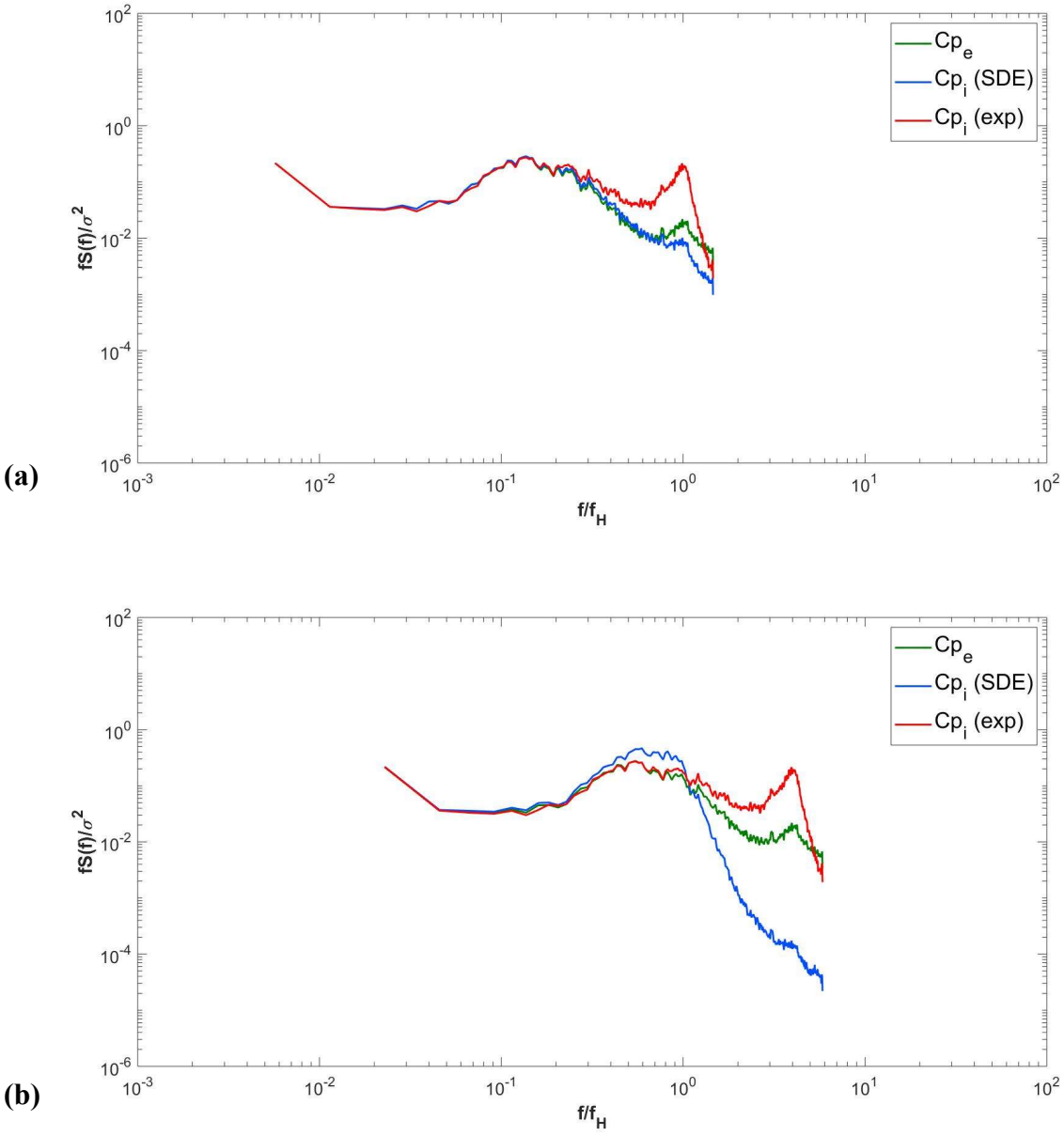

Figure 3-12: Spectra of the external, simulated internal, and measured internal pressure coefficients of the stitched-together tornadic cases at 90° with (a) regular internal volume and (b) scaled internal volume.

An important observation when comparing Figure 3-12 to Figure 3-13 is that the spectra of the simulated internal pressure for the scaled tornadic case is significantly more similar to the ABL cases than the regular tornadic case is. This is a trend noted throughout this entire section, implying that internal volume scaling in tornadic wind tunnel testing may lead to more accurate simulations of the measured internal pressure.

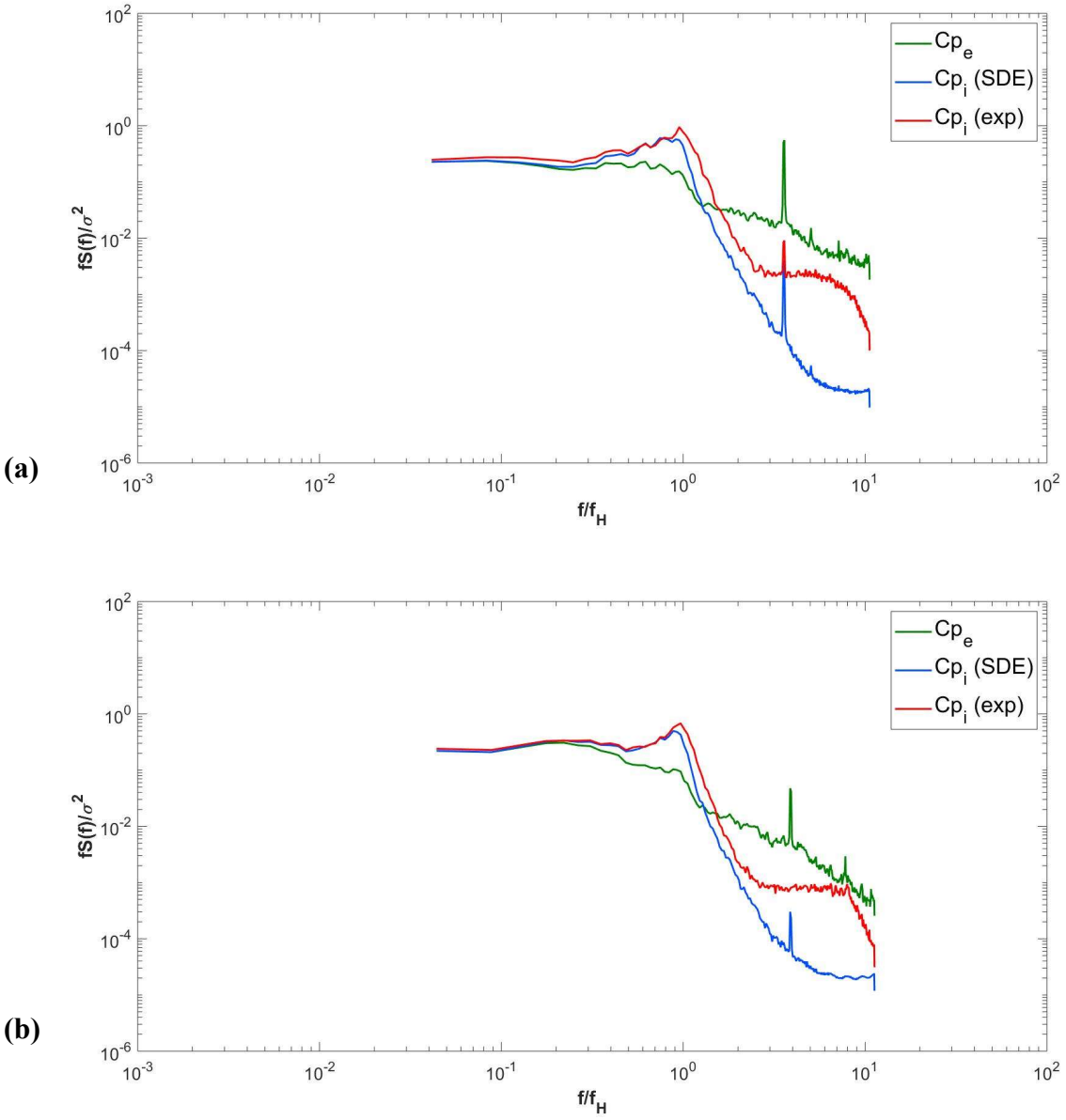

Figure 3-13: Spectra of the external, simulated internal, and measured internal pressure coefficients at a wind direction of 90° for the (a) ABL-Short case and (b) ABL-Tall case.

3.3 Summary

The first half of this thesis uses a theoretical model based on the single discharge equation with the Helmholtz resonator concept to simulate internal pressures in a low-rise building from external pressures at a dominant opening in a tornadic wind tunnel test. These simulated internal pressures are then compared to experimental measured internal pressures from inside the building. Lastly, a comparison of the tornadic internal pressures is done for certain configurations from the boundary layer wind-tunnel NIST experiments, using the same computational model. The following conclusions can be made from the results.

- In the tornadic (WindEEE Dome) testing analysis, the model-simulated internal pressures generally agree with the measured internal pressures, with some differences. There is a minor, consistent offset of the SDE simulated internal pressures being lower than the experimental measured internal pressures. When looking at ensembles averages of pressures in 5° wind direction increments, the difference in mean internal pressure coefficients ranges from 0.04 at oblique wind directions, to 0.11 at wind directions near 90° (when the vortex radius is right over the building), with a mean difference of 0.07. These differences are partly within the uncertainty of ±0.07. The rms simulated and measured internal pressure coefficients agree very well, having coefficients with differences no greater than 0.03 from each other across all wind directions.
- When comparing ABL wind tunnel analysis to the tornadic results, the internal pressure model simulates the internal pressures caused by ABL winds more accurately than those produced by tornadic winds. When comparing simulated and measured mean internal pressures, the NIST results show a similar offset of the simulated pressures underestimating the actual pressures. The difference is less than in the current tornadic study, however, with coefficient differences of up to 0.05, with mean differences of 0.03 and 0.01 in the two relevant configurations, all within measurement uncertainty.
- Although tornadic and ABL winds are similar, there are differences that partially explain the discrepancies in the SDE model when used for tornadic winds. When examining the pressure distributions and parent fits for both types of wind experiments, the distributions of tornadic and ABL pressures are similar for oblique wind directions, but different for normal wind directions. This is due to tornadic wind fields being more similar to ABL

winds away from the vortex core, but different than ABL winds near the vortex core, where the sub-vortices and vertical component of the wind result in large fluctuations in the wind speeds and directions.

- Examination of the time-histories and spectra of the SDE equation terms for the simulated and measured internal pressures of tornadic and ABL winds led to the conclusion that internal volume scaling in the tornadic wind tunnel studies makes the internal pressures behave more similarly to ABL-induced pressures. Without internal volume scaling, the smaller volume of the regular tornadic case results in small driving terms of the SDE equation due to the similarity of the simulated internal pressure to the external pressures, which coincides with small responses from inertial and driving terms.

Overall, the main conclusion from the WindEEE analysis is that tornadic and ABL winds have differences, especially when the vortex is near the building and is producing normal wind directions at the opening, but are similar enough to allow the theoretical model to reasonably simulate the internal pressures from the external pressures at the opening. The model is less accurate in tornadic winds compared to ABL winds, but this may be mitigated with internal volume scaling. More work could be done to further this study and its conclusions, which will be discussed in Chapter 5.

4. Internal Pressures in Residential Garages

In this chapter, based on the similarities of ABL and tornadic winds, ABL wind data is used to assess the failure capacity of garage doors. Since the magnitude of peak pressures on low-rise building walls is similar in tornadic and ABL wind flows, simpler and more readily available ABL data is used to assess the effects of door flexibility and load-dependent openings. This is a common simplification when the size of the element of study (the garage door) is small relative to the size of the tornado. The reader is reminded that the objective of this chapter is to obtain the ratio of peak net pressure to peak external pressure in order to determine the wind speeds required to general garage door failures.

4.1 Internal Pressure Model Results

4.1.1 Fixed and Flexible Opening Cases

In order to better understand the effects of garage door flexibility and variable open areas, two cases of fixed openings are examined initially with the MDE. The first case has a small fixed garage door opening of 0.1% of the front wall area (0.0104 m^2), representing a leakage case with the garage door closed, and the second case has an open area of 1.0% (0.104 m^2), which represents the relatively large opening caused by the door bending just prior to failure. This range of cases will give a baseline of how the pressures depend on open area. In both cases, there is a leakage area of 0.1% on each of three non-windward walls, with static external pressure time histories at these points. Many assumptions could be made here as garage structures vary significantly in terms of the amount of leakage they allow based on how they are integrated into a house, and based on the overall house and garage shape. The assumption here is fairly simple, but represents a common case where each wall allows leakage through other doors or windows.

Figure 4-1(a) depicts the external, internal, and net pressures, as a function of (full-scale) time, which is shown in seconds, for a segment of the time series for the nominal leakage case. These segments of the time history allow for an examination of the effects of leakage on the pressures, especially near the peak values. The external pressure (green) time history is taken from the NIST database, as explained above, while the internal pressure (blue) is calculated using the MDE, and the net pressure (red) is calculated via the difference between the external and internal

pressure. The data in the figure are presented in full-scale dimensions because the open area in later calculations depends on the dimensional full-scale loads. The conversion to full-scale depends on the mean roof height wind speed, which is taken as 36 m/s, similar to the value used by Oh et al. (2007). Of particular importance in the external pressure time history are the peak pressures, with intermittent, large values. The largest peaks typically last for durations of less than a second, such as the one centred at about 560 seconds in Figure 4-1.

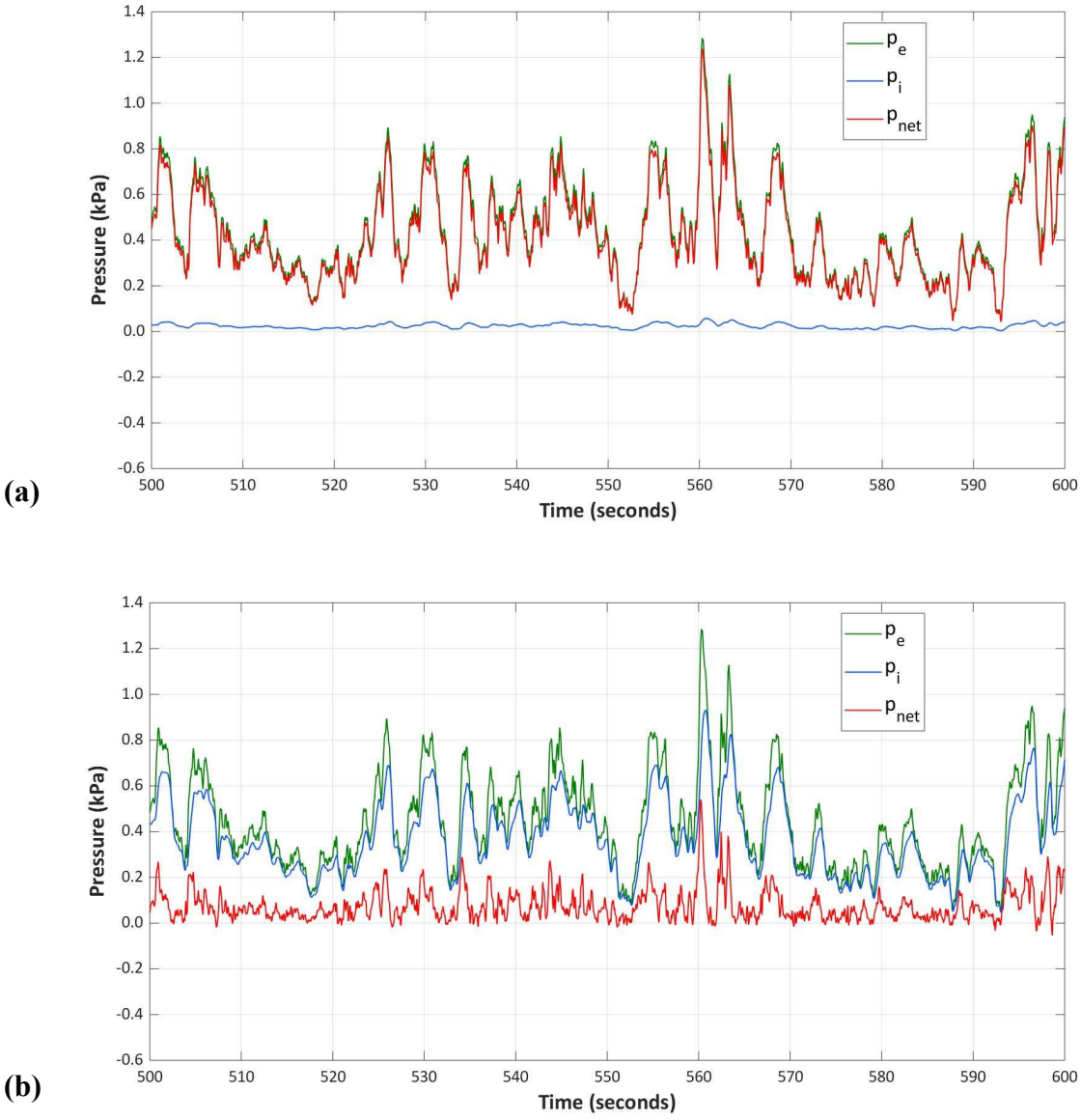

Figure 4-1: Time-history of external, simulated internal, and net pressure over a small section of the time series of a garage door sample with a fixed opening area of (a) 0.1% and (b) 1.0%.

The small leakage opening coupled with the allowance for leakage on all walls results in a mean internal pressure just above zero with minimal variation. The relatively steady internal pressure variation, with close to zero mean pressures, is well-known for leakage cases (e.g., Oh et al., 2007). There is a slight increase in internal pressure when there is a relatively high external pressure and a slight decrease for the lower external pressures. Overall, this results in the net pressure tracking the external pressure closely, with small differences seen mostly when the external pressure reaches peaks. However, the peak net pressures have little reduction with respect to the external pressures. For example, the peak at 560 seconds, with an external pressure of 1.29 kPa, yields a net pressure of 1.24 kPa, such that the ratio of peak net pressure to peak external pressure is 0.96. In fact, because the internal pressure is almost constant in time, the net pressure at the moment of the peak is approximately equal to the peak external less the mean internal pressure.

Figure 4-1(b) shows the same segment of time history as Figure 4-1(a), but for the relatively large (1%) opening case. Once again, the full-scale external, internal and net pressures are plotted as a function of time and, because the same external pressure time series is used, the effects of the open area become visible. As expected, the relatively large open area results in nearly instantaneous changes to the internal pressure when the external pressure changes. The internal pressure closely follows the values and changes in the external pressure, with slightly smaller fluctuations and peaks for this case. However, there is a small delay, on the order of 250 milliseconds (full-scale). This delay is also present in the measurements shown in Oh et al. (2007), and is caused by the relatively slow (compared to the speed of sound) physical movement of fluid into or out of the internal volume that causes the changes to the internal pressure. In this case, the mean net pressure is just above zero because of the small differences between the external and internal pressures. However, when there are rapid changes of the external peak pressures, which result in large peaks, the lag in the internal pressure for this open area size does not allow the internal pressure to attain values as large as the external before the external pressure drops back down. This can be shown quantitatively, for example, for the external and net pressure peaks at 560 seconds, where the net pressure is 0.54 kPa, resulting in a ratio of net to external peak pressures of 0.42. The important consequence of this is that there is much smaller applied load on the garage door compared to the case with only leakage openings.

In fact, if the garage door was more flexible, but strong enough to allow even larger open areas, the net load on the door would be even smaller.

Using the quasi-steady response assumption, the process of determining the failure wind speed could be as simple as using a fixed opening case with an opening size around the failure opening size. However, it is not clear that this should be the case because of the time lags between the external and internal pressures, which may be enhanced by the variable nature of the open area as the garage door bends in response to the net load. Hence, the accuracy of this assumption is scrutinized by running a flexible garage door opening case. To simplify the calculations, the fluctuating opening case is analyzed with the SDE to examine these effects.

Figure 4-2 introduces the flexible garage door model, which leads to a fluctuating open area. This creates a more dynamic relationship between the pressure and the area. Once again, the same segment of time series is shown, and, since the changes in the opening size are now important, they are plotted in Figure 4-2(b) along the same x-axis. The relationship between the open area size and the net pressure is governed by Figure 2-5(c). All garage door models that had open area versus net pressure tracked, have similar curves, and therefore, one relationship is used for all experimentally tested flexible garage door models. As mentioned, the SDE is used to produce the results for Figure 4-2; however, the net pressure from the MDE large opening case from Figure 4-1(b) is included as well, for comparison.

At first glance, the internal pressure time history in Figure 4-2 appears different from both the leakage and large opening cases. The internal pressure is clearly affected by the external, with much larger fluctuations than seen in the leakage case; however, it does not completely follow the external pressure as seen in the large opening case. This is, of course, due to the fact that the open area, shown in Figure 4-2(b), is alternating between being closed (i.e., the leakage case) and pushed open by large external pressure peaks (i.e., the large opening case).

Somewhat surprisingly, the mean internal pressure is noticeably higher than the mean external pressure. For example, the internal pressure is continuously higher than the external pressure from 505 to 523 seconds in the time history, and then again from 569 seconds to 583 seconds. This is due to the rate of increase in the internal pressure during external pressure spikes being higher than its rate of decrease during external pressure lows. Whenever a large spike in the

external pressure occurs, it results in the door opening (e.g., 525 second mark). This causes a rush of air to quickly increase the internal pressure. Then, as the external peak reduces, the net pressure also reduces and closes the openings around the garage door. In contrast, when the external pressure drops with a closed door, the internal pressure decreases, but is forced to do so at a slower rate due to only allowing leakage outwards in the SDE setup. This is different than the fixed opening cases where the internal pressure can escape more easily through the leakage in the other walls.

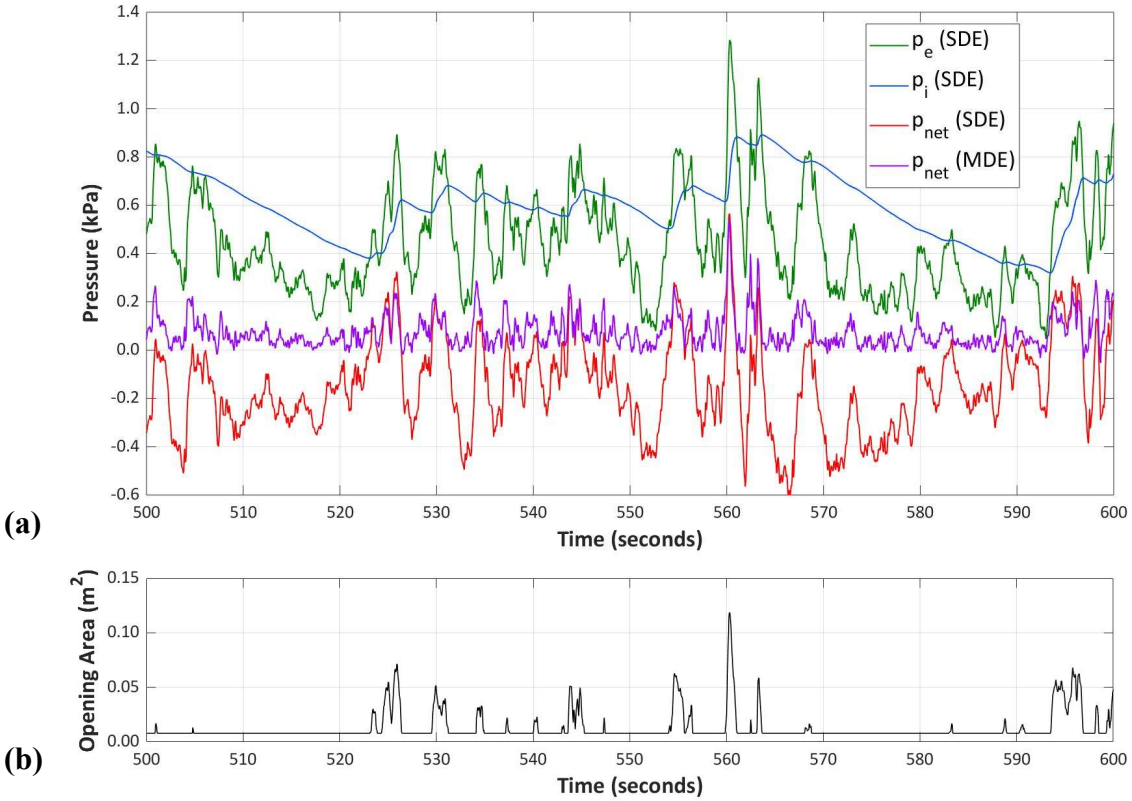

Figure 4-2: Time-histories of (a) external, simulated internal, and net pressure for the SDE using a flexible garage door, and the net pressure for the MDE for a fixed garage door opening of 1% of door area, and (b) the open area as a function of time for the flexible garage door.

The most important takeaway from Figure 4-2 is related to the net pressures. When comparing the red SDE and purple MDE net pressures, it is clear that the mean net pressure for the SDE flexible opening case is significantly lower than in the large fixed opening MDE case. However, during the moments of the largest wind gusts, such as the external pressure peak at 560 seconds,

the net pressures are similar. This location, for example, yields a net pressure of 0.57 kPa and a ratio of peak net to external pressure of 0.44 for the SDE flexible case, which is close to the MDE fixed opening net pressure and ratio of 0.54 kPa and 0.42, respectively. This shows that the MDE large opening case can yield a good estimation of the flexible opening case for the failure wind gusts, and that the SDE flexible opening case works adequately without the additional leakage openings.

Table 4-1 summarizes the most important statistical parameters of the three opening cases discussed so far, as well as two additional flexible opening cases, which will be discussed in the following section. The open area in the table provides the size of the garage door opening as a percentage of the front wall area for the fixed opening cases. For the flexible opening cases, the maximum and mean opening sizes are provided. One can see that, although the mean opening size for the flexible opening case is close to the leakage opening size, the maximum opening size shows that the peak values in the opening size exceed even the large opening case at times. The maximum external, internal, and net pressure coefficients are found through a Lieblein (1974) BLUE analysis, with the median values taken from the local extreme values of dividing the time histories into 10 equal segments. The ratio of peak net to peak external pressure is a key parameter to later determine the failure wind speeds of the garage doors, as explained earlier.

As would be expected, the peak internal pressure is higher for the large and flexible opening cases, and close to zero for the leakage opening case. This is directly correlated to how quickly the internal pressure can match the peaks of the external pressure, which is related to the size of the opening during the external pressure peaks. Therefore, for the large and flexible opening cases, the peak internal pressures are closest to the peak external pressure. Once again, due to the identical external pressure between the cases, the trends from the maximum net pressures directly correlate with the internal pressures. This causes the leakage case to have the highest maximum net pressure due to its lower peak internal pressure and the large opening case to have a lower maximum net pressure due to its higher peak internal pressure. The maximum net pressure for the flexible opening case is similar to that of the large opening case.

As mentioned, the ratio of maximum net pressure to maximum external pressure is an important parameter. From Table 4-1, the leakage case has the highest ratio of 0.96, the large opening case

has a lower ratio of 0.35, and the flexible opening case has a ratio of 0.41, similar to the large opening case. This shows that a larger opening size leads to a greater reduction in the peak net pressures.

Table 4-1: Open area and pressure means and maxima of fixed and flexible opening cases.

Door Model	Leakage Opening	Large Opening	Flexible Opening	More-Flexible Opening	Less-Flexible Opening
Open Area (%)	0.10	1.00	Max: 1.53	Max: 2.38	Max: 0.93
			Mean: 0.12	Mean: 0.14	Mean: 0.11
$\overline{Cp}_e$	0.58	0.58	0.58	0.58	0.58
$\widehat{Cp}_e$	1.63	1.63	1.63	1.63	1.63
$\overline{Cp}_i$	0.03	0.49	0.75	0.80	0.70
$\widehat{Cp}_i$	0.08	1.22	1.18	1.30	1.07
$\overline{Cp}_{net}$	0.55	0.10	-0.17	-0.21	-0.12
$\widehat{Cp}_{net}$	1.56	0.56	0.66	0.56	0.75
$\widehat{Cp}_{net}/\widehat{Cp}_e$	0.96	0.35	0.41	0.34	0.46

4.1.2 Other Flexible Opening Cases

To check the sensitivity of the results, two additional flexible opening models are created with the SDE method. The first model has twice the flexibility while the second model has half the flexibility. These models are created by simply doubling and halving the slope of the open area - net pressure curve used for the flexible opening case, as shown in Figure 4-3. The flexible opening area versus net pressure curve is taken as a linear fit to the combined garage door data from experimental testing in Figure 2-5(c). The zero offset in all three models represents the leakage opening of 0.1% of the garage door area, as mentioned earlier.

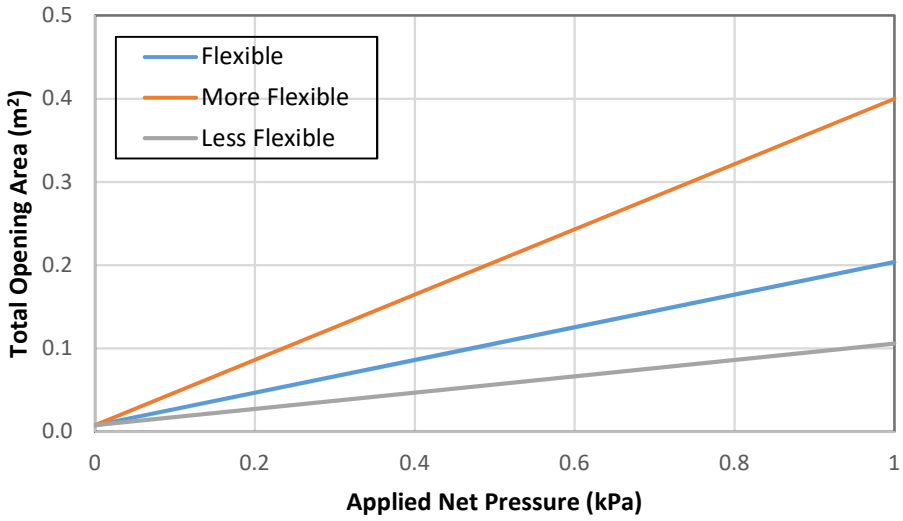

Figure 4-3: Simplified version of total opening area as a function of applied net pressure for the three flexible opening models.

The statistical results of the additional flexible opening cases can be found in Table 4-1. In the more-flexible-opening case, since the open area is now twice as sensitive to the net pressure, the fluctuations in the internal pressure are increased. In other words, the external pressure peaks result in larger openings of the garage door, leading to larger peaks in the internal pressure. This leads to both a higher peak and mean internal pressures compared to the flexible opening case.

Interestingly, because the mean internal pressure is higher in the more-flexible-opening case, the net pressure is positive less of the time. Therefore, although the garage door opens wider during large external peaks, the door is actually closed for a larger portion of the time series compared to a less flexible opening case. As always, the trends in the internal pressure create the opposite trends in the net pressure. For the more-flexible-opening case, this means that the larger mean and peak internal pressure lead to smaller mean and peak net pressures. These smaller peak net pressures then directly result in a lower peak net to peak external pressure ratio, taking some of the load off of the door.

For the less-flexible-opening case, as would be expected, the opposite trends to the more-flexible-opening case are observed, relative to the original opening case. Since the open area is now half as sensitive to the net pressure, the fluctuations in the internal pressure are less than the other flexible opening cases, resulting in a lower peak and mean internal pressure. This is due to

the more rigid garage door not opening as wide and hindering the increase of the internal pressure during external pressure spikes. The less-flexible-opening case also results in larger (more positive) mean and peak net pressures. This leads to higher peak net to peak external pressure ratios, meaning more of the applied external pressure is being felt by the door as net pressure.

Overall, the most important takeaway from the additional flexible opening cases is that the increased flexibility leads to higher internal pressures, which, in turn, leads to lower peak net to peak external pressure ratios. In other words, for a fixed garage door capacity or strength, a more flexible door would be more resilient. Of course, these higher internal pressures will, at some point, begin to have negative effects on other components of the structure, such as the roof.

4.1.3 Other Wind Directions

Because tornadoes can have significant swings in wind direction during their passage past any building, wind directions other than normal to the opening are also studied, with a focus on the range where the net loads would be inwards. In this analysis, the wind direction normal to the wall is defined as 270°, while the wind direction parallel to the wall is defined as 360°. Figure 4-4(a) and Figure 4-4(b) plot the mean and maximum internal pressure coefficients, respectively, as a function of wind angle from 270° to 360° in 15° increments for each of the six opening types studied in the internal pressure model. The external pressure is also plotted, which is identical for all opening types.

In Figure 4-4(a) and Figure 4-4(b), it appears that the relationship with wind direction is similar for all mean and maximum internal pressures across the five openings conditions with the exception of the leakage opening case, which has internal pressures consistently close to zero. For the other four opening cases, the pressures are about the same from 270° to 285°, but then decrease monotonically to 360°. For most of this range, between 300° and 345°, this decrease is well approximated as linear. It is well known through the literature that external positive pressures in the centre of a windward face of a wall are highest when the winds are perpendicular; therefore, it is not surprising that the more oblique and parallel winds lead to lower internal pressures due to the lower external pressures.

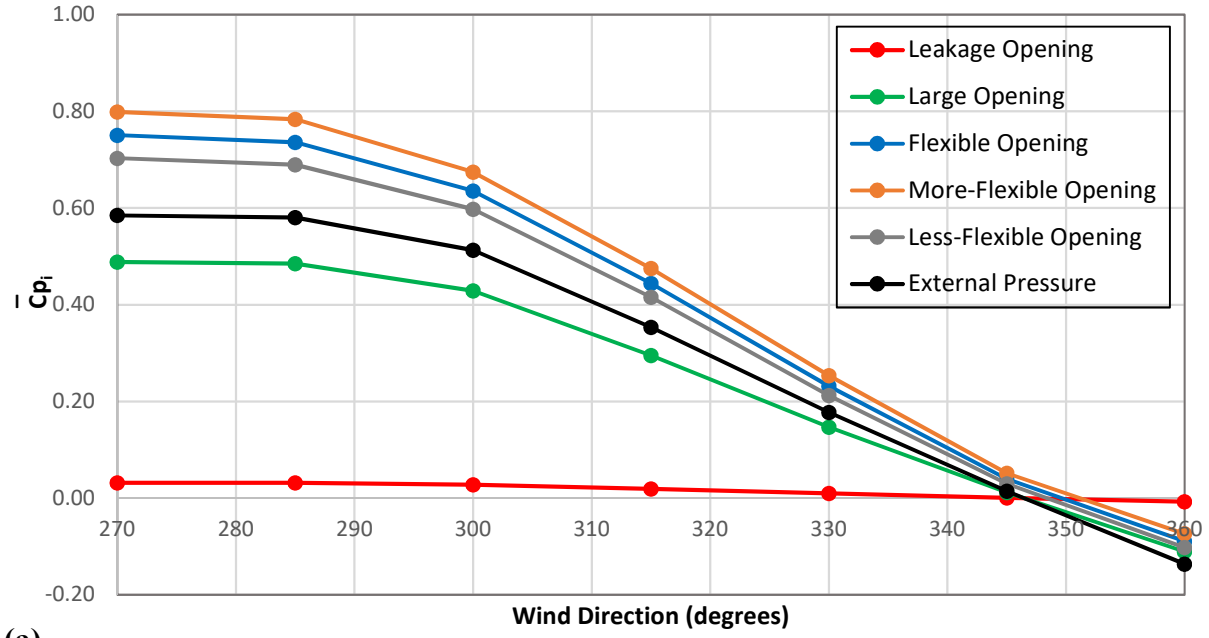
1.00
0.80
0.60
0.40
0.20
0.00
-0.20
270
280
290
300
310
320
330
340
350
360
Leakage Opening
Large Opening
Flexible Opening
More-Flexible Opening
Less-Flexible Opening
External Pressure
Wind Direction (degrees)

(a)

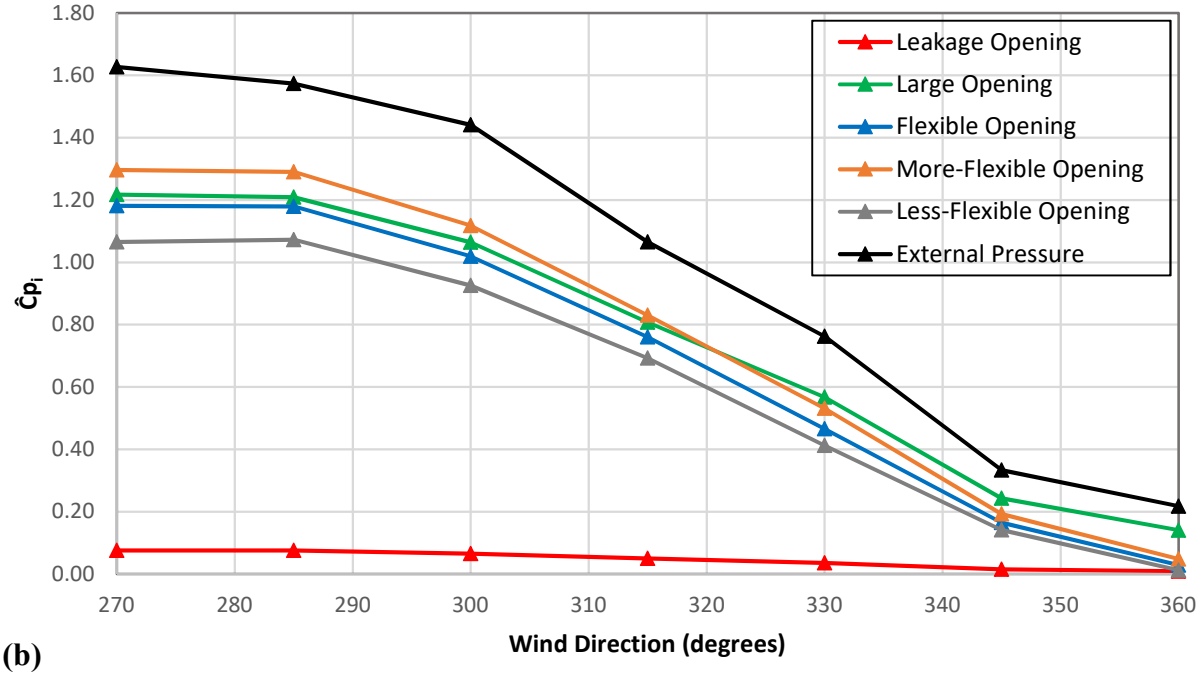
1.80
1.60
1.40
1.20
1.00
0.80
0.60
0.40
0.20
0.00
270
280
290
300
310
320
330
340
350
360
Leakage Opening
Large Opening
Flexible Opening
More-Flexible Opening
Less-Flexible Opening
External Pressure
Wind Direction (degrees)

(b)

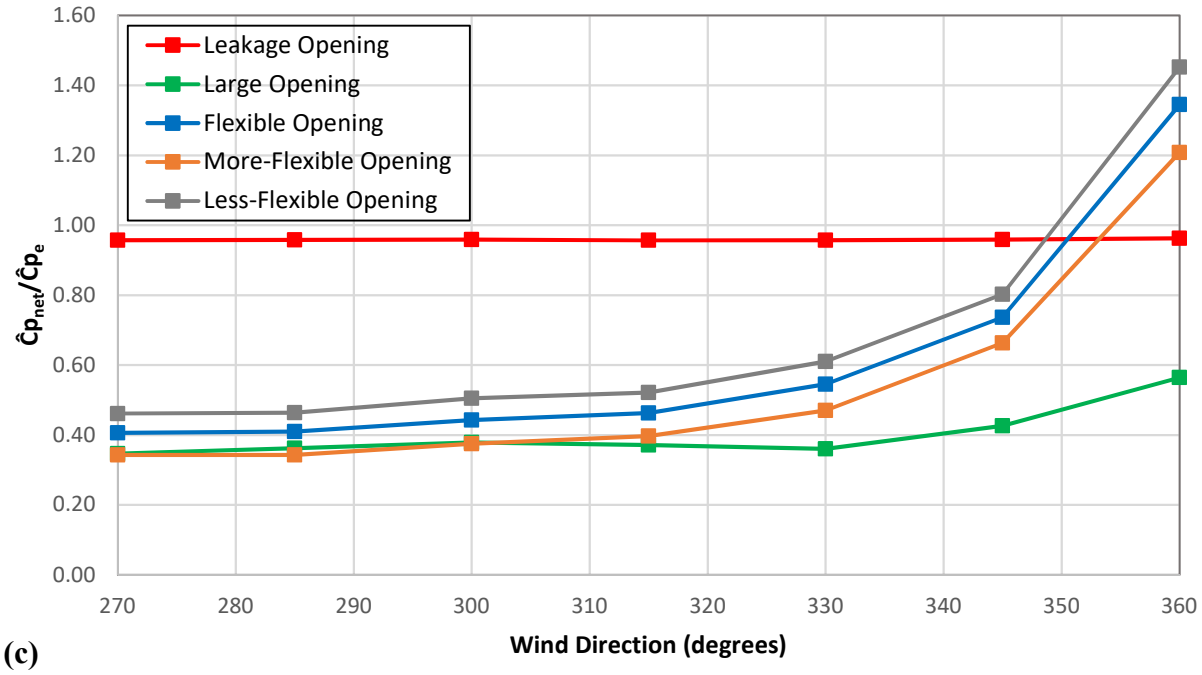

Figure 4-4: (a) Mean external and internal pressure coefficients, (b) maximum external and internal pressure coefficients, and (b) ratio of maximum net pressure coefficient to maximum external pressure coefficient as a function of wind direction.

Due to the similarity of the trends with wind direction, many of the observations made from the normal wind direction statistics in Table 4-1 apply to the other wind directions. For the majority of wind angles in Figure 4-4(a), mean internal pressure increases with increased opening size and flexibility in rigid and flexible opening cases, respectively. For these same wind angles, flexible openings produce larger mean internal pressures than rigid openings, with the mean external pressures falling between the rigid and flexible internal pressures. It should be noted, however, that the different models (MDE and SDE) used in the rigid and flexible openings may have played a role in these latter trends.

For the maximum internal pressures in Figure 4-4(b), both the flexibility of the door and size of the opening play a role, once again. The size of the opening seems to be slightly more important in the range of opening size and flexibility studied, as the large opening case has maximum pressures similar to the flexible case, while the leakage case has much lower pressures than all the flexible cases. There also exists a relationship between flexibility of the door and maximum

internal pressures, with the increased flexibility resulting in higher pressures when comparing the three flexible opening cases across all wind directions. Unsurprisingly, the maximum external pressures are consistently larger than all internal pressures.

Figure 4-4(c) shows the ratio of maximum net to maximum external pressure for the same range of wind directions. Once again, the trends of ratio with wind direction are similar across all the opening cases. The leakage opening ratio remains just below 1.00. For the flexible opening cases, the ratios are mostly constant between 270° and 315°, with rapid increases in the ratio as the wind becomes parallel to the garage door. Although these ratios are high, the loads on the door for parallel wind directions are small.

4.2 Failure Wind Speeds

4.2.1 Method

This section of the study combines the results from past experimental testing with the internal pressure modelling to estimate the failure wind speeds of garage doors. Specifically, the net pressures at failure (Table 2-2) are needed from the capacity tests, along with the ratio of maximum net to maximum external pressure from the internal pressure modelling (Table 4-1). The failure wind speed is calculated using the following equation:

$$V_{3s,fail} = \sqrt{\frac{p_{net,fail}}{(GCp_e)F0.5\rho}} \quad \textbf{(11)}$$

where $V_{3s,fail}$ is the failure wind speed of the garage door, $p_{net,fail}$ is the net failure pressure taken from past testing, GCp_e is the peak external pressure coefficient, F is the ratio of the maximum net pressure to the maximum external pressure from the internal pressure modelling, and ρ is the density of air taken as 1.23 kg/m^3. The range of peak external pressure coefficients is 1.1 to 1.6, corresponding to wind directions of 270° to 315°, since failure is less likely for other wind directions.

4.2.2 Results

Although six garage doors were tested in Jaffe at al. (2019), only four of them had their net pressure versus opening area data tracked: the three Product 2 samples, and the single Product 3 sample. Although only these two different garage door designs could be analyzed with internal pressure modelling, they are rather different from each other in strength. From experimental testing (Table 2-2), Product 2 had a failure pressure of 0.56 kPa, whereas the stronger Product 3 had a failure pressure of 1.75 kPa. This disparity in strength ensures that a full range of wind resistance capabilities is being analyzed. Product 2 and Product 3 designs exhibited similar opening area versus net pressure relationships, and therefore, similar factors of maximum net pressure to maximum external pressure despite their large difference in strength. This meant that it could reasonably be assumed that other garage door designs have a similar factor. Therefore, by applying the same method, an estimation can be made for the failure wind speed of the other two designs as well (Product 1 and Product 4), despite not having opening area versus net pressure data for these tests.

To calculate the expected failure wind speeds of the four tested garage doors, values needed to be selected for the net failure pressure, the ratio of peak net to peak external pressure, and the peak external pressure coefficient. The net failure pressures are taken from Table 2-2, the F value is taken as 0.4 from the large and flexible opening cases (rounded to one significant figure), as these are the opening cases most similar to typical garage doors at failure, and the GCp_e is taken as 1.3 from Gavanski and Uematsu (2014). The resulting expected failure wind speeds are rounded to the nearest 5 km/h. The expected wind speeds range from 130 to 265 km/h, and can be found along with the parameters in Table 4-2.

As mentioned in the introduction, a garage door failure on a standard wood-frame house falls under the DI, FR12 (one- or two-story family residences) and DOD4 (inward collapse of garage door). FR12-DOD4 has a lower bound wind speed of 130 km/h an upper bound of 185 km/h, and an expected wind speed of 155 km/h. The Product 2 samples have an expected failure wind speed similar to the expected wind speed of DOD4. This is likely a more common garage door, seeing as it is not as strong as and less expensive than the Product 3 sample, and probably the type of garage door that the wind speed range for FR12-DOD4 was based upon. The Product 3

sample failed at a wind speed much above the upper bound DOD4 of 185 km/h, with an estimated speed of 265 km/h. This highlights the immense variation in strength of various garage door types. An EF-1 tornado commonly produces high enough wind speeds to cause failure in the Product 2 design, but the results suggest it would take at least a weak EF-3 tornado to cause failure in the Product 3 design. Other components would likely fail at these wind speeds for FR12.

Table 4-2: Expected, lower-bound, and upper-bound failure wind speeds of garage doors.

	Door Type	$p_{net,fail}$ **(kPa)**	F	GCp_e	$V_{3s,fail}$ **(km/h)**
Expected	Product 1	0.42	0.4	1.3	130
	Product 2	0.56	0.4	1.3	150
	Product 3	1.75	0.4	1.3	265
	Product 4	0.90	0.4	1.3	190
Lower Bound	Product 1	0.38	1.0	1.6	70
	Product 2	0.50	1.0	1.6	80
	Product 3	1.58	1.0	1.6	145
	Product 4	0.81	1.0	1.6	105
Upper Bound	Product 1	0.46	0.4	1.1	150
	Product 2	0.62	0.4	1.1	170
	Product 3	1.92	0.4	1.1	305
	Product 4	0.99	0.4	1.1	220

The Product 1 and Product 4 samples have estimated failure wind speeds around the lower bound of 130 km/h and upper bound of 185 km/h, respectively, of FR12-DOD4. If it can be assumed

that these added designs have the same F value as the previous two designs, then these results seem to suggest the validity of these EF-Scale wind speeds. Three of the four designs fall reasonably within the range of FR12-DOD4, and the strongest among them is much stronger, which was already hypothesized by its high net failure pressure.

In reality, there is not one wind speed that defines the failure of each garage door sample. Rather, it is a wide range of wind speeds, as failures will have variation in door strength, door flexibility, wind direction, etc. To account for this range of values, lower bound and upper bound failure wind speeds are added to Table 4-2, similar to the way bounds are included in the DODs of the EF-Scale. The lower bound wind speed is based on a door with a 10% reduction in strength (failure net pressure) and a higher GCp_e value of 1.6. The upper bound wind speed is based on a door with a 10% increase in strength and a lower GC_e value of 1.1. This range of GCp_e values represent the maximum and minimum values over the wind direction range of 270° to 315° from Figure 4-4(b). The lower bound also uses a ratio of peak net to peak external pressure of 1.0, to represent a very leaky, isolated garage where the internal pressure never builds up inside, like in the leakage opening case.

Across all door designs and strength/flexibility bounds, the failure wind speeds for the garage doors have a wide range from 70-305 km/h, showing the significant difference that adjusting the parameters makes. Product 1, Product 2, and Product 4 designs now have lower bound failure wind speeds that dip below the lower bound of FR12-DOD 4, and Product 3 and Product 4 designs have upper bounds exceeding the upper bound of FR12-DOD4.

An important conclusion to make from these results is how they should be integrated into wind speed assessments. Some of the calculated extreme lower and upper bound wind speeds are not applicable to the EF-Scale. For example, the lower bound failure wind speeds for Product 1 and Product 2 are below the 85 km/h lower bound for threshold of visible damage (DOD1) for FR12, making them unrealistic. A failure at this low a wind speed would have a very low probability of occurrence. Similarly, the expected and upper bound wind speed for Product 3 is above the 245 km/h upper bound for exterior walls collapsing (DOD7) for FR12, meaning, at this point, the garage door would have failed as a result of the rest of the structure collapsing, especially due to the increased internal pressures from a more flexible opening, mentioned earlier. Based on the

failure wind speed results, along with these points, the EF-Scale wind speeds for weaker, 1-layer constructed garage doors, such as Product 1 and Product 2, should be 85-170 km/h, while the wind speeds for stronger, 3-layer constructed garage doors, such as Product 3 and Product 4, should be 105-245 km/h.

4.3 Summary

In summary, results from experimental testing of six garage door samples of four different designs in Jaffe et al. (2019) are combined with an internal pressure model. Two of the four door designs had their open area recorded as a function of net pressure during testing, which is used as input into the internal pressure model to determine how much of the external pressure applied by the PLAs in testing was resulting in net pressure on the doors. Combining past garage door experimental results and internal pressure results of this study, 3-second failure wind speeds are obtained for each of the garage door samples tested, which are then compared to the EF-Scale. The conclusions are as follows:

- The internal pressure model computationally examines a series of rigid and flexible garage door models that have a range of peak net to peak external pressure values of 0.34-0.96. The most important values are from the large and flexible opening cases, representing door designs Product 2 and Product 3, which have ratios of 0.35 and 0.41, respectively.
- Combining the above with failure net pressures in Jaffe et al. (2019), expected failure wind speeds of 130 km/h, 150 km/h, 265 km/h, and 190 km/h are found for Products 1 to 4, respectively. Given the varying nature of each door type with respect to strength and flexibility, upper and lower bounds are found for each garage door sample by varying a few key parameters of the failure wind speed equation. This results in a larger overall range of failure wind speeds of 70-305 km/h. Clearly, other failures would happen first for the higher end of this wind speed range.
- When comparing these failure wind speeds with FR12-DOD4 in the EF-Scale, reasonably similar results are found for the three lower capacity products. Stronger garage doors would unlikely be the first significant failure in the failure sequence of a wood-frame house.

5. Conclusions and Recommendations

5.1 Conclusions

This study explores internal pressure modelling issues for tornadoes. The goal of the first half of the study is to understand whether the unique details of tornadic wind fields alter the dynamics of internal pressures. To accomplish this goal, the single discharge equation (SDE) is used in a theoretical model based on the Helmholtz resonator concept to simulate internal pressures from measured external pressures in a tornado simulator. The results and accuracy of the model are then compared to similar work done with atmospheric boundary layer (ABL) wind tunnel studies to assess the validity of the model in tornadic winds.

It is found that the internal pressure model is able to simulate the actual internal pressures relatively well, with the difference in measured and simulated mean internal pressure coefficients having an average of 0.07, which is partially explained by the measurement uncertainty of ±0.07. The error in the model is highest when the vortex radius is passing over the structure and the wind direction at the opening is near 90°. For comparison, the average difference in measured and simulated mean internal pressure coefficients for the ABL cases from the National Institute of Standards and Technology database is 0.03 and 0.01, respectively, fully within measurement uncertainty.

The main causes of inaccuracies in the model are believed to be physical differences in the tornadic wind flow, a lack of internal volume scaling, and interference from the measurement instruments. The differences in the wind flow mainly stem from the spatially non-uniform nature of the turbulence. Sub-vortices in the tornado, as well as vertical wind components in and around the core, cause this region to be highly turbulent with relatively fast and large changes in wind speed and direction, whereas regions further from the main vortex have much lower turbulence. A comparison of the statistical distribution and parent fits of the tornadic and ABL wind pressures showed that the tornadic winds are mostly similar to ABL winds, except for when the vortex radius passes over the building and the wind direction is approximately normal, where these large changes in the wind occur. An analysis of the magnitudes and spectra of the SDE equation terms, and spectra of the pressures themselves, then showed that a lack of internal

volume scaling in the present tornadic study likely contributed to the differences in the model accuracy compared to the ABL experiments.

The second half of this study involved using the same internal pressure model to assess garage door failures in severe winds. The model is first used to determine the ratio of peak net pressure to peak external pressure during garage door failures for several door types, taking into account the fluctuating open area as the door is loaded by the wind. These results are then combined with failure net pressures of past garage door tests to determine the failure wind speeds of a typical garage door.

From the theoretical model, a ratio between the peak net and peak external pressure of 0.34-0.96 is determined for a series of rigid and flexible garage door samples. The realistic, flexible garage door sample has a ratio of 0.4. When combined with experimental failure testing, the failure wind speed range across all door types is determined to be 130-265 km/h, and 130-190 km/h when the strongest of the four door types is excluded. These ranges have reasonable agreement to FR12-DOD4 of the EF-Scale, especially when excluding the strongest door design. When examining upper and lower bound failure wind speeds by varying a few key parameters, the largest range of failure wind speeds is determined to be 70-305 km/h. Evidently, other structural failures would happen prior to the upper end of this range; however, the results still show the large variations in garage door failure wind speeds.

5.2 Recommendations

There are several ways that the WindEEE experiment and analysis could be improved. One way this could be done would be to simply use the same model to simulate internal pressures in more tornado simulations. The data from the second half of the current WindEEE experiments with the vortex translation 90° to the long wall of the building have yet to be studied in depth and there are many other variables that can be altered in the experiment (building dimensions, opening size, vortex size, vortex translation speed, etc.). Many of the physical phenomena could be further examined and sources of error eliminated or mitigated in future experiments. These include the multiple vortices, the static pressure model, and the Cobra probe coverage. Internal volume scaling by ways such as an internal pressure chamber in the building model could also

improve results. Another way this study could be improved would be to alter the computational model itself, to attempt to better account for the differences in ABL and tornadic winds.

There are several items that could be addressed as future work for the garage door portion of this research, with two main items addressed here. As mentioned, only two of the four garage door designs had their net pressure versus opening area tracked. Running the experiments again with more trials while tracking all the data for each test would improve experimental results for the model. There also exists many other types of garage doors with various strength and flexibility properties. Analyzing of more garage door types would be valuable, as well as examining the possible effects of spatial pressure gradients on the garage door response and capacity.

Both parts of this study should continue to improve the understanding of tornado-induced internal pressures in residential structures and low-rise buildings. Further research into how internal pressures develop in tornadoes and when garage doors fail in severe winds will greatly aid in improving structural resilience to these forces of nature.

6. References

ASCE/SEI 7-16. (2017). Minimum design loads and associated criteria for buildings and other structures. Reston, VA: American Society of Civil Engineers.

ASHRAE (2005). "Chapter 27: Ventilation and infiltration," in: *ASHRAE Handbook: Fundamentals* (Atlanta, GA: American Society of Heating, Refrigerating and Air-Conditioning Engineers) 27.1–27.31.

ASTM E1233-06 (2006). *Standard Test Method for Structural Performance of Exterior Windows, Doors, Skylights, and Curtain Walls by Cyclic Air Pressure Differential*. West Conshohocken, PA: ASTM International. Available online at: www.astm.org

ASTM E330/E330M-14 (2014). *Standard Test Method for Structural Performance of Exterior Windows, Doors, Skylights and Curtain Walls by Uniform Static Air Pressure Difference.* West Conshohocken, PA: ASTM International. Available online at: www.astm.org

Baker, C., & Sterling, M. (2019). Are Tornado Vortex Generators fit for purpose? *Journal of Wind Engineering and Industrial Aerodynamics*, *190*, 287-292.

Benjamin, J. R., & Cornell, C. A. (2014). *Probability, statistics, and decision for civil engineers*. Courier Corporation.

Cheng, J. (2004). Testing and analysis of the toe-nailed connection in the residential roof-to-wall system. *Forest products journal*, *54*(4).

Dao, T. N., Graettinger, A. J., Alfano, C., Gupta, R., Haan, F. L., Prevatt, D., ... & Kashani, A. G. (2014). Failure progression analysis of observed residential structural damage within a tornado wind field. In *Structures Congress 2014* (pp. 1448-1459).

Environment Canada. (2014). Enhanced Fujita Scale Damage Indicators and Degrees of Damage, accessed on Jan 6, 2017 from https://ec.gc.ca/meteo-weather/default.asp?lang=En&n=1F0BCA63-1&offset=2&toc=show

Feng, C., & Chen, X. (2018). Characterization of translating tornado-induced pressures and responses of a low-rise building frame based on measurement data. *Engineering Structures*, *174*, 495-508. Fujita, T. T. (1971). *Proposed characterization of tornadoes and hurricanes by area and intensity*. Satellite and Mesometeorology Research Project, Department of the Geophysical Sciences, the University of Chicago.

Gavanski, E., & Uematsu, Y. (2014). Local wind pressures acting on walls of low-rise buildings and comparisons to the Japanese and US wind loading provisions. *Journal of Wind Engineering and Industrial Aerodynamics*, *132*, 77-91.

Ginger, J. D. (2000). Internal pressures and cladding net wind loads on full-scale low-rise building. *Journal of Structural Engineering*, *126*(4), 538-543.

Haan Jr, F. L. (2017). An examination of static Pressure and Duration effects on Tornado-induced Peak Pressures on a low-rise Building. *Frontiers in Built Environment*, *3*, 20.

Haan Jr, F. L., Balaramudu, V. K., & Sarkar, P. P. (2010). Tornado-induced wind loads on a low-rise building. *Journal of structural engineering*, *136*(1), 106-116.

Ho, T. C. E., Surry, D., & Morrish, D. (2003). NIST/TTU cooperative agreement–windstorm mitigation initiative: Wind tunnel experiments on generic low buildings. *The Boundary Layer Wind Tunnel Laboratory, University of Western Ontario*.

Ho, T. C. E., Surry, D., Morrish, D., & Kopp, G. A. (2005). The UWO contribution to the NIST aerodynamic database for wind loads on low buildings: Part 1. Archiving format and basic aerodynamic data. *Journal of Wind Engineering and Industrial Aerodynamics*, *93*(1), 1-30.

Holmes, J. D. (1980). Mean and fluctuating internal pressures induced by wind. In *Wind Engineering* (pp. 435-450). Pergamon.

Holmes, J. D. (2015). *Wind loading of structures*. CRC press.

International Code Council. (2015). *International Residential Code.*

Irminger, J. O. V., & Nøkkentved, C. (1930). *Wind-pressure on Buildings: Experimental Researches.(First-[second] Series)* (No. 23). Danmarks naturvidenskabelige samfund.

Jaffe, A. L., Riveros, G. A., & Kopp, G. A. (2019). Wind Speed Estimates for Garage Door Failures in Tornadoes. *Frontiers in Built Environment*, *5*, 14.

Kezele, D. B. (1989). *Global roof failures of modern residential buildings*. Faculty of Engineering Science, University of Western Ontario.

Kikitsu, H., Sarkar, P. P., & Haan, F. L. (2011). Experimental study on tornado-induced loads of low-rise buildings using a large tornado simulator. In *Proceedings of 13th international conference on wind engineering*.

Kopp, G. A., & Gavanski, E. (2011). Effects of pressure equalization on the performance of residential wall systems under extreme wind loads. *Journal of Structural Engineering*, *138*(4), 526-538.

Kopp, G. A., Morrison, M. J., Gavanski, E., Henderson, D. J., & Hong, H. P. (2010). "Three little pigs" project: hurricane risk mitigation by integrated wind tunnel and full-scale laboratory tests. *Natural Hazards Review*, *11*(4), 151-161.

Kopp, G. A. & Wu, C.-H. (2020). A framework to compare wind loads on low-rise buildings in tornadoes and atmospheric boundary layers. *Journal of Wind Engineering and Industrial Aerodynamics*. Accepted manuscript. doi: 10.1016/j.jweia.2020.104269

Letchford, C., Levitz, B., & James, D. (2015). Internal pressure dynamics in simulated tornadoes. In *Structures Congress 2015* (pp. 2689-2701).

Levitan, M. L., & Mehta, K. C. (1992). Texas Tech field experiments for wind loads part 1: building and pressure measuring system. *Journal of Wind Engineering and Industrial Aerodynamics*, *43*(1-3), 1565-1576.

Levitan, M. L., & Mehta, K. C. (1992). Texas Tech field experiments for wind loads part II: meteorological instrumentation and terrain parameters. *Journal of Wind Engineering and Industrial Aerodynamics*, *43*(1-3), 1577-1588.

Lieblein, J. (1974). *Efficient Methods of Extreme-Value Methodology.* No. NBSIR 74-602, Washington, DC: National Bureau of Standards.

Liu, H. (1975, June). Wind pressure inside buildings. In *Proceedings of the 2nd US National Conference on Wind Engineering Research, Colorado State University, June* (pp. 22-25).

McDonald, J. R., & Mehta, K. C. (2006). *A recommendation for an enhanced Fujita scale (EF-scale)*. Wind Science and Engineering Center, Texas Tech University.

Miller, C. S., Kopp, G. A., Morrison, M. J., Kemp, G., & Drought, N. (2017). A Multichamber, Pressure-Based Test Method to Determine Wind Loads on Air-Permeable, Multilayer Cladding Systems. *Frontiers in Built Environment*, *3*, 7.

Minor, J. E. (1994). Windborne debris and the building envelope. *Journal of Wind Engineering and Industrial Aerodynamics*, *53*(1-2), 207-227.

Morrison, M. J., Kopp, G. A., Gavanski, E., Miller, C., & Ashton, A. (2014). Assessment of damage to residential construction from the tornadoes in Vaughan, Ontario, on 20 August 2009. *Canadian Journal of Civil Engineering*, *41*(6), 550-558.

Oh, J. H. (2004). *Wind-induced internal pressures in low-rise buildings* (Masters thesis dissertation, Faculty of Graduate Studies, University of Western Ontario).

Oh, J. H., Kopp, G. A., and Inculet, D. R. (2007). The UWO contribution to the NIST aerodynamic database for wind loads on low buildings: Part 3. Internal pressures. J. Wind Eng. Ind. Aerodyn. 95, 755–779. doi: 10.1016/j.jweia.2007.01.007

Pearce, W., Sykes, D.M. (1999). Wind tunnel measurements of cavity pressure dynamics in a low-rise flexible roofed building. J. Wind Eng. Ind. Aerodyn. 82, 27–48.

Pan, K., Montpellier, P., & Zadeh, M. (2002). Engineering observations of 3 May 1999 Oklahoma tornado damage. *Weather and forecasting*, *17*(3), 599-610.

Quiroga Diaz, P. S. (2006). *Uncertainty analysis of surface pressure measurements on low-rise buildings* (Doctoral dissertation, The University of Western Ontario).

Rajasekharan, S. G., Matsui, M., & Tamura, Y. (2013). Characteristics of internal pressures and net local roof wind forces on a building exposed to a tornado-like vortex. *Journal of Wind Engineering and Industrial Aerodynamics*, *112*, 52-57.

Refan, M., & Hangan, H. (2018). Near surface experimental exploration of tornado vortices. *Journal of Wind Engineering and Industrial Aerodynamics*, *175*, 120-135.

Roueche, D. B., Prevatt, D. O., & Haan, F. L. (2020). Tornado-induced and straight-line wind loads on a low-rise building with consideration of internal pressure. *Frontiers in built environment*, *6*, 18.

Sabareesh, G. R., Matsui, M., & Tamura, Y. (2013). Ground roughness effects on internal pressure characteristics for buildings exposed to tornado-like flow. *Journal of Wind Engineering and Industrial Aerodynamics*, *122*, 113-117.

Sabareesh, G. R., Matsui, M., & Tamura, Y. (2019). Vulnerability of roof and building walls under a translating tornado like vortex. *Frontiers in built environment*, *5*, 53.

Sarkar, P. P., & Kikitsu, H. (2009). Experimental studies on internal pressure and debris strike for improved tornado induced loads of low-rise buildings. *Proceedings of the 41st US-Japan Panel on Wind and Seismic Effects, Tsukuba, Japan*.

Shen, S. Y., Masters, F. J., Upjohn, H., II, L., & Sinnreich, J. (2017). Simulation of Time-Varying spatially Uniform Pressure and near-surface Wind Flows on Building components and cladding. *Frontiers in Built Environment*, *3*, 24.

Sills, D., Cheng, V., McCarthy, P., Rousseau, B., Waller, J., Elliott, L., ... & Auld, H. (2012). Using tornado, lightning and population data to identify tornado prone areas in Canada. In *Preprints, 26th AMS Conference on Severe Local Storms, Nashville, TN*.

Smith, D. (2010). Validation of wind and wind-induced pressure data collected at the Institute for Building and Home Safety's state-of-the-art multi-peril applied research and training facility, Wind Science and Engineering Research Center, Lubbock, Texas.

Sparks, P. R., Schiff, S. D., & Reinhold, T. A. (1994). Wind damage to envelopes of houses and consequent insurance losses. *Journal of Wind Engineering and Industrial Aerodynamics*, *53*(1-2), 145-155.

Thampi, H., Dayal, V., & Sarkar, P. P. (2011). Finite element analysis of interaction of tornados with a low-rise timber building. *Journal of Wind Engineering and Industrial Aerodynamics*, *99*(4), 369-377.

Vickery, B.J. (1986). Gust factors for internal pressures in low-rise buildings. *Journal of Wind Engineering and Industrial Aerodynamics.* 23, 259–271.

Wang, J., Cao, S., Pang, W., & Cao, J. (2017). Experimental study on tornado-induced wind pressures on a cubic building with openings. *Journal of Structural Engineering*, *144*(2), 04017206.

Wu, C. H., & Kopp, G. A. (2016). Estimation of wind-induced pressures on a low-rise building using quasi-steady theory. *Frontiers in built environment*, *2*, 5.

Appendices

Appendix A – Comparison of External Pressure Taps Surrounding Opening

As mentioned in Chapter 3, one of the main sources of error in the simulated internal pressure measurements in the tornadic WindEEE experiment is a surprising difference in the external pressure taps surrounding the opening. Figure A-1 shows building wall CD that contained the opening, with four pressure taps highlighted: Tap 88 (bottom left), Tap 89 (top left), Tap 103 (bottom right), and Tap 104 (top right). The measured external pressure for the purposes of the internal pressure model is taken as an equally-weighted average between these four taps, seeing as they are equally spaced around the opening. However, upon further investigation, surprising differences are found in the individual external pressures of the four taps, even when taken as an average over all relevant configurations.

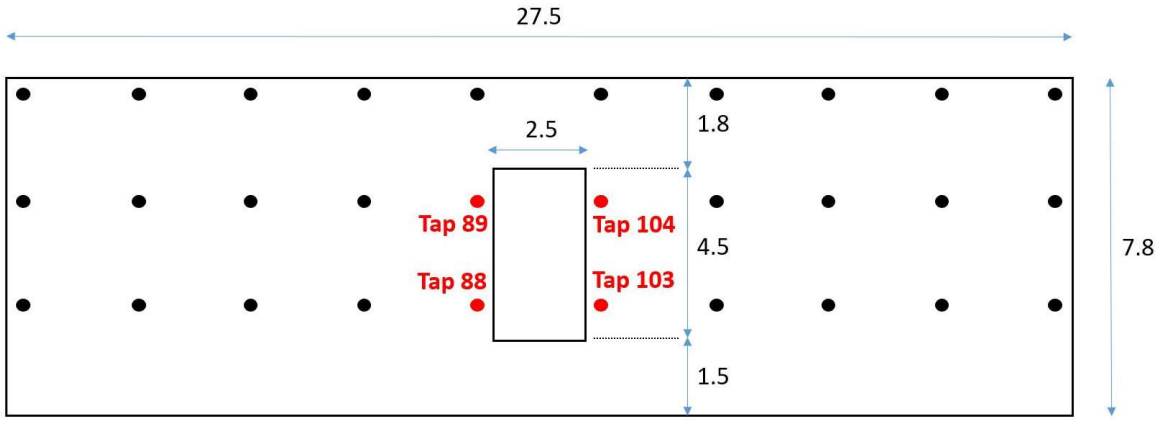

Figure A-1: Pressure tap layout on wall CD of the WindEEE building model highlighting the four taps surrounding the opening that are used for the internal pressure model. All dimensions are shown in centimetres.

To explore this issue further, the internal pressure model is run with each of the four taps individually as the external pressure input, as well as combinations of two adjacent taps (e.g., the two top taps: 89 and 104). Figure A-2 shows the difference between the measured internal pressure coefficients in the model and the simulated internal pressure coefficients using the SDE with each of the four pressure taps as individual inputs. Figure A-2(a) plots the pressure coefficients with vortex location and Figure A-2(b) plots the coefficients with wind direction at

the opening. In both figures, Tap 88 is shown in green, Tap 89 is shown in blue, Tap 103 is shown in red, and Tap 104 is shown in black. The pressure coefficients in these figures are ensemble-averaged using the same methods discussed in Chapter 3 that were used for Figure 3-5. From these figures, there are some clear differences in the measurements of the taps.

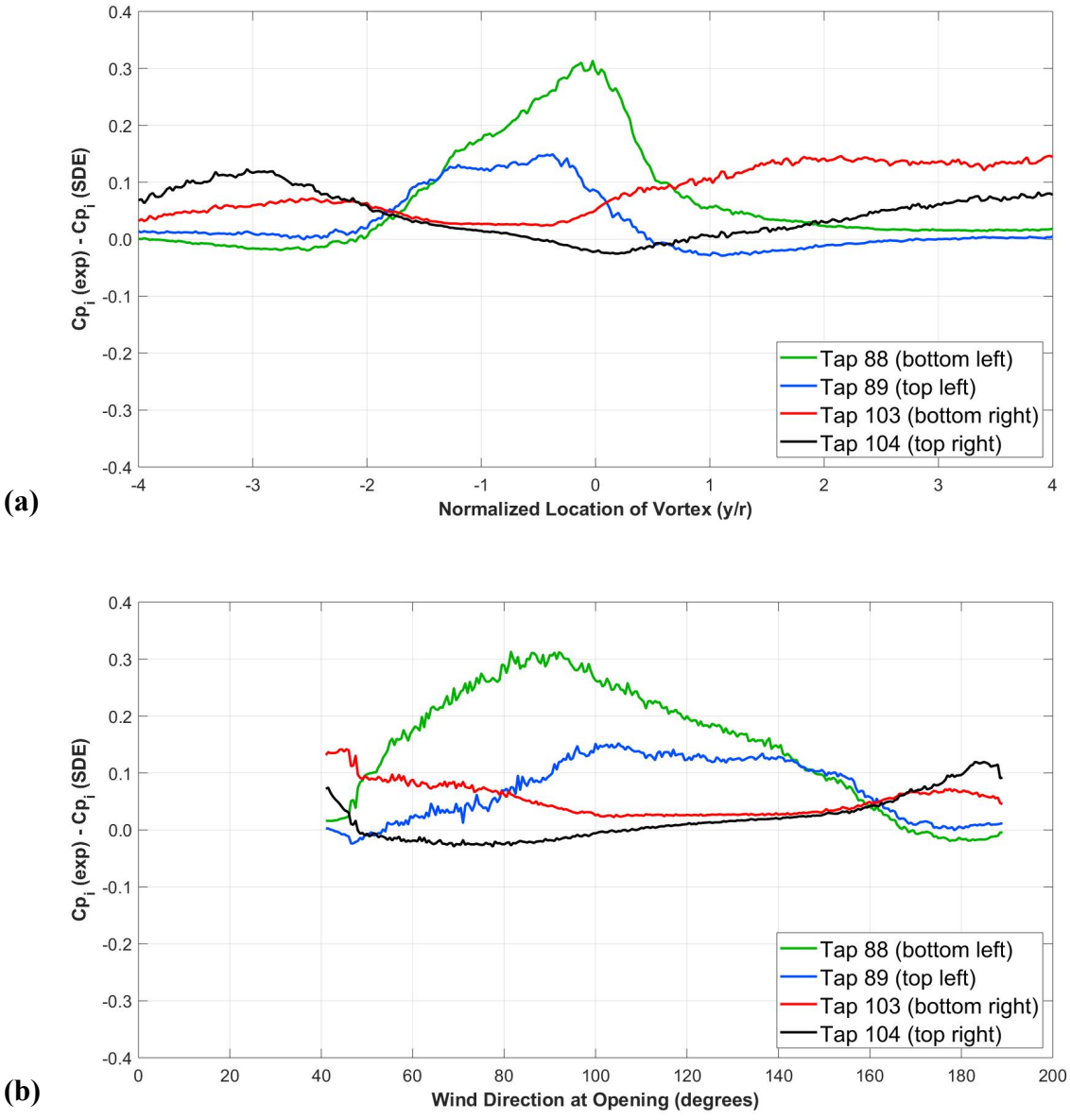

Figure A-2: Difference between the ensemble-averaged experimental and simulated internal pressure coefficients using each of the four external pressure taps surrounding the opening. The coefficients are plotted vs. (a) normalized vortex location (y/r) and (b) wind direction at the opening (θ_o).

The first observation from Figure A-2 is the difference between the taps left of the opening (88 and 89) and right of the opening (103 and 104). The left taps appear to simulate the internal pressure more accurately when the vortex is farther from the building, producing more oblique winds, and less accurately as the vortex radius is nearing and overtop of the building, producing winds normal to the opening. Additionally, the lower taps appear to better simulate internal pressures, overall, than their left- or right-sided upper tap counterparts. Tap 89 is typically more accurate than Tap 88, and Tap 104 is typically more accurate than Tap 103.

There are a couple possible explanations for the differences between the individual external pressure taps. The most plausible known explanation is various interferences with the tap measurements. These interferences could result from the Cobra probes (specifically probes C and D), the Cobra probe mounts, and the building itself. Measures are taken to limit these interferences in experimental setup, but the nature of the WindEEE experiments, especially due to the winds approaching the building model from all sides, make intrusion with the Cobra probes impossible to avoid. Another possibility is that the multiple vortices present in the simulated tornado are causing many local differences in measurements of adjacent pressure taps. Although, taking an average over many trials should mitigate these differences.

As stated in the main body, the internal pressure model is overall fairly accurate in simulating measured internal pressures. However, this appendix shows that using certain pressure taps or combinations of taps could potentially improve the accuracy. As an example, Figure A-3 once again plots the ensemble-averaged mean, maximum, and minimum external and internal pressures coefficients as a function of vortex location and wind direction, using the same methods described in Chapter 3, but only using the top taps (89 and 104) as external pressure inputs.

When compared to Figure 3-5 from Chapter 3, Figure A-3 produces overall more accurate simulated internal pressure, especially after the vortex translates past the model. This corresponds to wind directions at the opening below 90°. The only portion of the plots that are noticeably less accurate are at early tornado location values of $y/r \leq -3$, or $\theta_o \geq 185$.

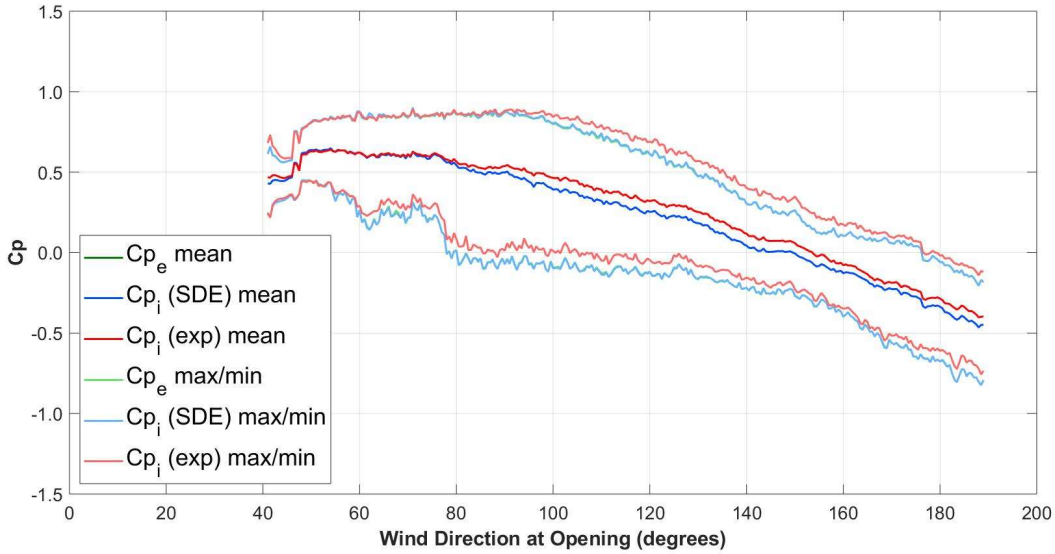

(a)

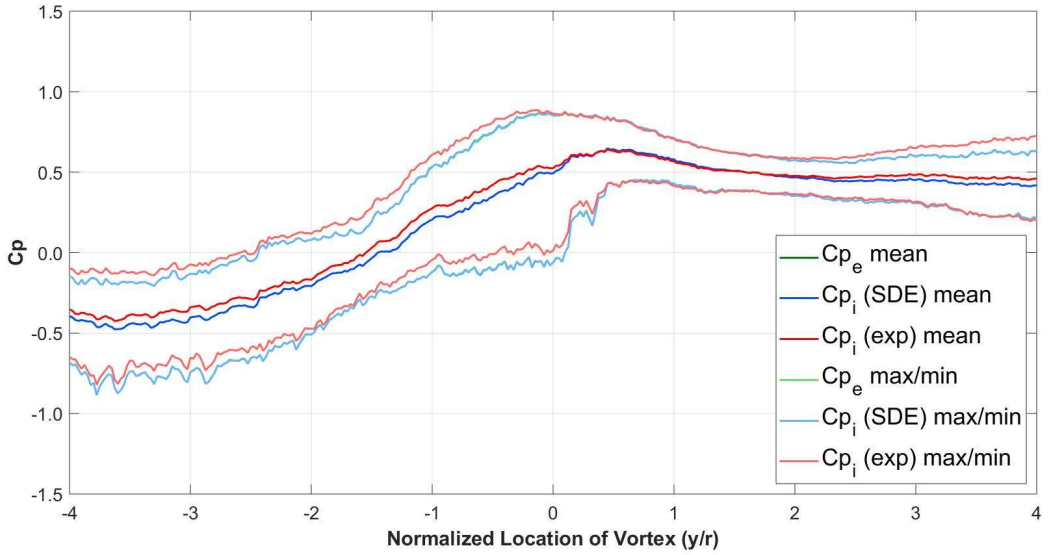

(b)

Figure A-3: Ensemble-averaged mean, maximum, and minimum of external and internal dynamic pressure coefficients from all configurations using only the upper two of the four external pressure taps surrounding the opening. External pressure at the opening, simulated internal pressure from the SDE, and measured internal pressure inside the building plotted vs. (a) normalized vortex location (y/r) and (b) wind direction at the opening (θ_o).

Curriculum Vitae

Name: Aaron L. Jaffe

Post-secondary Education and Degree:
The University of Western Ontario
London, Ontario, Canada
2013-2017 B.E.

Honours and Awards:
Dean's Honor List, Graduation with Distinction
2014-2017

NSERC Canadian Graduate Scholarship-Master's
2017

NSERC Undergraduate Student Research Award
2016

Dean's Award
2015

Related Work Experience:
Research Engineer
University of Western Ontario
2018-present

Teaching Assistant
University of Western Ontario
2017-2018

Publications:
Jaffe, A. L., Riveros, G. A., & Kopp, G. A. (2019). Wind Speed Estimates for Garage Door Failures in Tornadoes. *Frontiers in Built Environment*, *5*, 14.

Jaffe, A. L., Lalonde, E. R., & Kopp, G. A. (2016). Effects of Tornado Wind Speeds on Concrete Road Barriers. In *proceedings of 2016 CSCE Annual Conference, London, Canada.*